THE ELECTRONIC PROPERTIES OF NOBLE METAL DOPED SILICON NANOCRYSTALS USING HYBRID DENSITY FUNCTIONAL THEORY

by

CEDRIC LEON MAYFIELD

Presented to the Faculty of the Graduate School of
The University of Texas at Arlington in Partial Fulfillment
of the Requirements
for the Degree of

MASTER OF SCIENCE IN PHYSICS

THE UNIVERSITY OF TEXAS AT ARLINGTON
MAY 2013

Acknowledgements

It is my pleasure to express gratitude to the people that made this thesis possible. First of all I wish to thank my advisor, Dr. Muhammad Huda for suggesting and supervising this research. He has shared with me a philosophy that not only made this thesis possible but taught me the routine of professionalism. His insights, patience and encouragements were vital to this end. I also wish to thank my colleague and friend, Pranab Sarker for his kind assistance and enthusiasm for academic discourse. The discussions we had were always complementary to our physics curriculum. I wish to express sincere gratitude to Dr. Asok Ray and Dr. Qiming Zhang for donating their time to read my thesis. It is truly an honor to have distinguished faculty serve on my thesis committee. I am also thankful for the seamless pedagogy given by the Physics Department faculty members. I wish to also thank the physics office staff, in particular Margie, Stacy and Bethany for all of their help over the years. I would especially like to thank my sister, Chandra Jones for her support and encouragements. Lastly and most importantly, I wish to thank my parents, Rev. Curtis and Ernestine Mayfield for their unconditional love and care. Their guidance, objectivity and emotional support got me through the difficult times.

April 17, 2013

Abstract

THE ELECTRONIC PROPERTIES OF NOBLE METAL DOPED SILICON NANOCRYSTALS USING HYBRID DENSITY FUNCTIONAL THEORY

Cedric Leon Mayfield, M.S.

The University of Texas at Arlington, 2013

Supervising Professor: Muhammad N. Huda

One of the most challenging issues in semiconductor physics is to engineer band structures for a particular device. Contemporary photovoltaic (PV) and photoelectrochemical (PEC) devices rely on defect energy levels and nano-scaling to customize their band structures. As the length scale of a material becomes comparable to the exciton Bohr radius the free particle behavior of charge carriers transition to bound states where energy levels are quantized. In this thesis, hybrid density functional theory has been used to study the electronic properties of silicon nanocrystals (SiNCs) having 75, 150 and 300 silicon atoms. The atomic coordinates were defined by two geometries (diamond and wurtzite) of bulk phase silicon. The global minimum energy structures for both geometries at each size were found for particular variation on magnetic moments, dopant, dopant position, and surface passivation with hydrogen. We report our results on bond lengths, binding energies, formation energies, HOMO-LUMO gaps, and density of states. We also report results on electronic occupations derived from Mulliken population analysis. Our results show that the SiNCs have tunable HOMO-LUMO gaps with respect to size and that the inclusion of noble metals produces inter-gap defect levels. In addition,

we have found that hydrogen passivation affected the doping behavior significantly. Contrary to the general expectation, hydrogen passivation contributed to the energy levels near the highest occupied orbital. Overall, our results suggest the SiNCs can be used to construct optimal photovoltaic applications or used individually as photocatalysts.

Table of Contents

List of Illustrations

List of Tables

Chapter 1

Introduction

1.1 Motivation

The International Energy Agency has estimated that the global demand for energy could be fifty percent higher in 2035 than it is today [1]. Yet fossil fuels remain to be the dominant energy sources. Since fossil fuels are finite and have a negative impact on the environment scientist are motivated to develop alternative ways of supplying energy. Observing nature has been the most instructive on how to accomplish this task Naturally occurring processes from photosynthesis [2] to climate change convert solar energy and it stands to reason that this is our best option. Utilizing converted solar energy is a natural process to renew energy sources.

Photovoltaic (PV) and photochemical (PC) technology has attracted attention in industry and academia sufficiently enough to be recognized as an integral part of the solution toward meeting energy challenges [2–4]. PV and PC devices based on novel semiconductor materials are currently being explored that can lower the cost and increase the efficiency of solar energy conversion [5–7]. Semiconducting materials such as silicon nanocrystals are being looked at because of the novel properties that derive from quantum confinement [8–11].

Scientist at the National Renewable Energy Laboratory (NREL) observed photocurrent quantum efficiencies exceeding one hundred percent in QD solar cells [6]. The size dependence of band gap energies can be implemented in the design of energy converting devices which affords the device absorption of photons across the entire range of the visible solar energy spectrum. Also QDs have shown to create multiple excitons. per high energy photon and/or exciton per multiple low energy photons [12,13],

which is the ability to allocate photons across a broader energy spectrum than ever before considered in bulk materials.

A significant effort has been made in experimental procedures [14–21] to understand the catalytic properties of noble metals that are beneficial to growing the Si nanostructures. The fabrication of semiconducting nanomaterial made of Si relies heavily on the reduction of metal ions and the oxidation of Si in the growth environment. However a fundamental understanding of formation energies of the metals in nanosilicon is paramount to the reduction and oxidation potential these materials may have. Understanding of fundamental properties like formation energies will allow for the rational design and synthesis of new materials with precise control over their electronic, structural, magnetic, and optical properties. Toward this end, atomic-scale theory and simulation provide excellent means of rigorous, quantitative research studies.

Pristine nanowires have been grown using Au and Ag nanoparticles and more recently Cu clusters, in a metal-assisted vapor-liquid-solid method [15,16]. This method utilizes noble metal nanodroplets as catalyst. Si vapor dissociates at the noble metal liquid-Si solid interface. The aim of this thesis is to acquire the fundamental and quantitative understanding of noble metal atom, e.g., Cu, Ag and Au, interaction with semiconductor nanostructures through a comprehensive computational modeling of doping noble metal atoms in silicon nanocrystals. Additionally no systematic study of noble doping silicon nanostructures is available in the literature. Such theoretical studies are important in the design of new experimental procedures and thus important to the design of new devices that we can use to improve not just the quality of life but the standard of living.

1.2 Silicon Nanocrystals

1.2.1 Quantum Confined Energetics

In the bulk regime, silicon has an indirect low energy gap of 1.1 eV in the infrared region. As the size of the Si specimen decreases, reducing into a finite sized material this energy gap tends to widen driving the lowest occupied molecular orbital (LUMO) and highest occupied molecular orbital (HOMO) further apart and ultimately giving the small nanocrystals a direct-like behavior and discrete energy spectra, an important feature for photonic applications. The greater the difference between the HOMO and LUMO, more energy is needed to excite the nanocrystal, and therefore, more energy is released when the crystal returns to its fundamental state, resulting in a color shift from red to blue of the emitted light, hence allowing for photoluminescence across the visible spectrum. By this, one can infer that one of the main advantages of SiNCs is the possibility for atomic manipulation, allowing the control over the conductive and optical properties of the material just by altering the size of the gap or introducing dopants into its chemical composition.

SiNCs and similar nanostructures have been intensively studied in the last years due to their interesting quantum confinement properties [9–11,22–25]. The strong spatial localization of electrons and holes in SiNCs can enhance photoexcitations which give rise to luminescence. SiNCs are such systems that clearly demonstrate the quantum confinement effects associated with nanowires [26–30], nanorods [31,32], and nanoribbons [33], which have been explored intensely as of late. In each case, the study of spatially restricted materials has been observing size dependent behavior of energy gaps [34–37], binding energies [36,38–41] and formation energies [40,42–47]. Therefore investigating SiNCs serves as in instructional tool which aids in the understanding of more extended nanosystems.

1.2.2 Structural Attributes

Structural attributes such as surface state densities [10,32,43], facets [56–58], and corners [60] play strong roles in the equilibrium phases of nanostructures and thus are key factors to address in order to fine tune functionalization. In zero-dimensional systems these attributes are simplified by a more resolved localization of the effects which is embedded by the physical constraints of finite dimension. Much experimental evidence has been presented showing drastic changes in the electronic structure due to changes in these attributes. Simply reducing the number of atoms in materials or changing their atomic configurations drastically changes hardness [61–63] and charge carrier transport [64–67].

1.2.3 Passivation

Theoretical studies have revealed additional dependencies of the collective phenomena called quantum confinement effects. One such dependence is the treatment of surface states. It has been a general understanding that the termination of dangling bonds with H removes surface states from the band gap but should not modify the intrinsic nature of the occupied and unoccupied electronic states. However covalent H-Si bonds can distribute charge in a way to passivate the terminal bonding and yet have appearances in the electronic structure. In a theoretical study by Deng et al, for both anatase and wurtzite structures, a dependence on the nanocompound iconicity was observed for passivation efficiencies of real H atoms and partially charged pseudo H atoms [63].

Given the strong correlation between electronic and structural properties, it is feasible to suggest that these properties have interplay with H passivation. Electronic and/or structural variations may induce mechanisms that prevent or aid in the successful

passivation of structures. Ma et al. have shown terminal bonding deficiencies have a profound effect on nanostructure doping [64]. Experimentally it has been shown that replacing a few H surface atoms with more stable carbon and carbon monoxide bonds can stabilize the electroluminescence of porous Si diodes [65]. Also it has been shown that small H passivated silicon nanocrystals (H-SiNCs) that demonstrate strong quantum confinement exhibit blue luminescence while the same structure coated with an oxide shell exhibit yellow to red luminescence [66]. These results are related to complete and partial passivation of anisotropic energy states. Piezoresistive [73] and thermoelectric effects [74–76] rely heavily on anisotropic energy states. Therefore mechanisms that induce H passivation effects that may invoke such energy distributions should be investigated for possible refinements in electronic structure.

1.3 Summary

In this thesis we investigate the interplay of structural morphology, substitutional doping and H passivation on the electronic structure of SiNCs at three different sizes, namely 75, 150 and 300 Si atoms. At each size level, we have considered both the diamond and wurtzite structures. It is our aim to investigate in a systematic way the structural and electronic properties of SiNCs at these three different sizes and identify changes that occur in their properties due to H passivation of the surfaces, substitutional noble metal doping, and the combination of the two.

The organization of this thesis is as follows. In Chapter 2 we give a brief overview of the theory used to derive our quantum mechanical results. In Chapter 3 we describe the computational model and define quantities that are used in this theoretical analysis. In Chapter 4 we focus on the effect of H passivation and how it pertains to mechanical and electronic stabilities when determining the lowest energy properties. In Chapter 5 we

discuss the results from doping noble metal atoms in the determined lowest energy structure. Finally in Chapter 6 we give some concluding remarks on the derived energy signatures.

Chapter 2

Theory

Quantum mechanics was developed in the early part of the twentieth century to solve problems which could not be explained by classical mechanics. To model the electronic structure of materials using quantum mechanics, Schrödinger's equation must be solved; however in nearly all cases we cannot solve Schrödinger's equation exactly. This chapter outlines the various approximations used and the mechanics of solving within these approximations, as well as some of the general physics used in this thesis.

2.1 First Principles Techniques

The lowest energy properties, electronic structure and total energy of a system can be calculated through the time-independent, non-relativistic Schrodinger equation

$$\hat{H}\psi = E\psi \tag{2.1}$$

where $\hat{H}$ is the Hamiltonian operator and ψ is the wavefunction. For heavy atoms, neglecting relativistic effects will lead to erroneous results, as the mean square velocity of an electron in the 1 *s* orbital will be a significant fraction of the speed of light.

In atomic units, the non-relativistic Hamiltonian for N electrons and M nuclei is

$$\hat{H} = -\sum_{i=1}^{N}\frac{1}{2}\nabla_i^2 - \sum_{A=1}^{M}\frac{1}{2M_A}\nabla_A^2 - \sum_{i=1}^{N}\sum_{A=1}^{M}\frac{Z_A}{r_{iA}} + \sum_{i=1}^{N}\sum_{j>1}^{N}\frac{1}{r_{ij}} + \sum_{A=1}^{M}\sum_{B>A}^{M}\frac{Z_A Z_B}{R_{AB}} \tag{2.2}$$

where r_{iA} is the distance between the i^{th} electron and the A^{th} nucleus, r_{ij} is the distance between the i^{th} and j^{th} electron, R_{AB} is the distance between the A^{th} and B^{th} nucleus, M_A is the ratio of the mass of nucleus A to the mass of an electron, and Z_A is the atomic number of nucleus A. The five terms given in the Hamiltonian

represent the kinetic energy of electrons, the kinetic energy of nuclei, the Coulomb attraction between electrons and nuclei, the repulsion between electrons, and the repulsion between nuclei, respectively.

As nuclei are much slower moving than electrons, the Hamiltonian given in equation 2.2 can be further simplified through the Born-Oppenheimer approximation, in which the electrons are considered to be moving in a field of fixed nuclei. By using this approximation, the kinetic energy of the nuclei and repulsion between nuclei become a constant and the Hamiltonian reduces to

$$\hat{H} = -\sum_{i=1}^{N} \frac{1}{2} \nabla_i^2 - \sum_{A=1}^{M} \frac{1}{2M_A} \nabla_A^2 - \sum_{i=1}^{N} \sum_{A=1}^{M} \frac{Z_A}{r_{iA}} + \sum_{i=1}^{N} \sum_{j>1}^{N} \frac{1}{r_{ij}} \qquad (2.3)$$

Equation 2.3 is termed the electronic Hamiltonian. The energy derived from this Hamiltonian as a function of nuclear position, can be used as a potential energy surface for studying nuclear motion.

It is difficult to solve for the wavefunction ψ exactly, in anything but the simplest of cases, so a number of approaches using different approximations have been developed. The most common approaches are the Hartree-Fock (HF) and Density Functional Theories (DFT), which will be described in the next sections.

2.2 Hartree-Fock Theory

The electronic Hamiltonian given in equation 2.3 is a many-electron Hamiltonian. HF theory considers a simpler problem, where the many-electron problem is replaced by a one-electron problem, by treating the electron-electron repulsion in an average way [72]. The *n*-electron wavefunction is approximated by the product of a set of *n*-independent single electron wavefunctions

$$\psi(\mathbf{r}_1,\mathbf{r}_2,\mathbf{r}_i...\mathbf{r}_n,) = \psi_1(\mathbf{r}_1)\psi_2(\mathbf{r}_2)\psi_i(\mathbf{r}_i)...\psi_n(\mathbf{r}_n) \tag{2.4}$$

A many electron wavefunction such as this is termed a Hartree Product. Schrödinger's equation can then be expressed as a set of coupled single particle equations

$$\hat{H}\psi_i(\mathbf{r}) = E_i\psi_i(\mathbf{r}) \tag{2.5}$$

where $\hat{H}$ is now given by

$$\hat{H} = -\frac{1}{2}\nabla_{\mathbf{r}}^2 + V_{en}(\mathbf{r}) + V_H(\mathbf{r}) \tag{2.6}$$

where $-\frac{1}{2}\nabla_{\mathbf{r}}^{\mathbf{2}}$ represents the kinetic energy, $V_{en}(\mathbf{r})$ is the Coulomb attraction between electrons and nuclei, and $V_H(\mathbf{r})$ is the Hartree electron-electron Coulomb repulsion. The Hartree term treats the effects of repulsion in an average way, so within this approximation each electron is effectively in an average field produced by all of the other particles in the system. For an electron in a single particle orbital $\psi_i(\mathbf{r}_i)$, the Hartree potential is given by

$$V_H(\mathbf{r}_i)\Psi_i(\mathbf{r}_i) = \sum_j^n \int \frac{\psi_j(\mathbf{r}_j)^*\psi_j(\mathbf{r}_j)}{|\mathbf{r}_i - \mathbf{r}_j|} d\mathbf{r}_j\psi_i(\mathbf{r}_i) = \sum_j^n \int \frac{|\psi_j(\mathbf{r}_j)|^2}{|\mathbf{r}_i - \mathbf{r}_j|} d\mathbf{r}_j\psi_i(\mathbf{r}_i) \tag{2.7}$$

equation 2.7 includes a term for electron self-interaction when $i = j$. In Hartree theory, this self-interaction is prevented by not performing the summation when $j = i$.

The Hartree product, as defined in equation 2.4, violates the Pauli Exclusion Principle. To satisfy the Pauli principle, the wavefunction needs to be antisymmetric with respect to the interchange of electrons between two orbitals

$$\Psi(\mathbf{r}_2,\mathbf{r}_1) = -\Psi(\mathbf{r}_1,\mathbf{r}_2) \tag{2.8}$$

The requirement of antisymmetry can be easily enforced by using Slater determinants for the following reasons. Electrons must be indistinguishable, so that the charge density does not change with the interchange of electrons

$$\left|\Psi(\mathbf{r}_1,\mathbf{r}_2)\right|^2 = \left|\Psi(\mathbf{r}_2,\mathbf{r}_1)\right|^2 \tag{2.9}$$

The Hartree product does not satisfy this requirement, which can be demonstrated by examing a two electron case, in which the wavefunction is represented by two single particle orbitals in which electron one is placed in ψ_1 and electron two is placed in ψ_2

$$\Psi(\mathbf{r}_1,\mathbf{r}_2) = \psi_1(\mathbf{r}_1)\psi_2(\mathbf{r}_2) \tag{2.10}$$

Swapping the positions of electron-one and electron-two gives

$$\Psi(\mathbf{r}_2,\mathbf{r}_1) = \psi_1(\mathbf{r}_2)\psi_2(\mathbf{r}_1) \tag{2.11}$$

which results in a different orbital occupation, which can lead to a different charge density. To satisfy the requirement of antisymmetry, a combination of single particle orbitals can be chosen that do satisfy the requirement of antisymmetry

$$\Psi(\mathbf{r}_1,\mathbf{r}_2) = \frac{1}{\sqrt{2}}\left(\psi_1(\mathbf{r}_1)\psi_2(\mathbf{r}_2) - \psi_1(\mathbf{r}_2)\psi_2(\mathbf{r}_1)\right) \tag{2.12}$$

where the $\frac{1}{\sqrt{2}}$ is included as a normalization factor. Antisymmetry is now satisfied as interchange of coordinates in equation 2.12 now satisfies equation 2.8. Equation 2.12 also demonstrates how an antisymmetric wavefunction satisfies the Pauli Exclusion Principle, as if both electrons occupy the same orbital, the wavefunction vanishes. Equation 2.12 can be written as a Slater determinant

$$\Psi(\mathbf{r}_1,\mathbf{r}_2) = \frac{1}{\sqrt{2}}\begin{vmatrix}\psi_1(\mathbf{r}_1) & \psi_2(\mathbf{r}_1)\\ \psi_1(\mathbf{r}_2) & \psi_2(\mathbf{r}_2)\end{vmatrix} \tag{2.13}$$

which can be generalized for an N-electron system as

$$\Psi(\mathbf{r}_1,\mathbf{r}_2,\mathbf{r}_i,...\mathbf{r}_n)=\frac{1}{\sqrt{N!}}\begin{vmatrix}\psi_1(\mathbf{r}_1) & \psi_2(\mathbf{r}_1) & \psi_3(\mathbf{r}_1) & ... & \psi_n(\mathbf{r}_1)\\ \psi_1(\mathbf{r}_2) & \psi_2(\mathbf{r}_2) & \psi_3(\mathbf{r}_2) & ... & \psi_n(\mathbf{r}_2)\\ \psi_1(\mathbf{r}_3) & \psi_2(\mathbf{r}_3) & \psi_3(\mathbf{r}_3) & ... & \psi_n(\mathbf{r}_3)\\ ... & ... & ... & ... & ...\\ \psi_1(\mathbf{r}_n) & \psi_2(\mathbf{r}_n) & \psi_3(\mathbf{r}_n) & ... & \psi_n(\mathbf{r}_n)\end{vmatrix} \quad (2.14)$$

The Slater determinant given in 2.14 satisfies all the requirements for a wavefunction. Antisymmetry is met, as interchanging the coordinates of two electrons swaps two rows of the Slater determinant, which changes the sign of the determinant. Also, if two electrons occupy the same orbital, then two rows will be the same and the determinant will equal zero, conforming to the Pauli principle. The extra term generated due to the Pauli principle is called electronic exchange, and can be interpreted as the tendency of electrons with the same spin to avoid each other.

However, a correlation term accounting for electrons with opposite spin to avoid each other is completely neglected. This leads to the correlation energy (E_{corr}) being defined from Hartree-Fock (E_{HF}) as

$$E_{corr} = E_{exact} - E_{HF} \quad (2.15)$$

As E_{HF} is an upper bound to exact energy, the correlation energy will be negative. The main drawback of Hartree-Fock theory is its neglect of electron correlation effects, which leads to an overestimation of electron-electron repulsion in the system. There are more complex approaches that improve on the Hartree-Fock technique, such as the configuration interaction method, that instead of solving a single electron solution, solve many-electron problem. The problem in using these many-body methods is that they are considerably more computationally expensive than the Hartree-Fock technique.

2.3 Density Functional Theory

Density functional theory [73] is another approach, which avoids trying to solve the many-electron wavefunction $\Psi(r_1, r_2, r_3, ...)$, by instead solving for the electron density distribution $n(r)$. Density functional theory is based on the 1964 theorem of Hohenberg and Kohn and the computational scheme by Kohn and Sham. It is based on the idea that every ground state observable property of quantum mechanical system can be calculated from two different external potentials, unless the two differ by a constant, i.e. the ground state electronic structure is uniquely determined by the electron density. The ground state density can be found by minimizing a total energy of the form

$$E_{tot} = \int v_{ext}(r) n(r) dr + F[n] \tag{2.16}$$

where v_{ext} is some external potential and $F[n]$ is a universal functional of the density.

While in principle there exists an exact exchange-correlation energy term, leading to an exact ground state energy, it is a complicated expression and is not known explicitly. To use DFT in practice, approximations are needed to define E_{XC}. The simplest approximation, proposed by Kohn and Sham, is the Local Density Approximation (LDA) [74]

$$E_{XC}^{LDA}[n(r)] \equiv \int \varepsilon_{XC}^{LDA}(n(\mathbf{r})) n(\mathbf{r}) d\mathbf{r} \tag{2.17}$$

where $\varepsilon_{XC}(n(r))$ is the exchange-correlation energy per particle of uniform electron gas (jellium). This function has been modeled using quantum Monte Carlo data and fitted by analytic expressions such as the Vosko-Wilk-Nusair-LDA and the Perdew-Zunger-LDA. The LDA is a good approximation for slowly-varying systems, such as simple metals, but less accurate in systems where the density varies rapidly. In general, the LDA

overestimates atomization energies and predicts equilibrium bond lengths to be shorter than found in experiment.

To improve upon the accuracy if the LDA in non-homogeneous systems other approximations have been tried, with the most successful being based on the Generalized Gradient Approximation (GGA) [74]. The exchange-correlation energy within the GGA improves upon the LDA by including the local spatial variations of density

$$E_{XC}^{GGA} = \int f\left(n(r), |\nabla n(r)|\right) dr \tag{2.17}$$

There have been many functions proposed, for example the Perdew-Becke-Ernzerhof (PBE) and PW91 functionals.

The LDA and GGA approximations for the exchange-correlation energy tend to work well for systems with delocalized electrons, but are less reliable in systems with localized electrons.

2.4 Hybrid Methods

In a series of papers [75–77] Becke examined the effects of exchange and correlation in DFT on the computation of thermochemical properties. In examining the role of exact exchange he demonstrated the inclusion of a small component of exact-exchange within the DFT exchange-correlation approximation lead to more accurate molecular energetics.

The exchange-correlation approximation proposed by Becke was

$$E_{XC} = (1 - a_0) E_{XC}^{LDA} + a_0 E_X^{exact} + a_x \Delta E_X^{B88} + E_C^{LDA} + a_c \Delta E_C^{PW91} \tag{2.18}$$

where E_X^{exact} is the exact exchange energy, ΔE_X^{B88} is Becke's gradient correction to the exchange functional, and ΔE_C^{PW91} is the Perdew and Wang gradient corrected correlation.

The parameters a_0, a_x, and a_c are semi-empirical coefficients that were determined by a least-squares fit to atomization energies, ionization potentials, and electron and proton affinities in Pople's test set of atomic and molecular species, and Becke suggested values of $a_0 = 0.2$, $a_x = 0.72$, and $a_c = 0.81$.

When this method was implemented in the Gaussian 92 code, the Perdew and Wang correlation was replaced by the Lee-Yang-Parr (LYP) correlation and this hybrid functional was called B3LYP. As the LYP functional does not have an easily separable local component, Stephen *et al*. proposed the use of the VWN local correlation

$$E_{XC}^{B3LYP} = (1-a_0)E_{XC}^{LDA} + a_0 E_X^{HF} + a_x \Delta E_X^{B88} + a_c E_C^{LYP} + (1-a_c)E_C^{VWN} \qquad (2.19)$$

In this thesis we use the Gaussian 03 software suite of programs implementation of B3LYP throughout all calculations.

2.5 Basis Sets

Most implementations of *ab initio* techniques for solid state applications use basis sets that are based on either plane waves and/or Gaussian type orbitals. These types of basis sets are popular as they make the computation of integrals relatively easy. Other types of basis sets that are used include Slater type orbitals, which are a product of spherical harmonics $Y_{lm}(\theta,\phi)$ by a radial function $R(r)$, where $R(r) = r^n e^{-r\xi}$. Slater type orbitals (STO) give a much better representation of the cusps of the wavefunction near the nuclei than Gaussian type orbitals GTO, but are not widely used because the calculation of multi-center two electron integrals are more complicated, and are consequently more computationally expensive than using Gaussians.

There are both advantages and disadvantages in using either plane wave or Gaussian type basis sets. One of the great advantages of plane waves is that they can

be applied to any system equally well. As plane waves form an orthonormal complete set, then any normalizable, continuous function can be expanded to an arbitrary precession within the plane wave basis set. Varying the plane wave cut-off can then be systematically increased until a desired accuracy of calculation is reached. Also, the computer coding required to manipulate the plane waves is also simpler.

The downside with plane wave basis sets is that many more basis functions are required to describe the wavefunction than when using Gaussian functions. Even with large, modern computers, the computational cost and memory requirements are too large to describe core electrons accurately. There are different ways to overcome this problem, with the most common approach being the use of the pseudopotential approximation. In the pseudopotential approximation the core electrons and the strong nuclear potential are removed and replaced by a weaker pseudopotential which acts on a set of pseudo wavefunctions.

Another disadvantage in using plane waves is found when dealing with surfaces. When performing a plane-wave calculation, the entire simulation cell is filled with plane waves up to the cut-off energy, regardless of the location of the atoms. This means that in surface calculations, there is a computation cost associated with the empty, “vacuum gap” above the atomic surface. This vacuum gap cannot be made too small or the surface will interact with is periodic image above.

Gaussian functions can be far more computationally efficient, but unlike a plane wave basis, Gaussian functions do not constitute a universal set, and individual basis sets must be developed for each atom in the periodic table. Gaussian type functions can be expressed as

$$\chi^{GTF} = e^{-\alpha r^2} x^l y^m z^n \tag{2.20}$$

where α is the exponent and l, m, and n are integer exponents of Cartesian coordinates. This can be factorized into Cartesian components

$$\chi^{GTF} = \chi_x^{GTF}\chi_y^{GTF}\chi_z^{GTF} \tag{2.21}$$

where each component has the form

$$\chi_x^{GTF} = (x - x_0)^l e^{-\alpha(x-x_0)^2} \tag{2.22}$$

While the Gaussian functions can be efficiently calculated, a Gaussian function is not an optimum basis function. To obtain a better basis function, while retaining the computational efficiency of Gaussian functions, basis functions can be formed from a fixed linear combination of primitive Gaussians. This linear combination is termed a contraction

$$\chi_i(\mathbf{r}) = \sum_{j=1}^{L} d_{ji} g_j(\alpha_{ji}\mathbf{r}) \tag{2.23}$$

where L is the length of the contraction, d_{ji} is the contraction coefficient, and α_{ji} are the contraction exponents.

A contracted Gaussian function gives a good approximation to an atomic orbital, but it lacks any flexibility to expand or shrink in the presence of other atoms in a molecule. Hence the contracted GTO is too robust to meet the accuracy requirements for research quality results. The solution is to extend the contracted Gaussian function by adding extra basis functions beyond the minimum number required to describe each atom, use minimal basis functions for the core electrons or use an effective core potential and split the extra basis functions in the valence regions only. Then the Hartree-Fock procedure can weight each atomic orbital basis function more or less to get a better description of the wavefunction. If there are twice the minimum of basis functions, this is

called a “double zeta” basis set, if triple the minimum of basis functions, then it is called a “triple zeta” basis set, and so forth; the zeta, ζ , comes from the exponent in the GTO.

Chapter 3

Computational Details

3.1 Software Implementation

For the total energy, we performed an *ab initio* calculation within the framework of density-functional theory (DFT) as it is implemented by the Gaussian 03 software package [78]. Treatment for the exchange and correlation was handled by Becke's three parameter hybrid functional combined with the Lee-Yang-Parr correlation functional, denoted B3LYP [79–81]. Hybrid functionals are known to provide better band gap and structural properties for semiconductors [80,81]. The electron orbitals are described by a double-ζ basis set with the effective core potential (ECP) of Hay and Wadt, known as the Los Alamos National Laboratory 2-Double Zeta basis set (LANL2DZ) [83,84]. LANL2DZ allows the valence region fine structure resolution by compensating sensitivity to nuclear and core interactions and doubling the electron orbitals in the highest occupied and lowest unoccupied states. For H-Si compounds, the B3LYP/LANL2DZ method has reproduced binding energies and bond lengths that are identical to experimental values within negligible error. For example, the method was tested on the Si dimer and H-Si molecule, giving bond lengths of 2.352 Å and 1.55 Å, respectively, which should be compared with experimental values of 2.352 Å and 1.47 Å.

3.2 Choice of Basis Set

Our choice of the LANL2DZ basis set was a selection based on a balance between computational cost and accuracy. For the silicon atom, the Hay-Wadt pseudo-potential with the associated basis set is used for the core electrons and the valence electrons, respectively. The Hay-Wadt ECP and the associated basis set for the silicon

atom is shown in Table 3.1 and Table 3.2. For the heavier noble metal atoms, scalar relativistic effects are accounted for via baits ECP. Full treatment of relativity (spin-orbit interaction) bears a computational cost so in order to avoid extending calculation times we have excluded these corrections to the total energy.

The quality of the B3LYP/LANL2DZ scheme for the description of noble metal atom doping in Si nanocrystals was tested by atomic and dimer calculations. In Table 3.3 we show the calculated bond lengths, binding energies, ionization potentials, and electron affinities of all the noble metal atoms and their silicide dimers. Our chosen basis set underestimates the ionization energy (E_I) and electron affinitiy (E_A) for the Si atom. However, the E_I and E_A of the Cu atom are comparable with the user-specified basis set in terms of agreeing with experiment. The dimer calculation of Si shows an improvement on the E_I and E_A with a slight discrepancy in bond length. The copper-silicide has bond lengths that concur fully with experiment as expected. Even though E_I and E_A are underestimated, the binding energies and bond lengths are in fairly good agreement with available experimental data and other quantum chemical predictions.

These results clearly indicate that the choice of basis set does a good job for the systems studied in this work .Therefore we are confident that our chosen level of theory is adequate for the description of the electronic structure of all noble metal atom doping in SiNCs. Throughout this work full geometry optimization of the SiNCs has been performed without any constraints on symmetry operations using the LANL2DZ basis set. All computations have been performed utilizing the High Performance Computing (HPC) infrastructure at the University of Texas Arlington.

Table 3.1: Hay and Wadt Pseudopotentials for Silicon Atoms

n_k	ζ_k	d_k
d-potential		
1	505.3138	-10.0000
2	103.2221	-84.9236
2	23.4569	-30.3299
2	6.7506	-12.1049
2	2.1603	-1.8945
s-d potential		
0	689.4911	3.0000
1	114.1729	60.5207
2	35.7424	201.3086
2	9.4530	65.9400
2	2.2544	19.0301
p-d potential		
0	88.9379	5.0000
1	76.7774	6.6414
2	56.1481	247.5972
2	21.1874	129.3715
2	6.8277	47.4617
2	2.1001	11.7377

Table 3.2: Basis functions for silicon atom

Exponents (α_i)	Coefficients (c_i)
s orbitals	
1.2220000	0.274462
0.2595000	0.616689
0.0931100	0.558086
p orbitals	
2.5800000	-0.039785
0.2984000	0.521997
0.0931100	0.587382

Table 3.3: Bond lengths (B_L) in Å, binding energy (E_B) in eV, ionization energy (E_I) in eV, and electron affinities (E_A) in eV of Relevant Atomic and Dimer Species [85]

Atom/Diatom	Data Source	B_L	E_B	E_I	I_A
Si	B3LYP/LANL2DZ			7.263	0.772
	B3LYP/GEN			8.113	0.948
	Experiment			8.15	1.385
Cu	B3LYP/LANL2DZ			7.826	0.812
	B3LYP/GEN			8.030	1.002
	Experiment			7.724	1.235
Ag	B3LYP/LANL2DZ			7.752	1.088
	B3LYP/GEN				
	Experiment				
Au	B3LYP/LANL2DZ			9.421	2.166
	B3LYP/GEN				
	Experiment				
Si2	B3LYP/LANL2DZ	2.352	2.620	7.882	2.620
	B3LYP/GEN	2.286	3.081	7.905	1.815
	Experiment	2.246	3.290	7.921	2.176
CuSi	B3LYP/LANL2DZ	2.298	1.946	7.431	0.645
	B3LYP/GEN	2.247	2.093	7.226	
	Experiment	2.28	2.225		
AgSi	B3LYP/LANL2DZ	2.489	0.788	7.441	0.669
	B3LYP/GEN	2.360			
	Experiment				
AuSi	B3LYP/LANL2DZ	2.377	1.236	7.796	0.873
	B3LYP/GEN	2.250			
	Experiment				

3.3 Comparative Energies

3.3.1 Binding Energy Calculations

Stability is quantified by a formulation of the calculated total energies. The binding energy per atom E_B is given by

$$E_B(Si_{M-1}) = [E_{TOT}(Si_M) - \mu_{nm} - M\mu_{Si}]/M \quad (3.1)$$

where E_{TOT} is the total ground state energy of a given nanocrystal at a given spin multiplicity obtained from the self-consistent calculation. μ_{nm} and μ_{Si} are the atomic energies of the noble metal atoms and Si atoms respectively. M is the number of atomic centers in the nanocrystal. For H passivated silicon nanocrystals (H-SiNCs), the binding energy is modified by subtracting the appropriately scaled H atomic energy and dividing the result over all atoms in the system i.e.

$$E_B(\mathrm{H_N Si_{M\text{-}1}}) = [E_{TOT}(\mathrm{H_N Si_{M\text{-}1}}) - \mu_{nm} - (M-1)\mu_{\mathrm{Si}} - N\mu_H]/M + N \quad (3.2)$$

where, M and N are the number of atomic centers and number of dangling bonds, respectively. The binding energy per atom calculation is a measure of the electromagnetic interaction between the constituents. This atom by atom relation affords this analysis the equal footing to compare relative stabilities of the different phases of silicon. The negative values for E_B refer to a bounded system.

3.3.2 Formation Energy Calculations

The formation energy, E_F of noble metal atoms in the SiNCs is defined as

$$E_F(\mathrm{Si_{n\text{-}1}M}) = [E(\mathrm{Si_{n\text{-}1}M}) - E(\mathrm{Si_n})] + [E(\mathrm{Si}) - E(\mathrm{M})] \quad (3.3)$$

where the first bracketed set represents the energy difference between the pure and doped SiNCs and the second bracketed set represents the energy difference between the dopant and the host atom. The sum of these two differences quantifies the amount of energy required to replace a Si atom with a noble metal atom and highlights the solubility of the dopants in equilibrium conditions. When passivating the nanocrystals, the binding energy was modified by adding the appropriate passivating atom energy with the correct scaling. In the case of E_F no such modification is needed. As long as the first bracketed set represents differences made between two passivated SiNCs of equal size and geometry, the energies associated with the passivating atoms are accounted for.

3.3.3 HOMO-LUMO Gap

The HOMO-LUMO energy gap E_G refers to the potential energy difference between the HOMO and LUMO and is defined as the energy difference between the HOMO and LUMO.

$$E_G = \varepsilon_{LUMO} - \varepsilon_{HOMO} \tag{3.4}$$

When a molecule absorbs this amount of energy it will transition from its most stable state (lowest energy state) to its first excited state. This information can be tied to the nanocrystals ability to generate photocurrent. The larger this energy difference the higher the energy required to excite the nanocrystal E_G can also be related to energy barriers for catalytic reactions. In zero-point energy calculations the HOMO energy serves as the Fermi level and the LUMO refers to the first excited state. Furthermore, in the quantum confinement model the E_G increases as the size of the nanocrystal decreases because the number of occupation levels decrease causing strongly quantized energy states.

3.4 Starting Parameters

The starting atomic configurations were fixed with all Si atoms occupying the same positions they would occupy in the bulk. We considered two common polymorphs of crystalline Si found at ambient temperature. The first morphology was the diamond structure which is a face centered cubic lattice that contains eight atoms per unit cell in the bulk state. The second morphology was the wurtzite structure which is a hexagonal close packing (hcp) lattice that has 14 atoms per unit cell in the bulk state. The wurtzite structure is commonly characterized by a shearing of the diamond structures unit cell so there are at least two perspectives common to each of the different structures. The point worth noting here is that these two structures offer completely different mechanical stabilities [31] as well as surface morphologies while remaining sufficiently similar to be compared. The mechanical stability is a measure of hardness for a material, therefore diamond and wurtzite will have differential responses to effective strain and the most resilient structure will emerge as the lowest energy state. Since diamond and wurtzite geometries only differ by a shearing of the unit cell, the surface morphologies are defined to be the uncommon perspectives between diamond and wurtzite geometries combined with the surface reconstructions resulting from geometry optimization.

3.5 Convergence Criteria

All of the nanocrystals studied in this thesis were allowed to fully relax until the maximum force between atoms was lower than 4.5×10^{-4} Ha/Bohr. Each calculation was performed self-consistently with 10^{-6} precision on convergence for two different spin states; a high spin state and a low spin state. The pristine nanocrystals were relaxed with their magnetic moments fixed in singlet (0 μ_B) and triplet spin states (2 μ_B). while the

doped nanocrystals have their magnetic moments fixed in doublet (1 μ_B) and quartet (3 μ_B) spin states. Determination of the magnetic moments was based on total number of valence electrons. If there is an even number of valence electrons in a structure, the limiting case on spin would be either a paramagnetic or diamagnetic state. Otherwise there is an odd number of valence electrons and the limiting cases are weakly paramagnetic (one net spin) or strongly paramagnetic (three parallel spin).

For each of the SiNCs studied, we have included an illustration of the optimized geometry along with plots of the bond length distributions for each SiNC. In the plots and tables, all quantities will be listed in order of increasing size. So the smallest SiNCs will be listed first. Significant properties such as binding energy per atom and formation energies are listed in the tables. Additionally figures for the density of states which include orbital contributions for the doped and passivated SiNCs are given. Mulliken atomic charges and illustrations of the HOMO's and LUMO's are also given

.

Chapter 4

Stability of Passivated and Unpassivated Silicon Nanocrystals

4.1 Determination of the Lowest Energy Geometry

In order to determine whether the diamond structure or the wurtzite structure made up the lowest energy geometry we made a series of comparisons between the total energies of the relaxed systems of just two size levels Si_{75} and Si_{150}. We calculated the total energies and E_B of the relaxed Si_{300} systems and confirmed the trends in stability, however a complete analysis of the structural and electronic attributes of only passivated silicon nanocrystals (H-SiNCs) at the 300 Si atom size level will be given. Cartesian coordinates on the results of geometry relaxation of passivated diamond silicon nanocrystals is given in Appendix A.

In Table 4.1 and Table 4.2 we present the total energies of the relaxed diamond and relaxed wurtzite unpassivated silicon nanocrystals (SiNCs), respectively. As mentioned before, the pristine structures have both high ($2\mu_B$) and low ($0\ \mu_B$) spin states possibilities. In Table 4.3 and Table 4.4 we present the total energies of the relaxed diamond and wurtzite H-SiNCs, respectively. Comparing the total energies as a function of spin we see the energy differences for SiNCs are small only differing by tenths of an electron volt. The total energy differences with respect to spin are significantly larger for H-SiNCs which points to a dependence on the magnetic quantum number for the stabilization of H passivation.

Comparing the relaxed total energies as a function of geometry we found for SiNCs the wurtzite structure had the most stable energies and for H-SiNCs the diamond structure had the most stable energies. Diamond H-SiNCs had the lower total energies because there were more H atoms used to passivate the diamond SiNCs than the

wurtzite SiNCs. The diamond (wurtzite) nanocrystals at the size levels of 75, 150, and 300 Si atoms required 76 (66), 140 (100), and 225 (170) H atoms, respectively, to passivate the surfaces. The difference in the number of H atoms prevents the comparison of the total energies on equal footing. Therefore in order to determine the lowest energy state by comparing the two energy profiles we must consider the atomic contributions to the overall stability. We will discuss the relative stabilities of these structures in more detail while discussing the binding energies per atom in section 4.2.

Table 4.1: Total Energies in eV for Unpassivated Diamond Silicon Nanocrystals

Species	**Si_{75}**		**Si_{150}**		**Si_{300}**	
Spin state	Singlet	Triplet	Singlet	Triplet	Singlet	Triplet
	-7909.487	-7909.903	-15838.279	-15838.661	-31682.825	-31685.930

Table 4.2: Total Energies in eV for Passivated Diamond Silicon Nanocrystals

Species	**$H_{76}Si_{75}$**		**$H_{140}Si_{150}$**		**$H_{225}Si_{300}$**	
Spin state	Singlet	Triplet	Singlet	Triplet	Singlet	Triplet
	-9187.427	-9184.258	-18180.790	-18179.896	-35499.442	-35488.449

Table 4.3: Total Energies in eV for Unpassivated Wurtzite Silicon Nanocrystals

Species	**Si_{75}**		**$Si_{15SiNCs0}$**		**Si_{300}**	
Spin state	Singlet	Triplet	Singlet	Triplet	Singlet	Triplet
	-7911.936	-7911.975	-15840.699	-15841.292	-31694.116	-31695.675

Table 4.4: Total Energies in eV for Passivated Wurtzite Silicon Nanocrystals

Species	**$H_{66}Si_{75}$**		**$H_{100}Si_{150}$**		**$H_{170}Si_{300}$**	
Spin state	Singlet	Triplet	Singlet	Triplet	Singlet	Triplet
	-9027.163	-9024.440	-17543.053	-17539.724	-34606.742	-34603.708

4.1.1 Relaxed Geometry

For a qualitative appreciation of the structural changes we have illustrated in Figures 4.1 – 4.4 relaxed diamond and wurtzite nanocrystals with and without H passivation at two different size levels. The relative influence of H passivation can be seen in the figures. With the exception of minimal expansions and contractions of the bond lengths, T_d symmetry is maintained in the core of both geometries. It is the absence of H passivation that results in major surface rearrangements that translates to distortions of the core Si-Si bond lengths. Therefore the degree in which distortion occurs is related to the number of dangling bonds.

Dangling bonds (also called surface states) show up in the electronic structure and prevent the characteristic quantum confined energy profile. Signatures in the structural attributes can indicate the degree in which the surface states are passivated e.g. passivation deficiencies can be identified upon visual inspection. In order to alleviate unwanted effects from surface states, sp^3 hybridization at the interfaces must be maintained. H passivation accomplishes this task with the smallest computational expense since it essentially “freezes” the atoms in place using one electron wave function per dangling bond.

Overall, the wurtzite SiNCs and H-SiNCs display the least amount of distortion within the core Si-Si bond lengths which indicates wurtzite structures have the lowest probability of incurring geometry induced passivation deficiencies. This is the first indication that the wurtzite structure is the most stable in this size range.

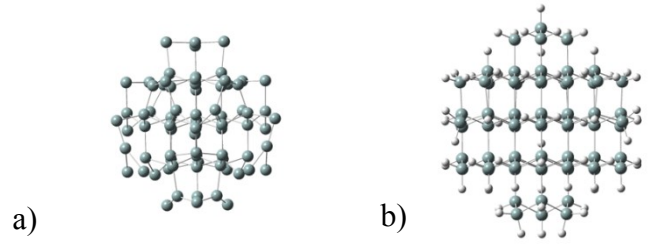

Figure 1: Optimized Geometry of Diamond a) Si_{75} and b) $H_{76}Si_{75}$.

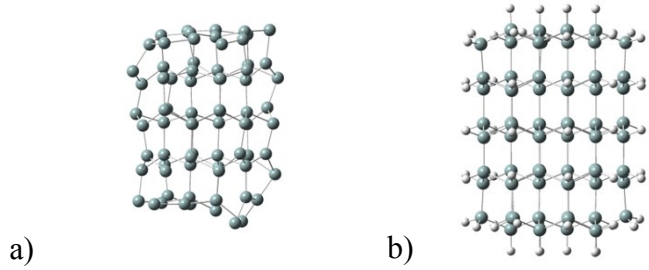

Figure 2: Optimized Geometry of Wurtzite a) Si_{75} and b) $H_{66}Si_{75}$.

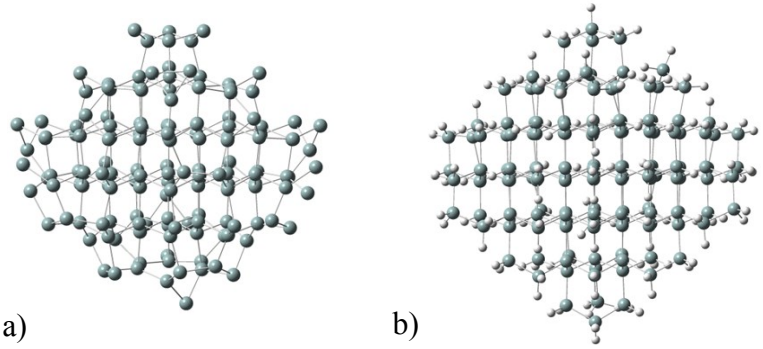

Figure 3: Optimized Geometry of Diamond a) Si_{150} and b) $H_{140}Si_{150}$.

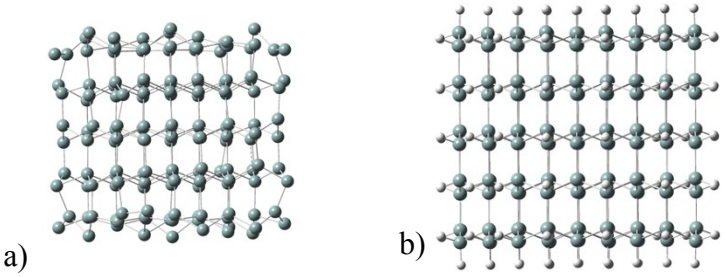

Figure 4: Optimized Geometry of Wurtzite a) Si_{150} and b) $H_{100}Si_{150}$.

4.1.2 Average Bond Lengths

In Figure 4.5 the average core Si-Si bond length of the relaxed SiNCs and H-SiNCs are reported as a function of the number of Si atoms. The only bonds considered to be core Si-Si bonds are those which belong to atoms that are four fold coordinated. From Figures 4.1 – 4.4 one can see all structures experienced expansions in their average bond lengths after relaxation but within 0.09 Å of the calculated dimer bond length. For SiNCs, as the number of Si atoms increased the amount of expansion reduced and the average interatomic distance tended to the calculated dimer value. For the passivated diamond and wurtzite nanocrystals the core Si-Si bond lengths are essentially unchanged.

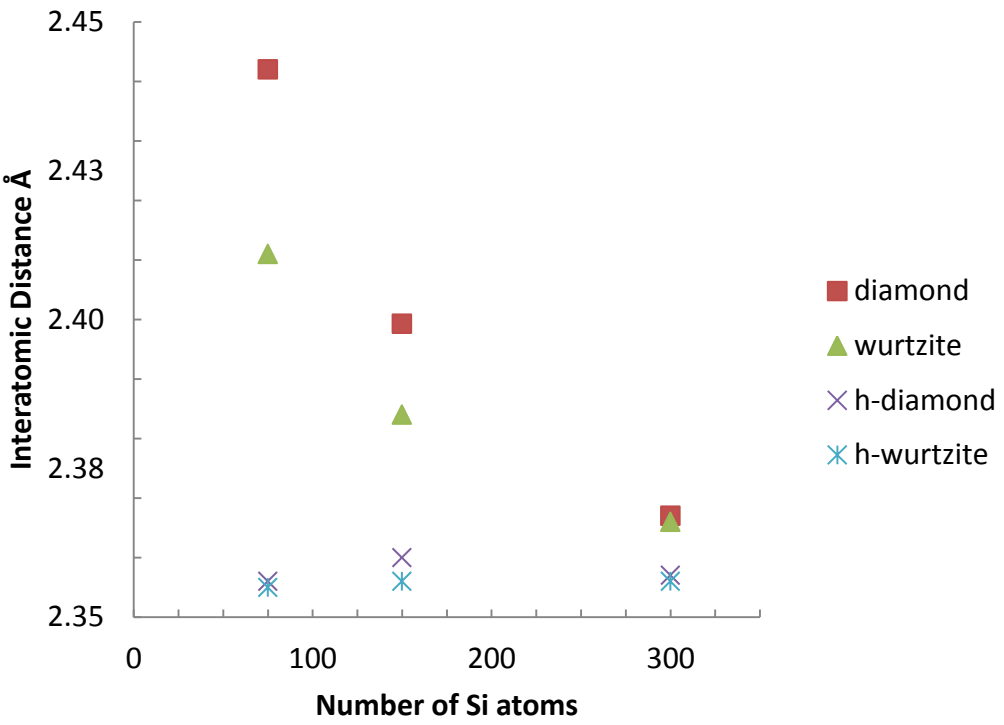

Figure 5: Average Si-Si bond lengths for each structure as a function of the number of Si atoms. The distances are given in angstroms. The x-axis represents the calculated Si dimer bond length.

4.1.3 Bond Length Distributions

All of the bond distributions are determined excluding bonds with surface atoms, so the expanded and contracted bonds of surface reconstruction and the strong bonding with passivating H atoms are not included. In Figure 4.6 (4.7) we report the Si-Si bond length distributions for diamond (wurtzite) SiNCs and H-SiNCs.

The distribution associated with SiNCs exhibit two peaks. These two peaks elucidate the patterns shown in Figure 4.5. The first major peak shows small deviations from the average bond lengths since the spread is within a tenth of an Angstrom from the average core Si-Si bond length and is associated with the binding strength that maintains the tetrahedral symmetry of the core Si-Si bonds. The averages of each structure all have less than 2.5% difference from the calculated Si dimer bond length (2.352 Å). The second peak gives an idea of how many core Si-Si bonds are outside of the statistical width of distribution and is associated with bonds that experience the largest expansions during geometry relaxation.

In Figure 4.6 and Figure 4.7 we report the Si-Si bond length distribution for diamond SiNCs and H-SiNCs respectively. The diamond Si_{75} has a Si-Si bond length distribution that has is peak around 2.442 Å which is a 3.8% difference from the calculated dimer bond length. The diamond Si_{150} core Si-Si bond length distribution has a broader spread and yet the average Si-Si bond length decreased to 2.399 Å which is a 1.9% difference from the calculated Si dimer bond length. The diamond $H_{76}Si_{75}$ has a spiked core Si-Si bond length distribution centered on an average of 2.356 Å which is a 0.2% difference from the calculated dimer value. This indicates that the diamond $H_{76}Si_{75}$ structure is well passivated with a surface potential created by the H-Si bonds. The diamond $H_{140}Si_{150}$ has a broad core Si-Si bond length distribution which reflects the range of distortion seen in this passivated structure. The peak of this distribution is centered on

an average bond length of 2.360 Å which is only a 0.3% difference from the calculated Si dimer bond length. However it is the shape of the distribution that indicates a distorted structure. Inefficiently passivating charge leads to instabilities in the bonding because the electrons must redistribute themselves in a way to supplement passivation. Even though the effect of H passivation did not increase bond stability enough to spike the Si-Si bond distribution of $H_{140}Si_{150}$ the effect was enough to bring the second peak bonds within the statistical width.

In Figure 4.8 and Figure 4.9 we report the Si-Si bond length distribution for wurtzite SiNCs and H-SiNCs. Again the unpassivated structures exhibit two peaks, however the second peak is not as prominent as the diamond structures second peak. This indicates that there are fewer core Si-Si bond lengths outside of the statistical width; another strong indication that the wurtzite structures are the most stable structures in this size range. For the wurtzite Si_{75} the core Si-Si bond length distribution is centered on 2.393 Å and has a small second peak. The second peak actually gets smaller when the number of Si atoms is doubled to Si_{150}. For wurtzite H-SiNCs all of the Si-Si bond length distributions are extremely sharp which is characteristic of Si-Si bonds that hardly deviating from their average value of 2.37 Å. This also corresponds to an average bond length that remains constant with increased number of Si atoms confirming the trend in Figure 4.5.

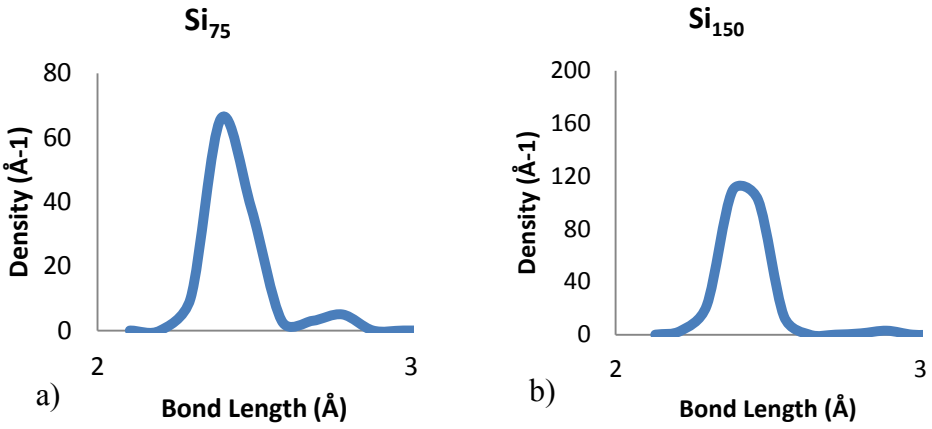

Figure 6: Core Si-Si Bond Length Distributions for Diamond a) Si_{75} and b) Si_{150}.

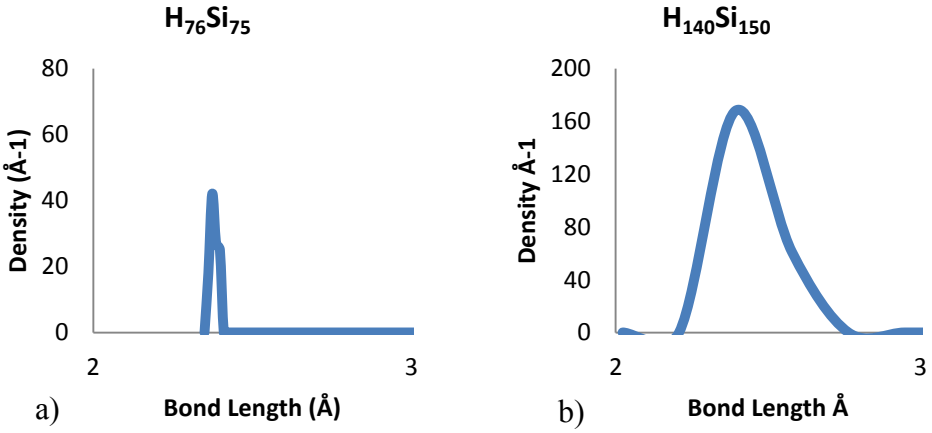

Figure 7: Core Si-Si Bond Length Distributions for Diamond a) $H_{76}Si_{75}$ and b) $H_{140}Si_{150}$

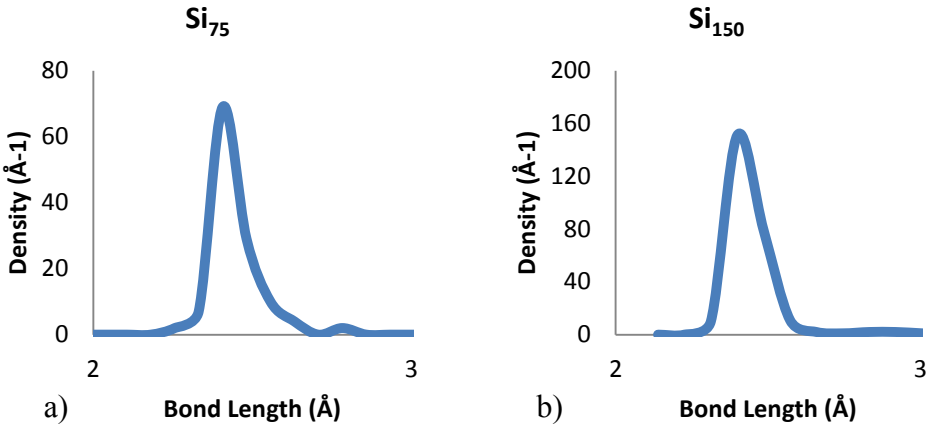

Figure 8: Core Si-Si Bond Length Distributions for Wurtzite a) Si_{75} and b) Si_{150}

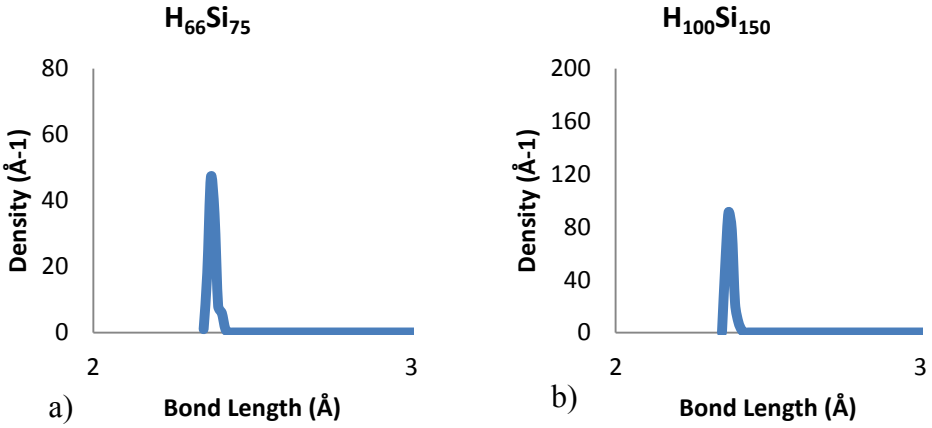

Figure 9: Core Si-Si Bond Length Distributions for Wurtzite a) $H_{66}Si_{75}$ and b) $H_{100}Si_{150}$

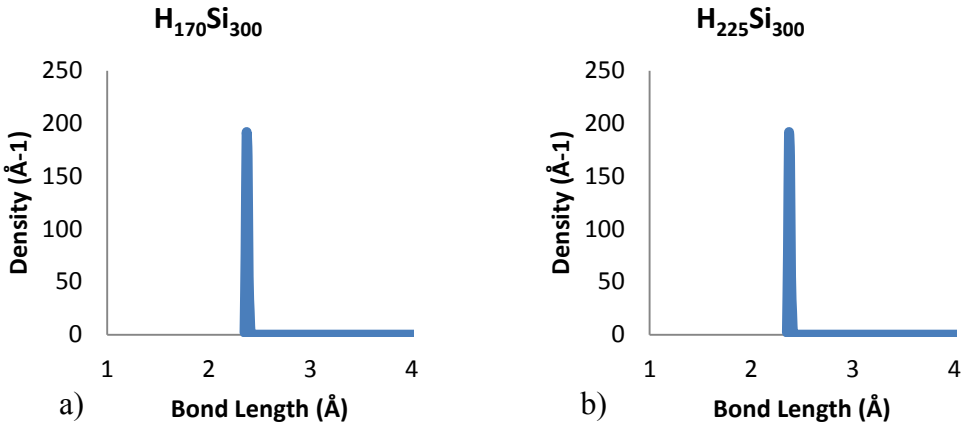

Figure 10: Core Si-Si Bond Length Distributions for a) Wurtzite $H_{170}Si_{300}$ and b) Diamond $H_{225}Si_{300}$

4.2 Electronic Properties

4.2.1 Binding Energies

In Table 4.5 and Table 4.6 we report the binding energies (E_B) per atom and HOMO-LUMO gaps (E_G) of diamond SiNCs and H-SiNCs respectively, in their lowest energy state configurations for singlet and triplet spin states. For each nanocrystal passivated or not, the binding energy per atom difference (ΔE_B) between spin states is just a few meV, so in terms of bond strength the spin state does not make a significant change to stability. However, low energy differences between spin states may be indicative of low magnetic susceptibility. Uniformly all of the diamond SiNCs (H-SiNCs) chose the triplet (singlet) spin state as the lowest energy state. This evidence suggests that adding H atoms to the surface of SiNCs changes the electronic occupations in a way to passivate the intrinsic spin regardless of spin pairing rules. We will discuss in further detail the relationship between spin and H passivation in section 4.2.4.

The resulting redistribution of charge resulting from the H-Si bonding is reflected by the difference in binding energy upon passivation, ΔE_B. When the diamond Si_{75} is passivated with the required 76 H atoms to form $H_{76}Si_{75}$, $\Delta E_B = -94$ meV, and for the diamond Si_{150} passivated with 140 H atoms to form $H_{140}Si_{150}$, $\Delta E_B = 14$ meV.

In Table 4.7 and Table 4.8 we report E_B and E_G for wurtzite SiNCs and H-SiNCs in both spin state configurations. Again the SiNCs (H-SiNCs) uniformly chose the triplet (singlet) spin state as the lowest energy state. For the wurtzite SiNCs there are uniform increases in ΔE_B with respect to the number of Si atoms as anticipated. When the wurtzite Si_{75} is passivated with the required 66 H atoms to form $H_{66}Si_{75}$, $\Delta E_B = -111$

meV. When the wurtzite Si_{150} is passivated with the required 100 H atoms to form $H_{100}Si_{150}$, $\Delta E_B = -97$ meV. The positive change in ΔE_B at each size level is further evidence that the wurtzite geometry is the lowest energy geometry at this size range.

4.2.2 HOMO-LUMO Gaps

The E_G for both diamond and wurtzite structures increase by more than 3.0 eV when passivated with H. This broadening of the E_G is the most recognizable signature of the quantum confined model. Tables 4.5 and 4.7 show that prior to passivation the E_G is much smaller than the bulk E_G value of 1.12 eV which would make the SiNCs near metallic. The concept of purely unpassivated Si structures is a theoretical construct to aid in distinguishing the effects of passivation beyond just satisfying dangling bonds. Indeed the small E_G are due to the surface states that lie above the Fermi energy. However, upon passivation these states are hybridized with H *s* electrons and as expected the resultant surface potential isolates the HOMO and LUMO from the surface, physically and energetically.

Since the surface states are no longer available for occupation the valence electrons are left to occupy fewer states. This enhances quantum confinement to a point in which broadening of the E_G is more prevalent. It should be noted that as the number of Si atoms increases the E_G gets smaller for all SiNCs and H-SiNCs with respect to their spin lowest energy states. When the E_G is compared as a function of size with the spin states fixed, the higher energy spin state has no identifiable relationship with size.

However comparing the E_G with respect to spin state with the sizes fixed the higher energy spin state always has the smaller E_G.

Table 4.5: Binding Energy and HOMO-LUMO Gaps in eV for Unpassivated Diamond Silicon Nanocrystals

Species		Si_{75}		Si_{150}		Si_{300}	
Spinstate		Singlet	Triplet	Singlet	Triplet	Singlet	Triplet
	E_B	-3.051	-3.056	-3.179	-3.182	-3.200	-3.211
	E_G	0.435	0.975	0.575	0.616	0.656	0.606

Table 4.6: Binding Energy and HOMO-LUMO Gaps in eV for Passivated Diamond Silicon Nanocrystals

Species		$H_{76}Si_{75}$		$H_{140}Si_{150}$		$H_{225}Si_{300}$	
Spinstate		Singlet	Triplet	Singlet	Triplet	Singlet	Triplet
	E_B	-3.145	-3.124	-3.168	-3.165	-3.280	-3.259
	E_G	4.680	2.562	3.738	3.297	3.550	0.404

Table 4.7: Binding Energies and HOMO-LUMO Gaps in eV for Unpassivated Wurtzite Silicon Nanocrystals

Species		Si_{75}		Si_{150}		Si_{300}	
Spinstate		Singlet	Triplet	Singlet	Triplet	Singlet	Triplet
	E_B	-3.083	-3.084	-3.195	-3.199	-3.238	-3.243
	E_G	0.947	1.011	0.663	0.864	0.277	0.535

Table 4.8: Binding Energies and HOMO-LUMO Gaps in eV for Passivated Wurtzite Silicon Nanocrystals

Species		$H_{66}Si_{75}$		$H_{100}Si_{150}$		$H_{170}Si_{300}$	
Spinstate		Singlet	Triplet	Singlet	Triplet	Singlet	Triplet
	E_B	-3.195	-3.175	-3.296	-3.283	-3.353	-3.347
	E_G	4.654	3.888	3.911	0.753	3.497	0.580

4.2.3 Frontier Orbitals

The HOMO and LUMO can tell much about the effectiveness of H passivation. The sp^3 hybridization of H-Si bonds creates a surface potential that confines the electronic states to the core of the structure so the localization of the HOMO and LUMO is directly related to the effectiveness of H passivation. In this section we compare the HOMO and LUMO of SiNCs and H-SiNCs to determine the effect of H passivation. In Figures 4.10 – 4.17 the lowest energy state HOMO and LUMO are shown for all of the SiNCs and H-SiNCs. For the SiNCs the HOMO and LUMO are strongly localized in correspondence to the distortions shown in Figures 4.1 – 4.4, which give rise to defect-like states that reside in the E_G. For H-SiNCs the HOMO and LUMO are localized within the core of the structures. This simulates the true effect of quantum confinement.

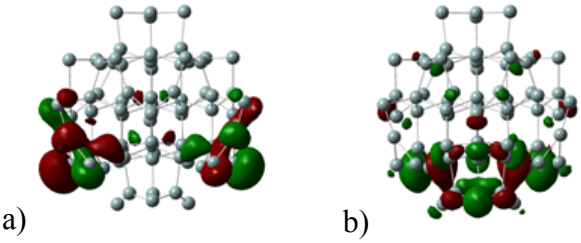

Figure 11: Surface Plots of Diamond Si_{75} a) HOMO and b) LUMO

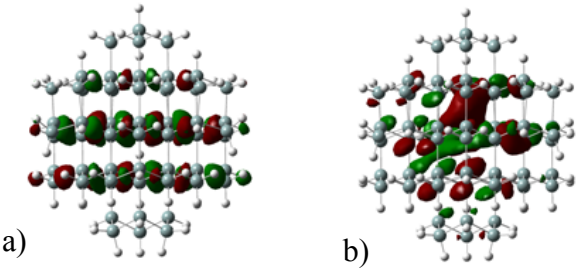

Figure 12: Surface Plots of Diamond $H_{76}Si_{75}$ a) HOMO and b) LUMO

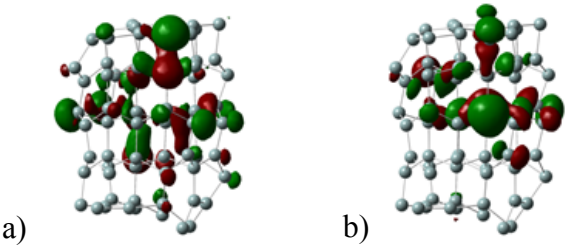

Figure 13: Surface Plots of Wurtzite Si_{75} a) HOMO and b) LUMO

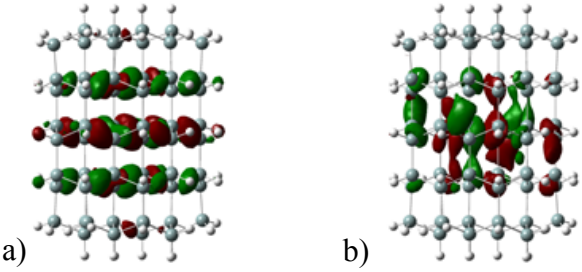

Figure 14: Surface Plots of Wurtzite $H_{66}Si_{75}$ a) HOMO and b) LUMO

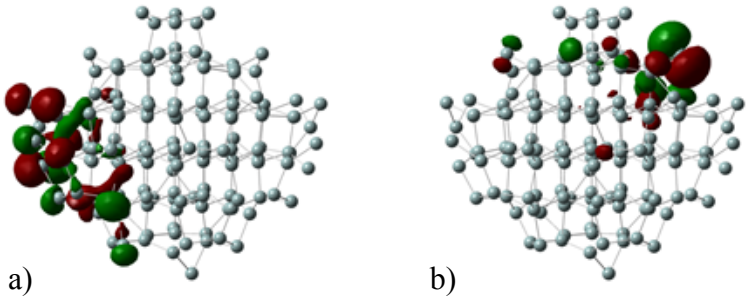

Figure 15: Surface Plots of Diamond Si_{150} a) HOMO and b) LUMO

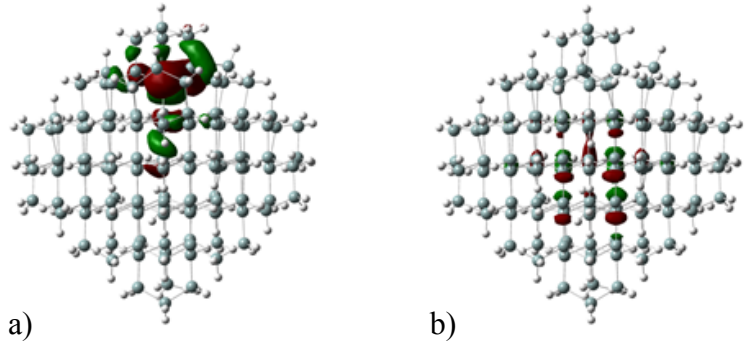

Figure 16: Surface Plots of Diamond $H_{140}Si_{150}$ a) HOMO and b) LUMO

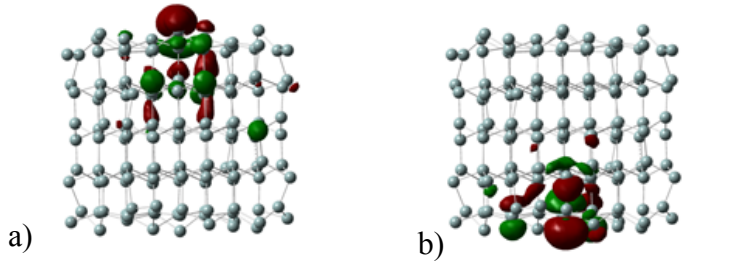

Figure 17: Surface Plots of Wurtzite Si_{150} a) HOMO and b) LUMO.

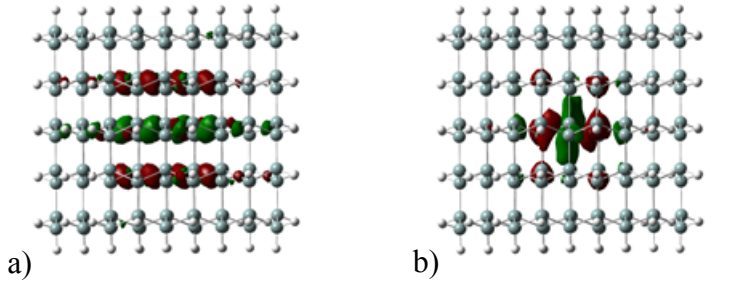

Figure 18: Surface Plots of Wurtzite $H_{100}Si_{150}$ a) HOMO and b) LUMO.

4.2.4 Spin Density

In Figures 4.8 – 4.11 we present spin density plots of the high spin state ($2\mu_B$) SiNCs and H-SiNCs. Based on the determination of the lowest energy state in the previous sections of Chapter 4, the high spin state is the lowest energy state for SiNCs but it is not the lowest energy state for H-SiNCs, because both configurations have an even number of valence electrons they each can take on a singlet or triplet spin state. The information presented gives us an idea how spin states effect surface passivation and vice versa.

In general, molecular orbitals with electrons are filled in the increasing order of their energies according to Aufbau's principle. Then by considering molecular orbitals, like atomic orbitals can only accommodate two electrons with opposite spins (Pauli Exclusion Principle), it is a reasonable expectation that Hund's rule of maximum multiplicity would apply. For the SiNCs, this is exactly the case. For instance, the Si_{75} geometries have 300 valence electrons $\left(75\times[Ne]3s^2 3p^2\right)$ and by Hund's rule there is no electron pairing until all the available orbitals of identical energy are singly occupied. By fixing the spin state in a triplet state we are essentially allocating 151 energy levels for the occupation of say, 151 alpha $(\uparrow)$ electrons and 149 beta $(\downarrow)$ electrons. The difference between alpha and beta electrons is the number of parallel spins remaining, e.g. leaving two electrons with parallel spin. However passivating the structure with the required number of H atoms reduces the total number of valence electrons. In the case of diamond Si_{75} or Si_{150}, we eliminate 76 and 140 valence electrons respectively, leaving 300 – 76 = 224 and 600 – 140 = 460 electrons, respectively. Following the above procedure for maximum multiplicity one would expect the high spin state to be favorable, but we must consider the Pauling scale electronegativity of the atoms competing for the free electrons. Si atoms have an electronegativity of 1.9 versus the H atoms

electronegativity of 2.2. This mismatch in electronegativity makes it favorable for the excess charge to be distributed over the H atoms as opposed to occupying higher energy occupation states. Hence our most stable spin state is the singlet spin state.

The spin densities for all of the SiNCs and H-SiNCs fixed with high spin states have localized spin densities on the surfaces. For the SiNCs the spin densities are expected to be localized on surface atoms because of the surface states that reside there, but for the H-SiNCs the mismatch in electronegativity draws the spin density to the surface. The most probable surface location for the spin density to reside for H-SiNCs is on the localized high density surface state. So far we have determined that the localization of high density surface states is induced by structural defects. Some examples of structural defects are vacancies, dislocations, grain mismatches, or interfacial fragmentation. Notice the fragmentation of a H_2 molecule in Figure 4.11 (right) when the passivated structure is forced to take on a high spin state.

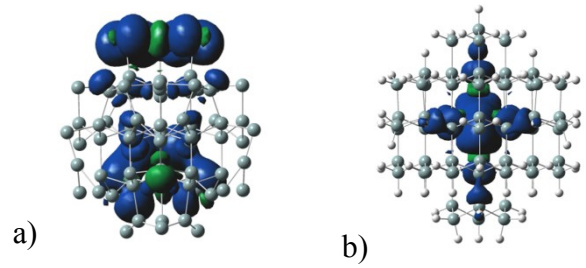

Figure 19: Spin Density Plots of Diamond a) Si_{75} and b) $H_{76}Si_{75}$

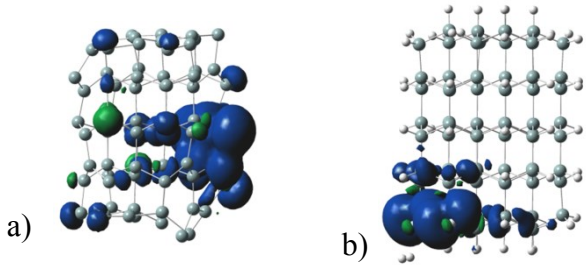

Figure 20: Spin Density Plots of Wurtzite a) Si_{75} and b) $H_{66}Si_{75}$.

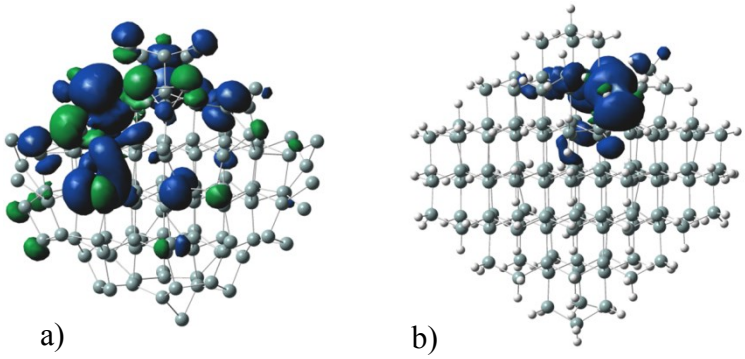

Figure 21: Spin Density Plots of Diamond a) Si_{150} and b) $H_{140}Si_{150}$

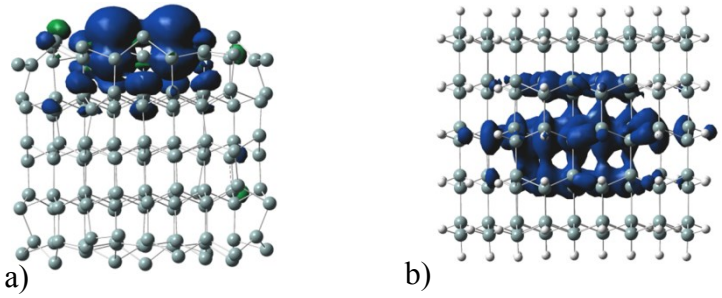

Figure 22: Spin Density Plots of Wurtzite a) Si_{150} and b) $H_{100}Si_{150}$

4.2.5 Density of States

The total electronic density of states for the SiNCs was decomposed into atomic contributions from the surface atoms and core atoms. For H-SiNCs the total electronic DOS was decomposed into atomic contributions from H atoms and Si atoms. By comparing DOS of the SiNCs and the H-SiNCs we can deduce the effect of surface state passivation. A Gaussian broadening of 0.05 eV was used. The Kohn-Sham eigenvalue of the HOMO is subtracted from the energy spectrum so that the Fermi level is set to zero. Since the calculations are spin-unrestricted we give the DOS plots of the majority and minority spin channels in the same figure. Just as suggested by the HOMO and LUMO plots, surface states are prevalent in all of the DOS plots for SiNCs. The LUMO states for SiNCs are lower in energy than the LUMO states of H-SiNCs. For H-SiNCs sp^3 hybridization passivates the surface states and the band edges are pushed apart to have E_G greater than that of bulk Si.

In Figure 4.22 the DOS for the diamond SiNC at the 75 Si atom size level is given. The diamond structure has more surface atoms with multiple dangling bonds which is reflected in the contribution of surface atoms to the DOS. In the valence region the surface atoms dominate the DOS down to -3 eV at which energy the core atoms begin to match the surface atom contributions. From the HOMO LUMO plots we see the HOMO for the diamond Si_{75} is centered on surface atoms. The diamond H-SiNC at the 75 Si atom size level is given in Figure 4.23 the DOS for the diamond H-SiNCs at the 75 Si atom size level is given. By directly comparing the DOS of the passivated and unpassivated structures we determined that strong hybridization of the H and Si electronic levels at -3 eV and 5 eV correspond with widening the of the energy gap.

In Figure 4.24 the DOS for the wurtzite SiNC at the 75 Si atom size level is given. At about 1 eV below the Fermi, 2 eV above the Fermi level, and 5 eV above the Fermi

level we see localized spikes in both spin channels. Comparing to the DOS for the same structure passivated (Figure 4.25) we see strong hybridization of the H and Si electronic levels at -1 eV and 5 eV.

In Figure 4.26 the DOS for the diamond SiNC at the 150 Si atom size level is given. At about 4 eV below the Fermi level, 1.5 eV above the Fermi level, and 4 eV above the Fermi level we see localized spikes in both spin channels. Comparing to the DOS for the same structure passivated (Figure 4.27) we see strong hybridization of the H and Si electronic levels at -4 eV and 4 eV.

In Figure 4.28 the DOS for the wurtzite SiNC at the 150 Si atom size level is given. At about 3 eV below the Fermi, 2 eV above the Fermi level, and 5 eV above the Fermi level we see localized spikes in both spin channels. Comparing to the DOS for the same structure passivated (Figure 4.29) we see strong hybridization of the H and Si electronic levels at -3 eV and 5 eV.

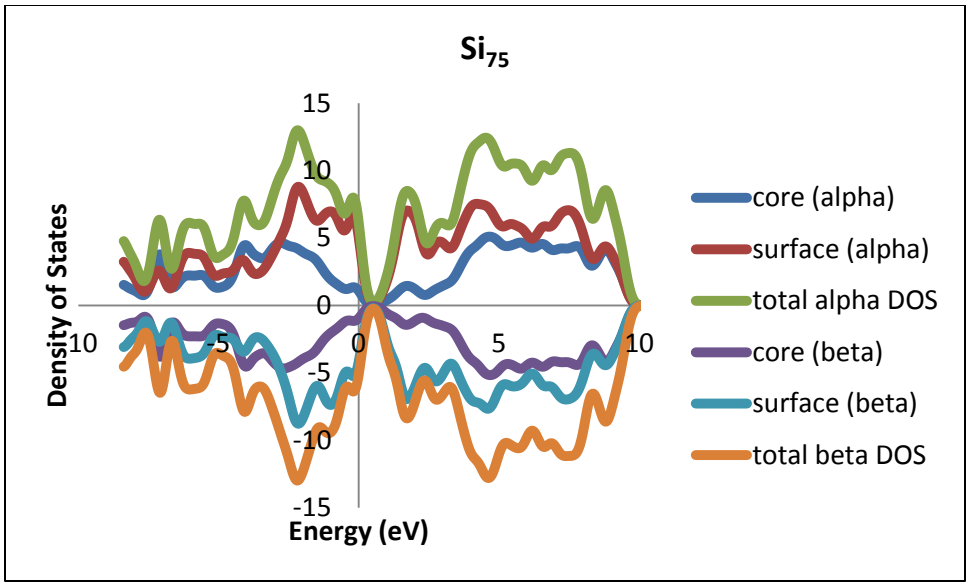

Figure 23: Density of States for Diamond Si_{75}.

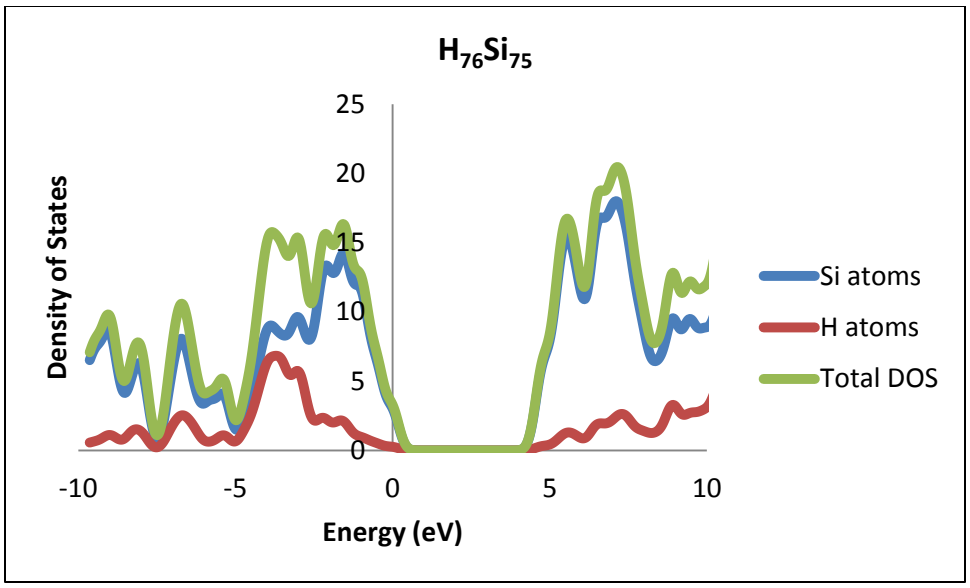

Figure 24: Density of States for Diamond $H_{76}Si_{75}$.

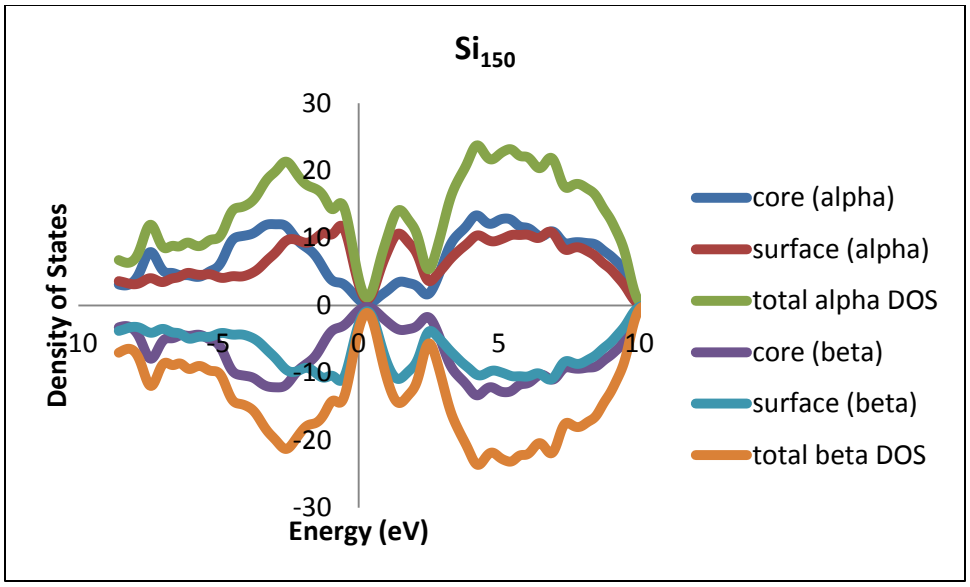

Figure 25: Density of States for Diamond Si_{150}.

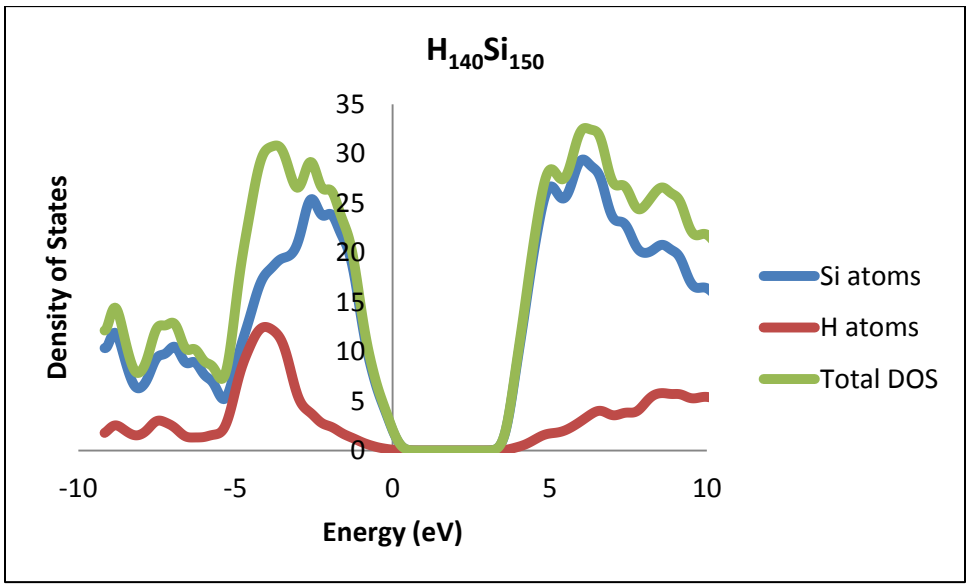

Figure 26: Density of States for Diamond $H_{140}Si_{150}$.

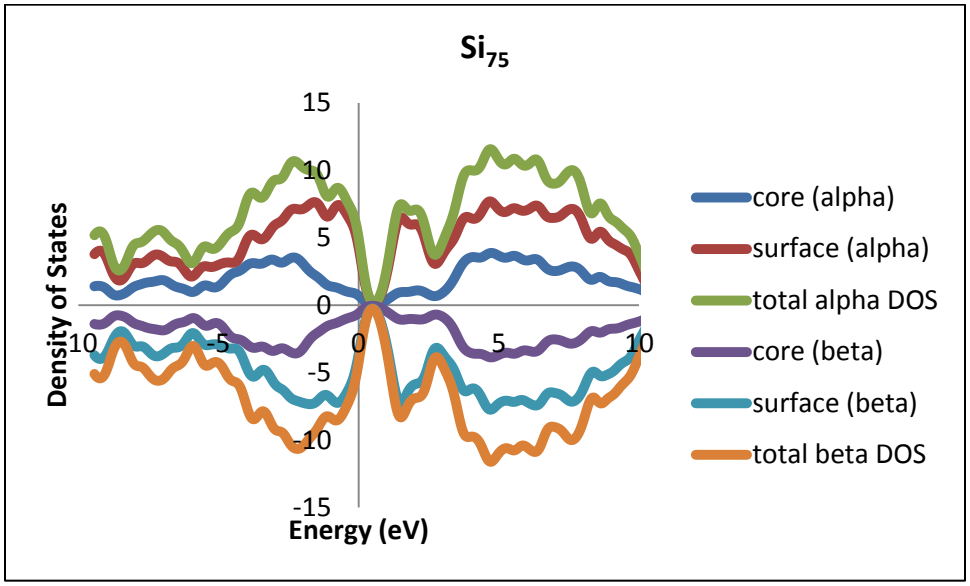

Figure 27: Density of States for Wurtzite Si_{75}.

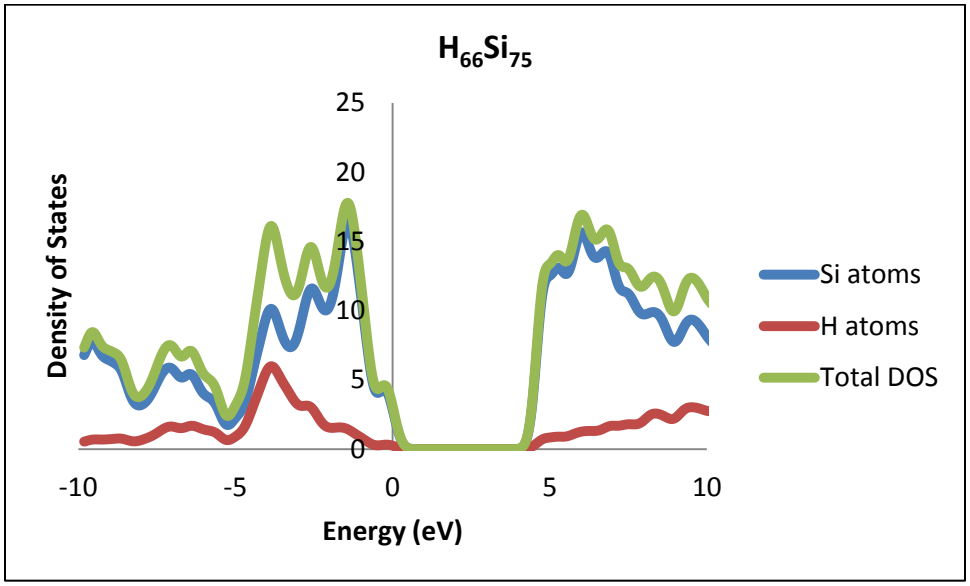

Figure 28: Density of States for Wurtzite $H_{66}Si_{75}$.

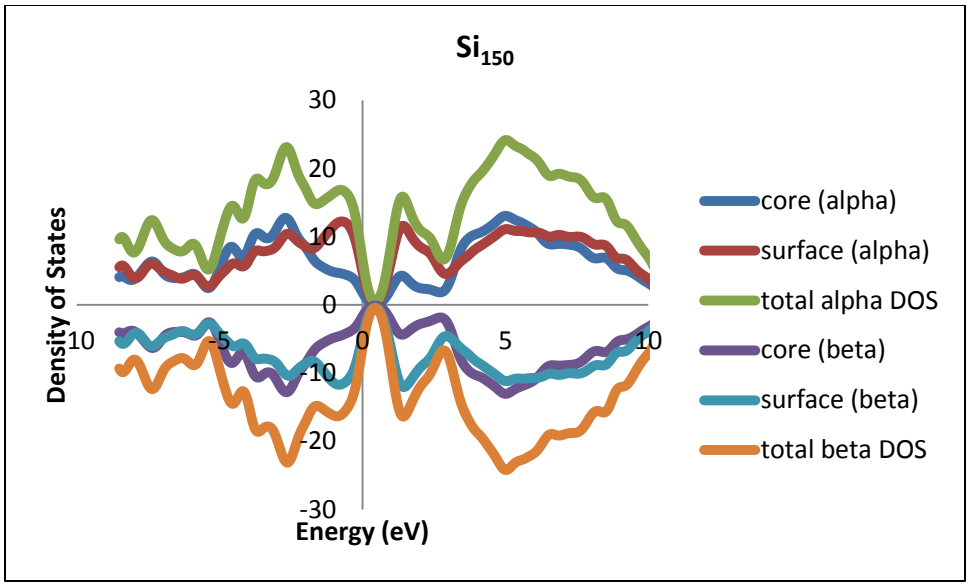

Figure 29: Density of States for Wurtzite Si_{150}.

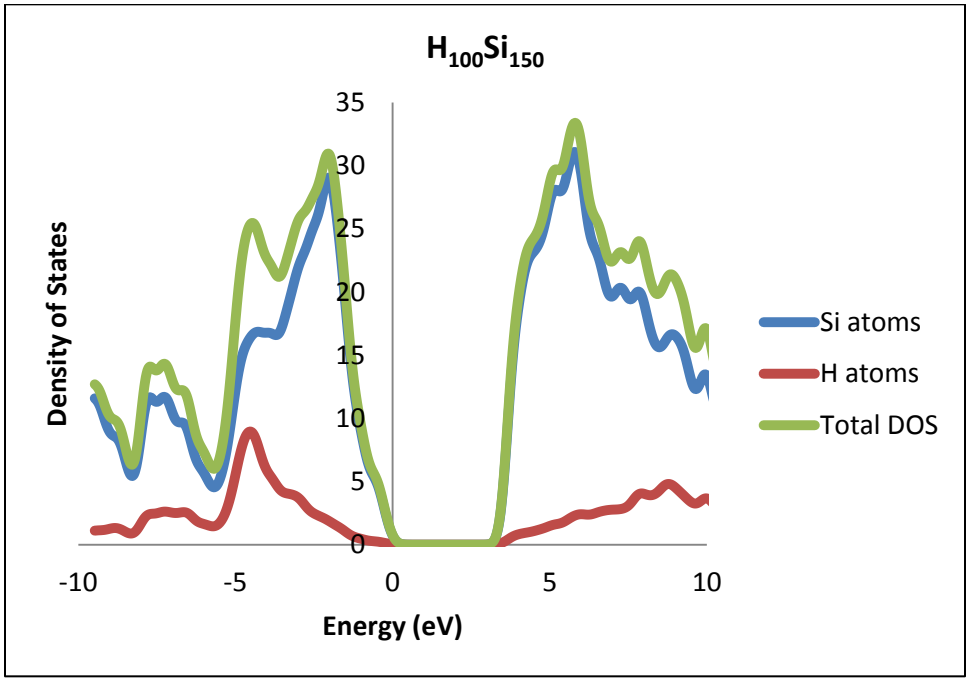

Figure 30: Density of States for Wurtzite $H_{100}Si_{150}$.

Chapter 5

Stability of Doped Passivated Silicon Nanocrystals

5.1 Doping Scheme for the Lowest Energy Geometry

Determination of the lowest energy geometry was carried out in Chapter 4 by considering the effect of H passivation on overall stability of diamond and wurtzite SiNCs.of which the wurtzite structure had the lowest energy at all size levels. Also in Chapter 4 we confirmed that structures with H passivation demonstrated the strongest quantum confined behavior. Therefore here in Chapter 5 we will be discussing noble metal atoms substitutionally doped in the passivated wurtzite structures $H_{66}Si_{75}$, $H_{100}Si_{150}$ and $H_{170}Si_{300}$. Doping of the most stable geometry was done at the three different size levels which consisted of placing the noble metal atoms at different substitutional positions.

In Figure 5.1 the substitutional positions are illustrated. The first substitutional position is a core site (1) which is defined as any interior site that has four-fold coordination. All of the nearest neighbors of a core site are bonded to Si atoms at least one atomic distance from the surface. The second substitutional position is a trough site (2) which is defined as a site that is at most one atomic distance from the surface and is bonded to a core site. Four-fold coordination is preserved at the trough site but the nearest neighbors may be surface atoms that have dangling bonds. The third substitutional position is a crest site (3) which is defined as any surface atom having at least one dangling bond and is also bonded to a trough site. Studying the effects of substitutional doping gives a fundamental understanding of the varying electronic modulations associated with spatial localizations of charge.

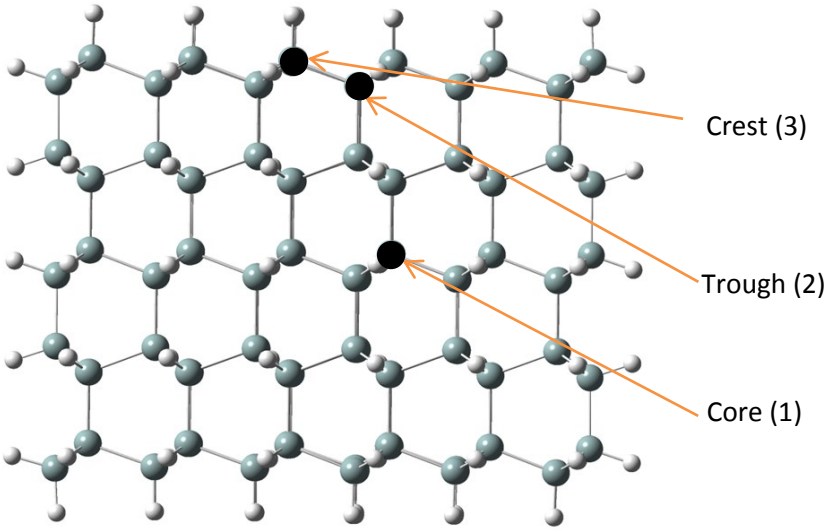

Figure 31: Passivated Wurtzite Silicon Nanocrystal showing (1) Core, (2) Trough and (3) Crest Substitutional Doping Sites.

5.2 Relaxed Geometry

In Figures 5.2 – 5.4 we present the relaxed geometries of $H_{66}Si_{74}X$, $H_{100}Si_{149}X$ and $H_{170}Si_{299}X$, where X = Cu, Ag, Au, to give an indication of how the structure changes with dopant position and number of Si atoms. We acknowledge that the structural distortions will be similar based on ionic radii that are within tenths of an Angstrom among Si and the dopants. Also each of the dopants has a similar electronic configuration, namely a filled *d* shell and half-filled *s* shell.

The doped $H_{66}Si_{74}X$ nanocrystals have the most visible structural distortions for all dopant positions. At the core the dopants give rise to structural deformations at corners where surface atoms have a higher number of dangling bonds. In this case, which is similar for all of the dopants at this location, no reordering of the bonding takes place just expansion and contraction of the bond lengths; four-fold coordination is maintained. Trough site doping has a unique reordering of bonding based on the dopant. For Cu doping the reordering consists of breaking bonds with the two crest atoms that are at least one atomic distance away from an edge or corner. The bonding to the crest atom on the corner (corners have more dangling bonds) and the bonding to the core atom are preserved with the exceptions of expansions and contractions of the bonds. For Ag doping all bonds are broken except for the bond with the crest atom on the corner of the structure. Au doping is done without reordering the bonds but the bonds with crest atoms on the corners are appreciably elongated. Finally for crest site doping, Each dopant has a similar effect. In nearly each case, the dopants break the bond with H and a trough atom, leaving two-fold coordination.

The doped $H_{100}Si_{149}X$ nanocrystals exhibit more stabilized doping but some distortions are visible. At the core the dopants relax into the substitutional position without noticeable distortions to the bonding. Four-fold coordination is maintained at the core.

Doping X atom at the trough site, has a screened interaction with the surface potential and in some case irrespective to size or dopant four-fold coordination is elusive. For crest site doping Cu and Ag have a similar effect on the local bonding. The bonds of Cu and Ag to the H atom are broken but the other coordination is maintained. Au doping however, is unique and does not reorder bonds based simply on iconicity mismatches; the s electron in this dopant moves appreciable close to the speed of light.

The doped $H_{170}Si_{299}X$ nanocrystals have even higher stability than the previous two sizes. The increase in stability directly corresponds to a decrease in structural distortions. X atoms relaxed into the core of this structure without any noticeable differences in bond lengths. X atoms relaxed into the trough site are more stabilized than the previous two sizes simply because high surface state density atoms which can invariably be atoms on the corners and edges of the structure. X atoms relaxed into the crest site are more stabilized than the previous two sizes for the same reason. Because of the ionic properties of the dopants visual inspection of the stabilities is elusive. A more dependable analysis of the stability must come from the electronic properties. In the remainder of Chapter 5 we will discuss in detail the energetic profile of each doped system.

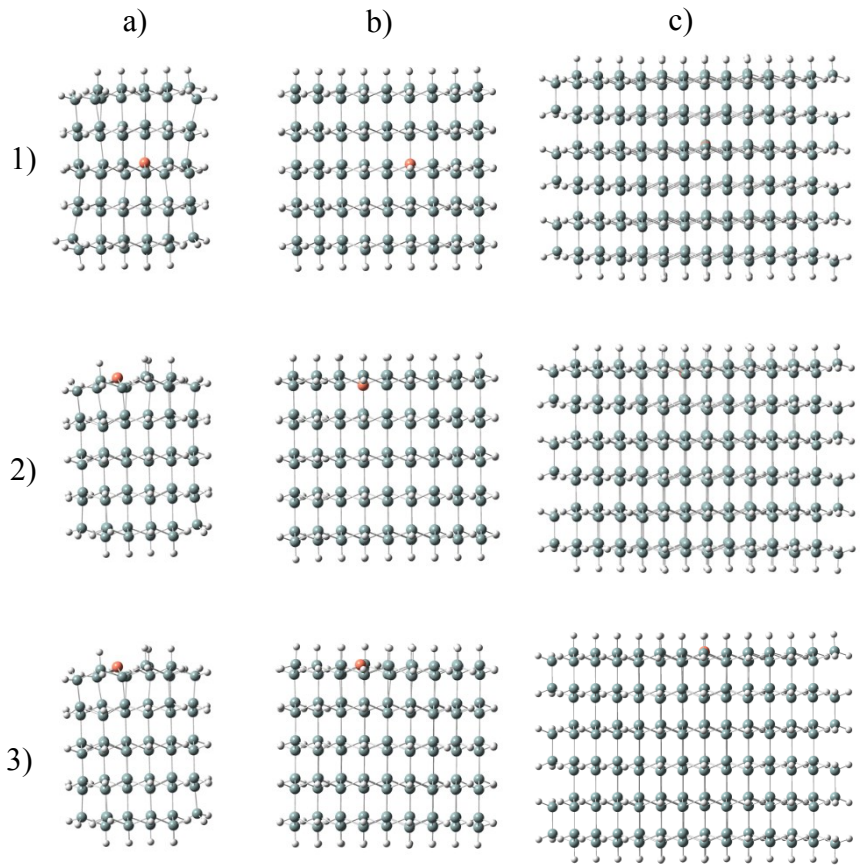

Figure 32 : Relaxed Geometry of a) $H_{66}Si_{74}Cu$, b) $H_{100}Si_{149}Cu$ and c) $H_{170}Si_{299}Cu$ with Cu at the 1) core, 2) trough, and 3) crest doping sites.

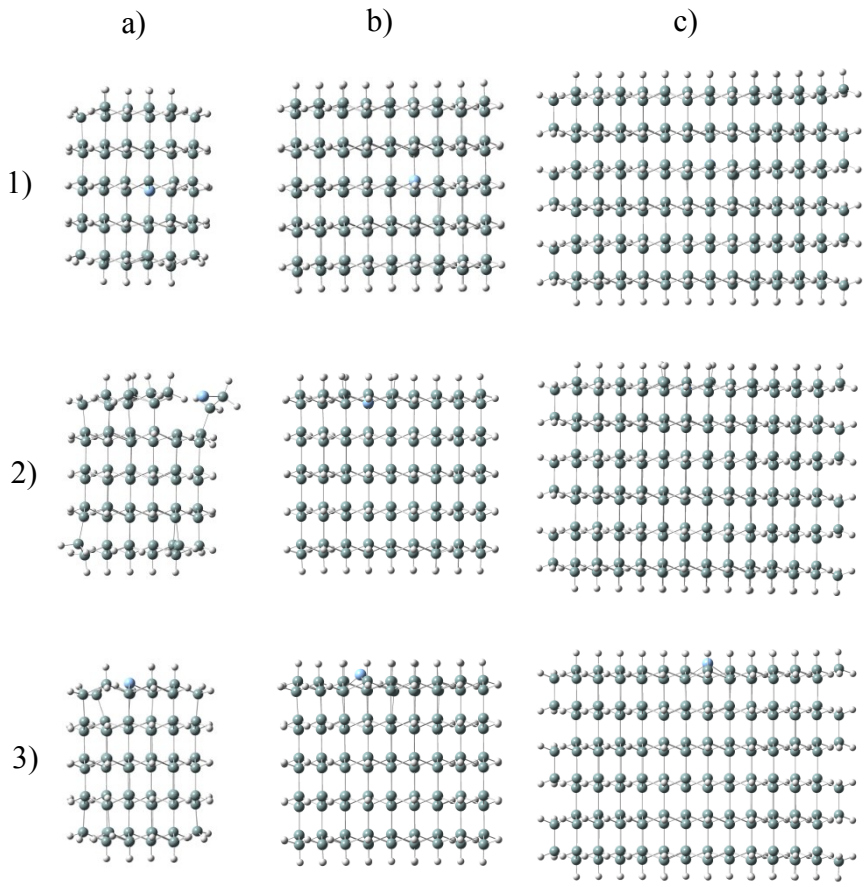

Figure 33 : Relaxed Geometry of a) $H_{66}Si_{74}Ag$, b) $H_{100}Si_{149}Ag$ and c) $H_{170}Si_{299}Ag$ with Ag at the 1) core, 2) trough, and 3) crest doping sites.

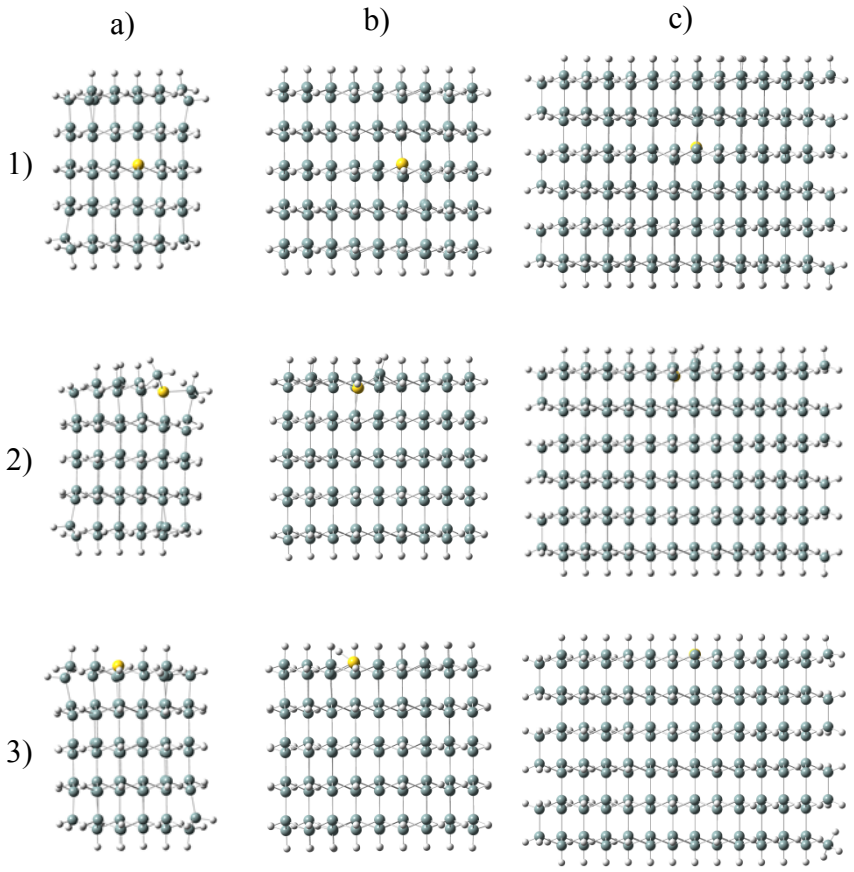

Figure 34 : Relaxed Geometry of a) $H_{66}Si_{74}Au$, b) $H_{100}Si_{149}Au$ and c) $H_{170}Si_{299}Au$ with Au at 1) core, 2) trough, and 3) crest doping sites.

5.3 Doped Electronic Properties

5.3.1 Effect of Noble Metal Dopants on Magnetic Moments

Previously in Chapter 4 we discovered that all of the H passivated silicon nanocrystals (H-SiNCs) had a complete quenching of the magnetic moments even though by Hund's rule they should have had high spin magnetic moments. In this doping section we are introducing noble metal atom dopants to these H-SiNCs with quenched magnetic moments. Then by considering variant ionic bonding in the cases of substitutional Cu doping (+1 or +2 charge states), Ag doping (+1 charge state) or Au doping (+1 or +3 charge states) in place of Si (+2 or +4 charge state), we realize doping can result in the system being electron deficient or electron excessive. Therefore predicting the stabilization of magnetic moments via Hund's rule is a dubious task.

In Tables 5.1 – 5.9 we report the total energies of $H_{66}Si_{74}X$, $H_{100}Si_{149}X$ and $H_{170}Si_{299}X$ where X = Cu, Ag, Au. For each dopant we have the energy levels for a high (3 μ_B) and a low (1 μ_B) spin state. Since the dopants can be n- or p-type depending on the ionic environment we expect some level of magnetic susceptibility. Coupling of this susceptibility with the quenching of H passivation is indeed a complicated task. However, to this end, we simulated fine structure splitting by calculating the differences between the high and low spin state energy levels. Our lowest energy spin state was determined by observing which spin state had the lowest energy. Then a spin state transition is defined as going from the lowest energy spin state to the highest energy spin state.

The energy difference (ΔE_S) associated with a spin state transition is then the difference between the lowest energy and the highest energy spin states. ΔE_S is a quantity that is always negative by definition and its magnitude indicates the amount of energy required to the flip spin of the system.

For $H_{66}Si_{74}X$ core site doping offers little in terms of total energy differences. For instance, in Cu doping the low spin state has a more stable energy than the high spin state by approximately $\Delta E_s = -48$ meV, so the doublet state is the lowest energy state in this case. For Ag doping, $\Delta E_s = -147$ meV favoring the quartet spin state For Au doping, $\Delta E_s = -26$ meV favoring the doublet spin state. At the trough site, for all of the dopants, the magnetic moment for each of the structures is the doublet spin state. For Cu $\Delta E_s = -968$ meV, for Ag $\Delta E_s = -1.085$ eV, and for Au $\Delta E_s = -653$ meV. At the crest site, again all the dopants relax into doublet spin state. For Cu $\Delta E_s = -2.162$ eV, for Ag $\Delta E_s = -2.520$ eV, and for Au $\Delta E_s = -2.302$ eV. For the 75 Si atom size level as the dopant moves closer to the surface the magnitude of ΔE_S is significantly increasing.

For $H_{100}Si_{149}X$ at the core site there are small differences in the energy between the spin states, but for each dopant in the core the quartet spin state is identified as the lowest energy spin state. For Cu doping $\Delta E_S = -136$ meV, for Ag doping $\Delta E_s = -152$ meV, and for Au doping, $\Delta E_s = -35$ meV. Then at the trough site the quartet spin state is favored for all dopants except Au, which chose the doublet spin state as its lowest energy state. For Cu $\Delta E_s = -150$ meV, for Ag $\Delta E_s = -107$ meV, and for Au $\Delta E_s = -66$ meV. At the crest site all the dopants relax into a doublet spin state. For Cu $\Delta E_s = -1.844$ eV, for Ag $\Delta E_s = -1.919$ eV, and for Au $\Delta E_s = -1.122$ eV. For the 150 Si atom size level the differences in spin state energy showed small differences for

the core and trough site but at the crest site ΔE_S is an order of magnitude larger at the crest site for all of the dopants..

For $H_{170}Si_{299}X$ at the core site again the differences between spin state energy are small however, the quartet spin state is identified as the lowest energy state. For Cu $\Delta E_s = -106$ meV, for Ag $\Delta E_s = -127$ meV, and for Au $\Delta E_s = -26$ meV. At the trough site the quartet spin state is favored for all dopants except Au, which chose the doublet spin state as its lowest energy state. For Cu $\Delta E_s = -11$ meV, for Ag $\Delta E_s = -63$ meV, and for Au $\Delta E_s = -108$ meV. At the crest site all dopants relax into a doublet spin state. For Cu $\Delta E_s = -1.790$ eV, for Ag $\Delta E_s = -1.884$ eV, and for Au $\Delta E_s = -1.461$ eV. Overall we see increases in spin state transition energy as the dopant moves toward the surface.

Table 5.1: Total Energies in eV of $H_{66}Si_{74}Cu$, $H_{100}Si_{149}Cu$ and $H_{170}Si_{299}Cu$: the Core Site

Species	**$H_{66}Si_{74}Cu$**		**$H_{100}Si_{149}Cu$**		**$H_{170}Si_{299}Cu$**	
Spin state	Doublet	Quartet	Doublet	Quartet	Doublet	Quartet
	-14256.948	-14256.900	-22772.785	-22772.921	-39836.554	-39836.660

Table 5.2: Total Energies in eV of $H_{66}Si_{74}Cu$, $H_{100}Si_{149}Cu$ and $H_{170}Si_{299}Cu$: the Trough Site

Species	**$H_{66}Si_{74}Cu$**		**$H_{100}Si_{149}Cu$**		**$H_{170}Si_{299}Cu$**	
Spin state	Doublet	Quartet	Doublet	Quartet	Doublet	Quartet
	-14257.411	-14256.443	-22772.435	-22772.585	39836.339	39836.350

Table 5.3: Total Energies in eV of $H_{66}Si_{74}Cu$, $H_{100}Si_{149}Cu$ and $H_{170}Si_{299}Cu$: the Crest Site

Species	**$H_{66}Si_{74}Cu$**		**$H_{100}Si_{149}Cu$**		**$H_{170}Si_{299}Cu$**	
Spin state	Doublet	Quartet	Doublet	Quartet	Doublet	Quartet
	-14258.034	-14255.872	-22773.818	-22771.974	39837.470	-39835.680

Table 5.4: Total Energies in eV of $H_{66}Si_{74}Ag$, $H_{100}Si_{149}Ag$ and $H_{170}Si_{299}Ag$: the Core Site

Species	**$H_{66}Si_{74}Ag$**		**$H_{100}Si_{149}Ag$**		**$H_{170}Si_{299}Ag$**	
Spin state	Doublet	Quartet	Doublet	Quartet	Doublet	Quartet
	-12885.379	-12885.553	-21401.318	-21401.1470	-38465.045	-38465.172

Table 5.5: Total Energies in eV of $H_{66}Si_{74}Ag$, $H_{100}Si_{149}Ag$ and $H_{170}Si_{299}Ag$: the Trough Site

Species	**$H_{66}Si_{74}Ag$**		**$H_{100}Si_{149}Ag$**		**$H_{170}Si_{299}Ag$**	
Spin state	Doublet	Quartet	Doublet	Quartet	Doublet	Quartet
	-12886.317	-12885.232	-21401.108	-21401.215	-38464.901	38464.964

Table 5.6: Total Energies in eV of $H_{66}Si_{74}Ag$, $H_{100}Si_{149}Ag$ and $H_{170}Si_{299}Ag$: the Crest Site

Species	**$H_{66}Si_{74}Ag$**		**$H_{100}Si_{149}Ag$**		**$H_{170}Si_{299}Ag$**	
Spin state	Doublet	Quartet	Doublet	Quartet	Doublet	Quartet
	-12887.098	-12884.578	-21402.435	-21400.516	-38466.144	-38464.260

Table 5.7: Total Energies in eV of $H_{66}Si_{74}Au$, $H_{100}Si_{149}Au$ and $H_{170}Si_{299}Au$: the Core Site

Species	**$H_{66}Si_{74}Au$**		**$H_{100}Si_{149}Au$**		**$H_{170}Si_{299}Au$**	
Spin state	Doublet	Quartet	Doublet	Quartet	Doublet	Quartet
	-12605.845	-12605.819	-21121.731	-21121.510	-38185.447	-38185.473

Table 5.8: Total Energies in eV of $H_{66}Si_{74}Au$, $H_{100}Si_{149}Au$ and $H_{170}Si_{299}Au$: the Trough Site

Species	**$H_{66}Si_{74}Au$**		**$H_{100}Si_{149}Au$**		**$H_{170}Si_{299}Au$**	
Spin state	Doublet	Quartet	Doublet	Quartet	Doublet	Quartet
	-12886.317	-12885.232	-21401.108	21401.215	-38464.901	38464.964

Table 5.9: Total Energies of $H_{66}Si_{74}Au$, $H_{100}Si_{149}Au$ and $H_{170}Si_{299}Au$: the Crest Site

Species	**$H_{66}Si_{74}Au$**		**$H_{100}Si_{149}Au$**		**$H_{170}Si_{299}Au$**	
Spin state	Doublet	Quartet	Doublet	Quartet	Doublet	Quartet
	-12607.158	-12604.856	-21121.974	-21120.825	-38186.042	-38184.581

5.3.2 Binding Energy

In Tables 5.10 – 5.18 we present the binding energy per atom (E_B) and HOMO-LUMO gaps (E_G) of $H_{66}Si_{74}X$, $H_{100}Si_{149}X$ and $H_{170}Si_{299}X$, where X = Cu, Ag, Au. We compared the E_B of each of the doped structures to the undoped structure of similar size and passivation. Then we study the overall change in stability with increasing size. Finally we study the binding as a function of dopant and note the E_G. The comparisons are carried out at each size level to study the overall effect of doping on the stability of the prototype structure.

For $H_{66}Si_{74}X$ we find a uniform reduction in stability upon doping of the structures on the order of hundredths of an electron volt. Reduction in stability is part of the cost for replacing a Si atom with a larger NMA. Doping X at the core site has the largest cost for substitutional doping. The Cu and Au atom have similar E_B and are always more stable than Ag doping. As the X atom dopant is moved from the core to the surface stability increases are on the order of thousandths of an electron volt. For $H_{100}Si_{149}X$ we see a similar trend in stability as we saw in the previous case. When compared to the same structure without doping X atom we find a uniform reduction in binding energy on the order of hundredths of electron volt. However compared to the smaller doped structures we observe an increase in stability on the order of tenths of an electron volt. For $H_{170}Si_{299}X$, just as in the previous cases the binding energy decreases upon doping the structures. The relative stability of Cu and Au at any of the dopant sites are of negligible difference. To better describe the stability cost in replacing a Si atom with a dopant will be covered in greater detail when we discuss the relative formation energies in section 5.3.4.

5.3.3 HOMO-LUMO Gaps

Observing the HOMO LUMO Gaps given in Tables 5.10 – 5.18 we see for the doped H-SiNCs a trend associated with size. Holding the dopant, position and magnetic moments fixed the HOMO LUMO gap decreases with size. This behavior is dictated by quantum confinement effect. In the doublet spin state all of the E_G are all less than 2 eV, this evidence suggests that ideal quantum confined behavior is sensitive to magnetic moments. This relationship is further evidenced by the wide gap behavior being realized for the quartet spin state in all cases.

The interplay of magnetic moments with noble metal atom doping is very important for particular properties. For instance the Cu dopant at the core site we see small E_G at the 75 Si atom size level. However since the lowest energy state is pseudo degenerate with the quartet state (the energy differences are on the order of just a few meV) it is safe to say at the 75 Si atom size level the arrangement for magnetic moments favors the low spin state because the dopants behave as additional charge recepticles. The established quenching of magnetic moments associated with H passivation is complemented by the presence of the dopant in the core except for Ag which must be a donor in this case.

At the trough site especially at the 150 Si atom size level the effect of the dopant having a nearest neighbor bonded to a passivant H atom is shown to decrease the gap below the value for bulk Si. For Ag atom doping at the trough the low spin state contracts the gap and the Au atom doping has small differences in gap with respect to spin state. Of the dopants, Au has the propensity to behave as if it has more than one valence electron. The higher order valence of Au explains why the stabilization of electronic spin has small differences in gap between the magnetic moments.

At the crest site all dopants have E_G greater than the bulk band gap regardless of spin state. At each dopant position the E_G are decreasing with respect to dopant where the Au dopant has the smallest gap. For charge distributed on the surface the introduction of additional charge from the noble metal atom dopant gives rise to an electric dipole. Doping at the crest site would mean a smaller dipole and therefore a smaller potential barrier for the dopant to overcome in order to stabilize in the substitutional position.

Table 5.10: Binding Energy and HOMO-LUMO gaps in eV of $H_{66}Si_{74}Cu$, $H_{100}Si_{149}Cu$ and $H_{170}Si_{299}Cu$: the Core Site

Species		**$H_{66}Si_{74}Cu$**		**$H_{100}Si_{149}Cu$**		**$H_{170}Si_{299}Cu$**	
Spin state		Doublet	Quartet	Doublet	Quartet	Doublet	Quartet
	E_B	-3.163	-3.163	-3.278	-3.279	-3.344	-3.344
	E_G	1.736	3.882	1.317	3.457	1.377	3.121

Table 5.11: Binding Energy and HOMO-LUMO gaps in eV of $H_{66}Si_{74}Cu$, $H_{100}Si_{149}Cu$ and $H_{170}Si_{299}Cu$: the Trough Site

Species		**$H_{66}Si_{74}Cu$**		**$H_{100}Si_{149}Cu$**		**$H_{170}Si_{299}Cu$**	
Spin state		Doublet	Quartet	Doublet	Quartet	Doublet	Quartet
	E_B	-3.167	-3.160	-3.277	-3.278	-3.343	-3.343
	E_G	3.582	4.094	1.581	3.581	1.435	3.294

Table 5.12: Binding Energy and HOMO-LUMO gaps in eV of $H_{66}Si_{74}Cu$, $H_{100}Si_{149}Cu$ and $H_{170}Si_{299}Cu$: the Crest Site

Species		**$H_{66}Si_{74}Cu$**		**$H_{100}Si_{149}Cu$**		**$H_{170}Si_{299}Cu$**	
Spin state		Doublet	Quartet	Doublet	Quartet	Doublet	Quartet
	E_B	-3.171	-3.156	-3.282	-3.275	-3.346	-3.342
	E_G	3.738	4.073	3.208	3.530	3.025	3.231

Table 5.13: Binding Energy and HOMO-LUMO gaps in eV of $H_{66}Si_{74}Ag$, $H_{100}Si_{149}Ag$ and $H_{170}Si_{299}Ag$: the Core Site

Species		**$H_{66}Si_{74}Ag$**		**$H_{100}Si_{149}Ag$**		**$H_{170}Si_{299}Ag$**	
Spin state		Doublet	Quartet	Doublet	Quartet	Doublet	Quartet
	E_B	-3.154	-3.156	-3.274	-3.274	-3.341	-3.342
	E_G	1.394	3.642	1.355	3.283	1.377	2.954

Table 5.14: Binding Energy and HOMO-LUMO gaps in eV of $H_{66}Si_{74}Ag$, $H_{100}Si_{149}Ag$ and $H_{170}Si_{299}Ag$: the Trough Site

Species		**$H_{66}Si_{74}Ag$**		**$H_{100}Si_{149}Ag$**		**$H_{170}Si_{299}Ag$**	
Spin state		Doublet	Quartet	Doublet	Quartet	Doublet	Quartet
	E_B	-3.161	-3.153	-3.273	-3.273	-3.341	-3.341
	E_G	3.726	3.925	0.909	3.480	1.468	3.180

Table 5.15: Binding Energy and HOMO-LUMO gaps in eV of $H_{66}Si_{74}Ag$, $H_{100}Si_{149}Ag$ and $H_{170}Si_{299}Ag$: the Crest Site

Species		**$H_{66}Si_{74}Ag$**		**$H_{100}Si_{149}Ag$**		**$H_{170}Si_{299}Ag$**	
Spin state		Doublet	Quartet	Doublet	Quartet	Doublet	Quartet
	E_B	-3.167	-3.149	-3.278	-3.271	-3.344	-3.340
	E_G	3.541	3.924	2.805	3.358	2.643	3.063

Table 5.16: Binding Energy and HOMO-LUMO gaps in eV of $H_{66}Si_{74}Au$, $H_{100}Si_{149}Au$ and $H_{170}Si_{299}Au$: the Core Site

Species		**$H_{66}Si_{74}Au$**		**$H_{100}Si_{149}Au$**		**$H_{170}Si_{299}Au$**	
Spin state		Doublet	Quartet	Doublet	Quartet	Doublet	Quartet
	E_B	-3.163	-3.163	-3.279	-3.279	-3.344	-3.344
	E_G	1.610	3.590	1.422	3.220	1.286	2.903

Table 5.17: Binding Energy and HOMO-LUMO gaps in eV of $H_{66}Si_{74}Au$, $H_{100}Si_{149}Au$ and $H_{170}Si_{299}Au$: the Trough Site

Species		**$H_{66}Si_{74}Au$**		**$H_{100}Si_{149}Au$**		**$H_{170}Si_{299}Au$**	
Spin state		Doublet	Quartet	Doublet	Quartet	Doublet	Quartet
	E_B	-3.165	-3.161	-3.278	-3.278	-3.344	-3.344
	E_G	2.285	3.853	1.577	1.050	1.481	3.091

Table 5.18: Binding Energy and HOMO-LUMO gaps in eV of $H_{66}Si_{74}Au$, $H_{100}Si_{149}Au$ and $H_{170}Si_{299}Au$: the Crest Site

Species		**$H_{66}Si_{74}Au$**		**$H_{100}Si_{149}Au$**		**$H_{170}Si_{299}Au$**	
Spin state		Doublet	Quartet	Doublet	Quartet	Doublet	Quartet
	E_B	-3.173	-3.156	-3.279	-3.275	-3.345	-3.342
	E_G	3.449	3.835	2.131	3.303	2.665	3.012

5.3.4 Formation Energy

The formation energy of a dopant in H-SiNCs determines the dopant solubility in a host at a given growth condition or chemical potential. High formation energy corresponds to low solubility. In Tables 5.19 – 5.27 the formation energies are listed for each impurity with respect to dopant position and nanocrystal size. Overall the formation of dopants in the H-SiNCs at this size range is not likely at equilibrium conditions, however clear trends in formation energy can be extrapolated from this data. For instance, as the dopant is moved from the core to the crest position formation energy decreases showing a higher favorability for dopant atoms on the surfaces.

At the core site we see for Cu, Ag and Au, that as the number of Si atoms increases the formation energies decrease. For example Ag doping in the core at the 75 Si atom size level comes at formation energy of 5.498 eV and decreases by 20 meV when the size is doubled to 150 Si atoms. From 150 Si atoms to 300 the decrease in formation energy is approximately 10 meV. This indicates a trend for the formation energies that converges to a minimum value as we approach the bulk regime.

At the trough site this trend is interrupted due to the interaction with the passivant atom bonded to its nearest neighbor. This explanation makes sense because at different spin multiplicities the trend is preserved. This relative ease of dopant formation with respect to a change in spin multiplicity indicates that formation of the dopants may be facilitated better in an external field.

At the crest site the dopant atom is directly bonded with the passivant H atom. For each dopant at each size the doublet spin state has the lowest energy in terms of stability as seen by the binding energies in the previous section. In terms of formation energy the doublet spin state uniformly has values approximately 40 percent less than the formation energies calculated in the quartet spin state. The mechanism associated

with quenching the magnetic moments upon passivation is affected by the dopants. As seen in Figures 5.2 – 5.4 doping at the crest site is more stable when the bond to the passivant atom is broken.

Table 5.19: Formation Energy in eV of $H_{66}Si_{74}Cu$, $H_{100}Si_{149}Cu$ and $H_{170}Si_{299}Cu$: the Core Site

Species		$H_{66}Si_{74}Cu$		$H_{100}Si_{149}Cu$		$H_{170}Si_{299}Cu$	
Spin state		Doublet	Quartet	Doublet	Quartet	Doublet	Quartet
	E_F	4.418	4.466	4.471	4.336	4.391	4.285

Table 5.20: Formation Energy in eV of $H_{66}Si_{74}Cu$, $H_{100}Si_{149}Cu$ and $H_{170}Si_{299}Cu$: the Trough Site

Species		$H_{66}Si_{74}Cu$		$H_{100}Si_{149}Cu$		$H_{170}Si_{299}Cu$	
Spin state		Doublet	Quartet	Doublet	Quartet	Doublet	Quartet
	E_F	3.955	4.923	4.821	4.672	4.606	4.595

Table 5.21: Formation Energy in eV of $H_{66}Si_{74}Cu$, $H_{100}Si_{149}Cu$ and $H_{170}Si_{299}Cu$: the Crest Site

Species		$H_{66}Si_{74}Cu$		$H_{100}Si_{149}Cu$		$H_{170}Si_{299}Cu$	
Spin state		Doublet	Quartet	Doublet	Quartet	Doublet	Quartet
	E_F	3.332	5.494	3.439	5.282	3.475	5.264

Table 5.22: Formation Energy in eV of $H_{66}Si_{74}Ag$, $H_{100}Si_{149}Ag$ and $H_{170}Si_{299}Ag$: the Core Site

Species		**$H_{66}Si_{74}Ag$**		**$H_{100}Si_{149}Ag$**		**$H_{170}Si_{299}Ag$**	
Spin state		Doublet	Quartet	Doublet	Quartet	Doublet	Quartet
	E_F	5.672	5.498	5.624	5.471	5.585	5.458

Table 5.23: Formation Energy in eV of $H_{66}Si_{74}Ag$, $H_{100}Si_{149}Ag$ and $H_{170}Si_{299}Ag$: the Trough Site

Species		**$H_{66}Si_{74}Ag$**		**$H_{100}Si_{149}Ag$**		**$H_{170}Si_{299}Ag$**	
Spin state		Doublet	Quartet	Doublet	Quartet	Doublet	Quartet
	E_F	4.734	5.820	5.833	5.726	5.729	5.666

Table 5.24: Formation Energy in eV of $H_{66}Si_{74}Ag$, $H_{100}Si_{149}Ag$ and $H_{170}Si_{299}Ag$: the Crest Site

Species		**$H_{66}Si_{74}Ag$**		**$H_{100}Si_{149}Ag$**		**$H_{170}Si_{299}Ag$**	
Spin state		Doublet	Quartet	Doublet	Quartet	Doublet	Quartet
	E_F	3.954	6.473	4.506	6.426	4.486	6.370

Table 5.25: Formation Energy in eV of $H_{66}Si_{74}Au$, $H_{100}Si_{149}Au$ and $H_{170}Si_{299}Au$: the Core Site

Species		**$H_{66}Si_{74}Au$**		**$H_{100}Si_{149}Au$**		**$H_{170}Si_{299}Au$**	
Spin state		Doublet	Quartet	Doublet	Quartet	Doublet	Quartet
	E_F	4.414	4.441	4.419	4.384	4.391	4.365

Table 5.26: Formation Energy in eV of $H_{66}Si_{74}Au$, $H_{100}Si_{149}Au$ and $H_{170}Si_{299}Au$: the Trough Site

Species		**$H_{66}Si_{74}Au$**		**$H_{100}Si_{149}Au$**		**$H_{170}Si_{299}Au$**	
Spin state		Doublet	Quartet	Doublet	Quartet	Doublet	Quartet
	E_F	4.152	4.805	4.573	4.640	4.482	4.590

Table 5.27: Formation Energy in eV of $H_{66}Si_{74}Au$, $H_{100}Si_{149}Au$ and $H_{170}Si_{299}Au$: the Crest Site

Species		**$H_{66}Si_{74}Au$**		**$H_{100}Si_{149}Au$**		**$H_{170}Si_{299}Au$**	
Spin state		Doublet	Quartet	Doublet	Quartet	Doublet	Quartet
	E_F	3.102	5.403	4.203	5.325	3.796	5.257

5.3.4 Density of States

From the formation energies it was determined that the crest site had the highest solubility of dopants. In Figures 5.5 – 5.13 we show the DOS plots for all dopants at the crest site for each size level. The DOS plots are decomposed into atomic orbital contributions of the noble metal atom dopant. The overall shapes of the DOS plots do not change upon doping, therefore we have increased the resolution of the DOS plots to better visualize the mid-gap states. Mid-gap states are the focus because they have significant roles in charge transport and photoconductivity.

For doping at the 75 Si atom size level, the relative positions of the mid-gap states are the same for Cu and Ag, each dopant introduces an occupied level in both spin channels. In the majority spin channel the mid-gap states are at the valence edge, in the minority spin channel the mid-gap state is about 2 eV above the valence edge. As for Au doping, two mid-gap states are introduced, one occupied state and one unoocupied state and this is true for both spin channels. The two mid-gap states deriving from the Au atom are within 1 eV of each other which account for the small energy E_G discussed in section 5.3.3. In the cases with Cu or Ag, the contribution to the HOMO from the dopant atomic orbitals comes from the p orbitals, but the Au atom has contributions from both p- and d-orbitals. In the LUMO we see that s orbitals comprise the contribution from all of the dopants. Even though the crest site is associated with an H atom both the HOMO and LUMO are free of H s-orbital contributions.

For doping at the 150 Si atom size level, we see a similar trend as before. The main difference comes from the Au atom doping. In this case the two mid-gap states are further apart than previously noted at the 75 Si atom size level. In the majority spin channel the separation of the mid-gap states is about 2 eV but in the minority spin channel the separation of midgap states is approximately 1 eV. The contributions to the

HOMO and LUMO are the same at this size level as they were in the 75 Si atom size level for Cu and Ag; they contribute portions of their p-orbitals to the HOMO. The Au atom doping has its d orbital contribution to the HOMO suppressed by H atom s orbital. This is the first instance of a dopant maintaining a bond with the passivant H atom.

For doping at the 300 Si atom size level the similarity between the mid-gap states of Cu and Ag doping is continued. The occupied state deriving from Cu or Ag doping is at the valence edge for the majority spin channel and in the minority spin channel the mid-gap state lays approximately 1.5 eV above the valence edge. For Au doping the mid-gap states are slightly different than any of the other cases. In both spin channels the occupied mid-gap state is at the valence edge and the unoccupied state is about 1.5 eV above the valence edge. At this size level the atomic contributions from dopant p-orbitals are the smallest ones seen in this study. Primarily it is Si atoms that make up the HOMO except in the case of Au doping, in which p- and d-orbital contributions are prevalent. In the LUMO we see H atom contribution in the cases of Cu and Ag doping but no participation of H atoms occurs for the case of Au doping.

The peculiarities associated with the doping scheme come from the ability of these atoms to behave as either a donor or acceptor. Au seems to be the most flexible because it has the most variation in its mid-gap states as well as in its orbital contributions.

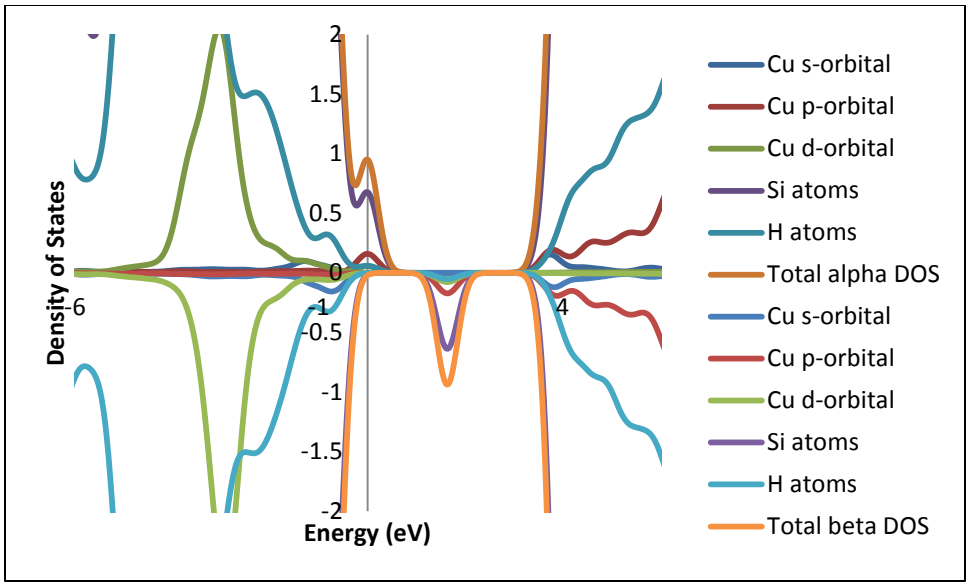

Figure 35: Density of States of $H_{66}Si_{74}Cu$ crest doping

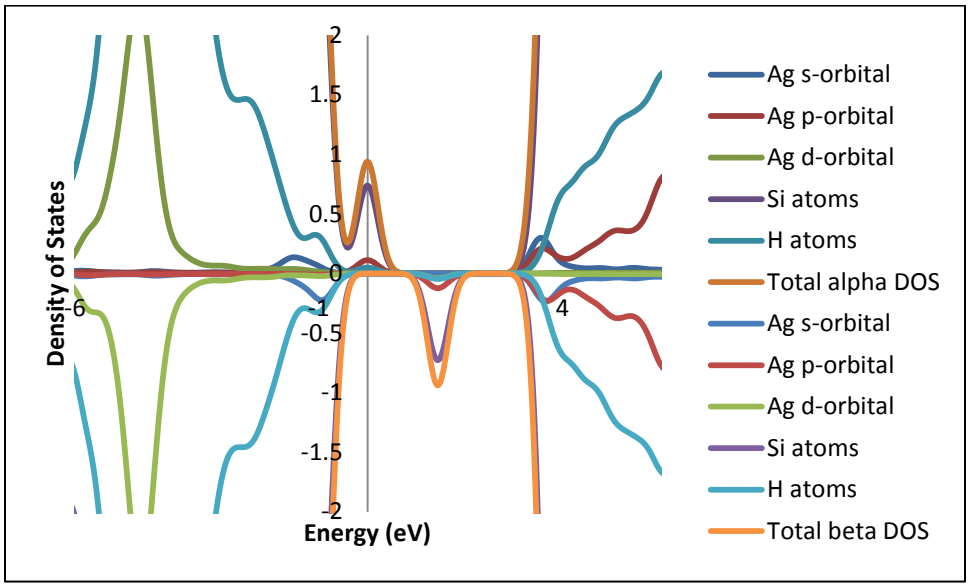

Figure 36: Density of States of $H_{66}Si_{74}Ag$ crest doping

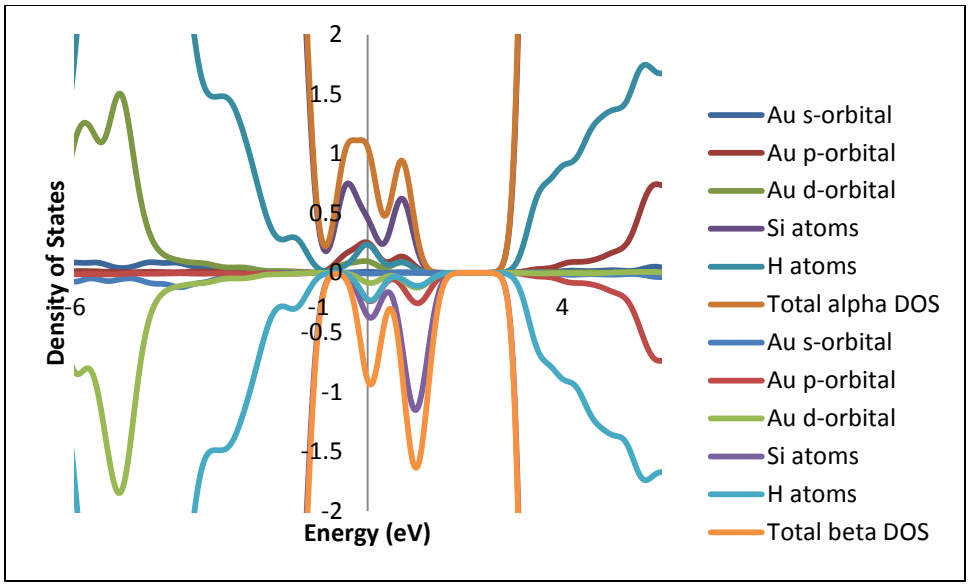

Figure 37: Density of States of $H_{66}Si_{74}Au$ crest doping

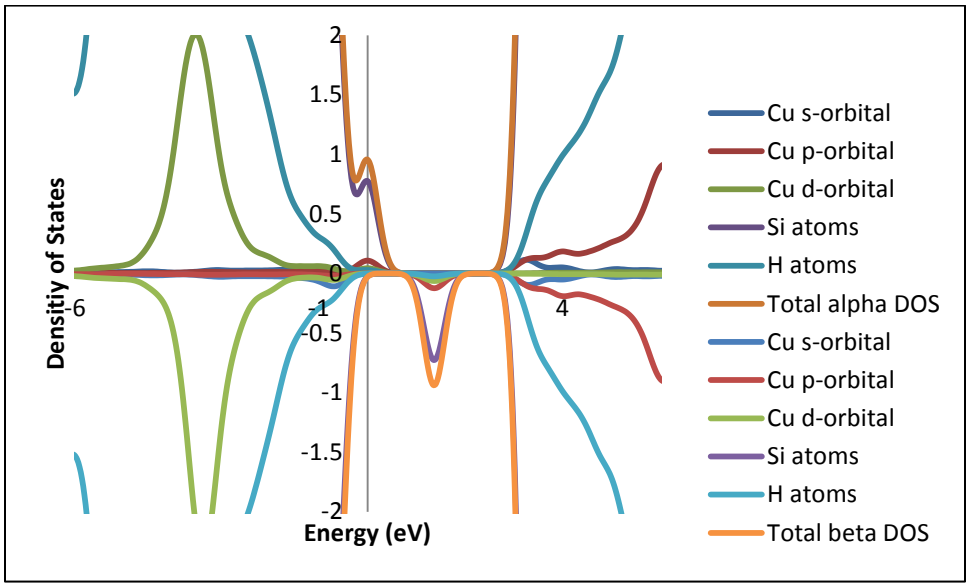

Figure 38: Density of States of $H_{100}Si_{149}Cu$ crest doping

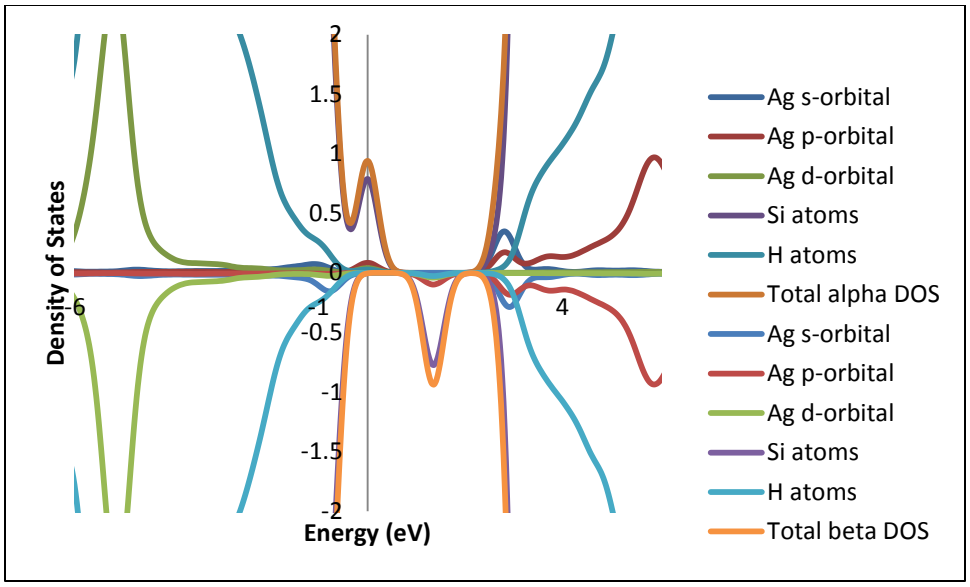

Figure 39: Density of States $H_{100}Si_{149}Ag$ crest doping

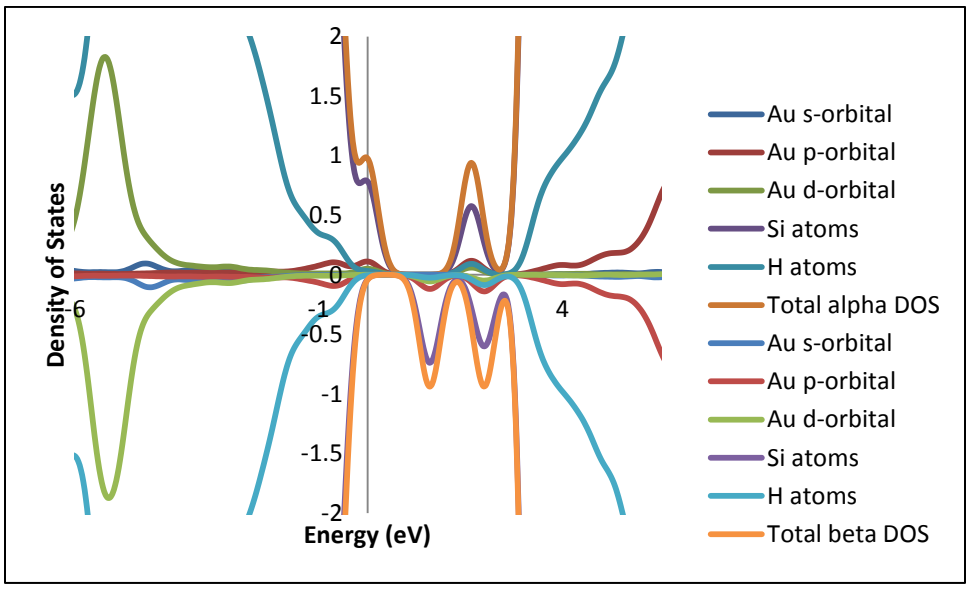

Figure 40: Density of States of $H_{100}Si_{149}Au$ crest doping

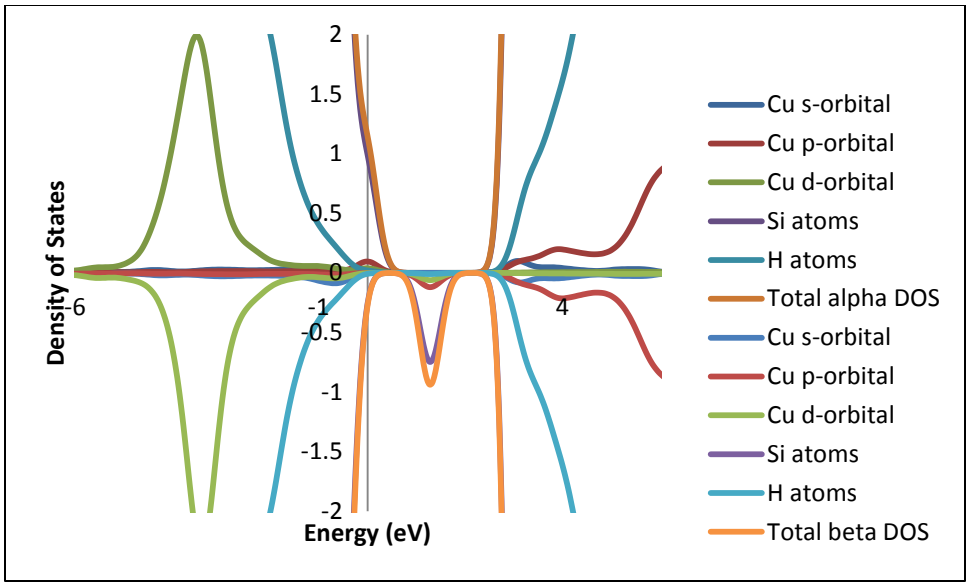

Figure 41: Density of States of $H_{170}Si_{299}Cu$ crest doping

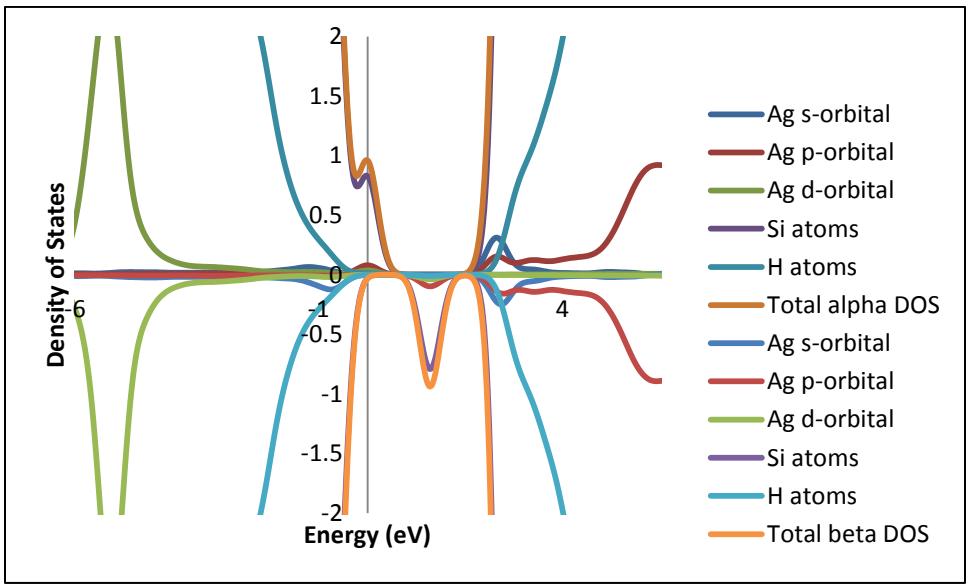

Figure 42: Density of States $H_{170}Si_{299}Ag$ crest doping

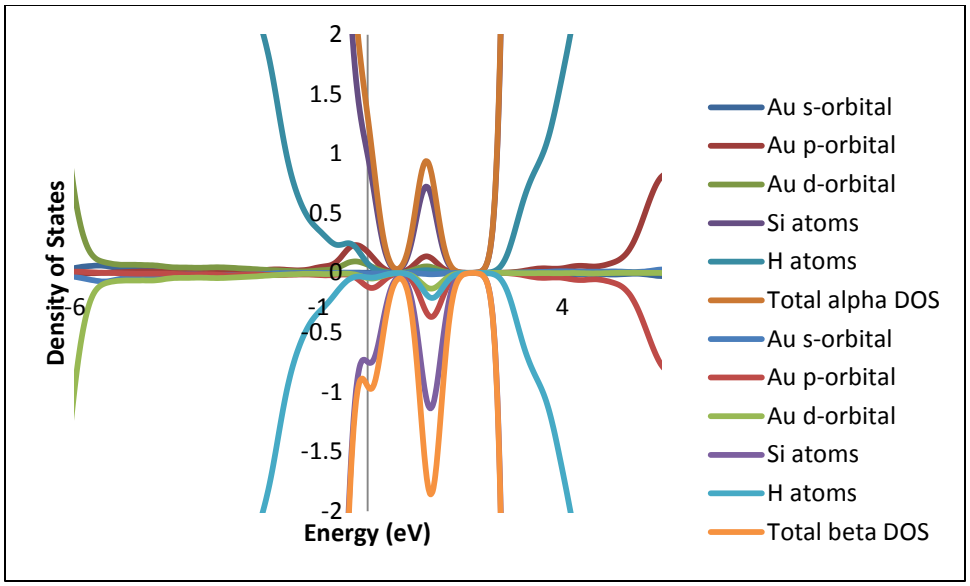

Figure 43: Density of States of $H_{170}Si_{299}Au$ crest doping

5.3.5 Mulliken Charge Distributions

In this section we discuss the Mulliken charge distributions to see how the ionic behaviors of dopants evolve in SiNCs and H-SiNCs. The Pauling scale electronegativity of Si, Cu, and Ag are all around 1.9 and for H and Au the electronegativity is 2.54 and 2.20, respectively. Based on these differences in electronegativity it interesting to see how charge distributes upon relaxation of the doped SiNCs and H-SiNCs. To elucidate the charging based on passivation and species of dopant we will compare the relative charging intensities of SiNCs and H-SiNCs for each of the dopants.

In Figure 5.14 we show a schematic of the Mulliken charge distributions of wurtzite SiNCs and H-SiNCs at the 150 Si atom size level. Again we focus on the crest site since we obtained maximum solubility of the dopants for all structures at this location. For Cu and Ag doping at the crest site passivation does not change the charge on the dopant atoms significantly. However for Au doping at the crest site passivation increases the intensity, shifting the negatively charged Au atom to even more negative. In addition Au doped H-SiNC contains relatively neutral Si atoms compared to the Si atoms in Cu and Ag doped H-SiNCs.

We can see that Cu and Ag give up charge to become more positive, however other Si atoms in the nanocrystals have similar charges as these dopant. This implies that Cu and Ag do not act like donors at this size level, but the Au dopant is clearly an acceptor in the hydrogen passivated SiNC.

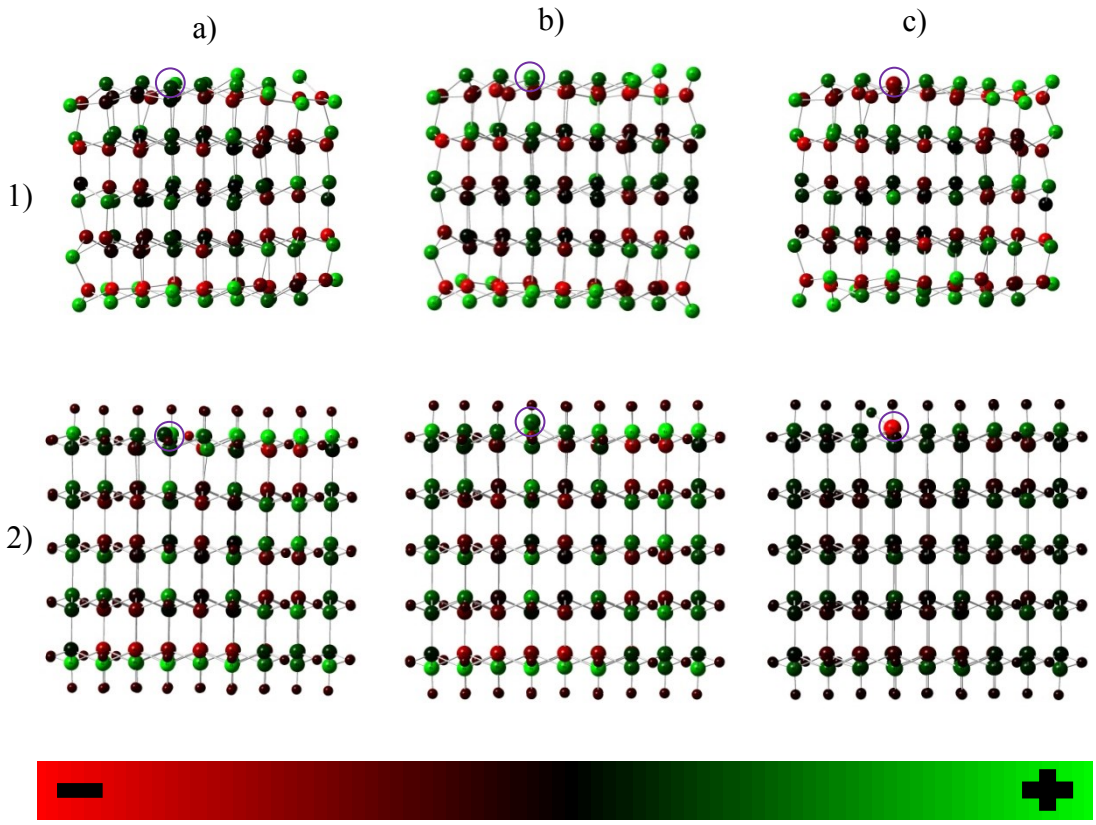

Figure 44: Mulliken Charge Distributions of a) Cu, b) Ag, and c) Au doping of Wurtzite Silicon Nanocrystals 1) Unpassivated and 2) Passivated at the 150 Si Atom Size Level

Chapter 6

Conclusion

6.1 Remarks

A comprehensive theoretical analysis toward a fundamental understanding of H passivation and novel metal atoms doping of silicon nanocrystals based on DFT calculations has been presented. The geometry, size, and dopant species makes the analysis of each system different. The mechanisms involved with H passivation as well as with doping can be utilized to engineer band structures for the customizable design of electronic devices.

Unpassivated silicon nanocrystals (SiNC)s at the 75, 150, and 300 Si atom size levels all preferred the wurtzite structure over the diamond structure based on the relative stability of these structures after geometry optimization. Less surface area of the nanostructures for wurtzite nanocrystals compared with the diamond nanocrysyals could be the reason for the higher stability for the wurtzites. However, the surface atoms have almost equal contribution to the electronic structure as the core atoms up to at least 8eV below the HOMO for both wurtzite and diamond structures.

Even though both structures demonstrated quantum confinement after H passivation by presenting the energetic signatures associated with the quantum confined model, they were at different intensities, and in this case resulted in a lowest energy geometry uncommon to the bulk phase of silicon. However, in general, size dependence of HOMO-LUMO gaps, binding energies and formation energies were all observed in this analysis.

For the diamond structure at the 150 Si atom size level strong distortions were prevalent in the core of the geometry even after passivation of its surfaces. More

precisely the difference in structural morphology, e.g. surface reconstruction, surface state density, and nanocrystal shape prevented a uniform passivation scheme across both geometries. In other words, even though both structures were passivated with the same passivant using the same procedure, the degree in which the core electronic states were isolated from the surface potential were different.

We concluded that the proximity of atoms with multiple dangling bonds, e.g. localized high surface state densities, are indeed culpable for any deficiencies in H passivation. sp^3 hybridization is to be expected in strong H-Si bonding and the singlet spin state was uniformly the ground spin state for all of the undoped passivated structures. The solubility of dopants in H-SiNCs is of extreme significance. Self-purification is a phenomenon associated with doping nanostructures that dictates an expulsion of impurities from the core. Although formatioin energies are high, dopants are unlikely to get into the nanocrystals, but in this study self-purification was indicated by the overall minimum formation energy of substitutional doping on the surfaces.

In general p-orbital of the dopant metal atom hybridize with the Si atoms. Sd-hybridize dopant metal orbital does show-up near the HOMO. However, for larger dopants, such as Au, sd-contribution is smaller. These behaviors are unique to the noble metal atoms because of their electronic configurations. The strong p-orbital presence and sd hybridization is good for the catalytic properties seen in experiment. Many of the growth characteristics of silicon nanostructures can be explained by the behaviors seen in this thesis. The dissociation of Cu from its surface explains why Cu catalyzed structures are scarce. Additionally, the induced covalent behavior from the Au dopant can explain why Au catalyzed structures are so prevalent.

6.2 Research Outlook

This study of SiNCs and H-SiNCs was a preliminary task for understanding electronic structure of semiconductors, in general. Our future plans are to use this knowledge in the analysis of binary and ternary metal oxide semiconductors nanocrystals, such as Fe_2O_3 and $Bi_2Ti_2O_7$. These materials have demonstrated significant potentials pertaining to solar energy conversion and will indeed require electronic structure design in order to improve upon their quantum efficiencies. Also we will be considering other quantum chemical computing software for the description of these materials. Therefore we will be employing suitable correction methods to our approximations for the more accurate description of electronic structure. The objective for my research endeavors will be the sustainability of renewable energy sources.

Appendix A

Cartesian Relaxed Coordinates of Passivated Diamond and Wurtzite Nanocrystals at the 300 Si atom size level

Relaxed Coordinates of the Passivated Diamond Silicon Nanocrystal at the 300 Si Atom Size Level

Atom	x	y	z
Si	1.128553	-10.596	-6.5839
Si	1.969406	-10.1993	-0.92671
Si	2.673488	-9.75967	4.523568
Si	3.740291	-8.55815	-3.96689
Si	5.55178	-6.96987	-7.00206
Si	4.461611	-8.01927	1.605446
Si	6.19412	-6.41464	-1.42615
Si	5.23222	-7.59438	7.134654
Si	6.897643	-5.84974	4.1857
Si	8.033453	-4.79718	-4.40369
Si	10.01844	-3.23332	-7.28027
Si	8.617754	-4.2603	1.139575
Si	10.45246	-2.60964	-1.81374
Si	9.227874	-3.63857	6.894423
Si	10.96609	-2.11862	3.798945
Si	12.47858	-1.21147	-4.58951
Si	13.05418	-0.74278	1.134785
Si	-2.47404	-8.47629	-7.24161
Si	-0.30391	-10.249	-4.73371
Si	-4.11185	-10.0936	-4.07806
Si	0.0128	-8.2558	-3.44616
Si	-3.86711	-8.0256	-2.97124
Si	-2.44912	-10.2701	-5.71814
Si	-2.14053	-6.44336	-6.08406
Si	-1.76787	-8.02656	-1.8541
Si	0.395331	-9.82838	0.78428
Si	-3.30344	-9.72201	1.433536
Si	0.648863	-7.81012	2.021924
Si	-3.2239	-7.58627	2.450709
Si	-1.70351	-9.81779	-0.29281
Si	-1.50305	-5.97965	-0.65278
Si	-1.14027	-7.59746	3.595972
Si	1.002755	-9.48816	6.142065
Si	-2.64882	-9.37824	6.885061

Si	1.303705	-7.52206	7.432047
Si	-2.52232	-7.24093	7.902292
Si	-1.10121	-9.44057	5.102821
Si	-0.87282	-5.56847	4.814812
Si	-0.4513	-7.56588	9.016033
Si	1.707774	-8.64154	-7.76722
Si	1.994033	-4.81538	-7.98129
Si	3.890288	-6.63697	-5.33632
Si	-0.02697	-6.4228	-4.95924
Si	4.18197	-4.60223	-4.09921
Si	0.254684	-4.38549	-3.737
Si	1.798451	-6.63825	-6.49391
Si	2.084881	-2.77826	-6.79191
Si	2.103446	-8.26823	-2.28494
Si	2.350596	-4.38015	-2.56861
Si	4.456005	-6.176	0.144954
Si	0.584508	-5.97541	0.507939
Si	4.717659	-4.14239	1.383033
Si	0.837902	-3.93167	1.728492
Si	2.380685	-6.22024	-1.04868
Si	2.600979	-2.32566	-1.34656
Si	2.726239	-7.82189	3.181192
Si	2.913391	-3.93738	2.922774
Si	5.038431	-5.77355	5.630229
Si	1.203703	-5.60086	5.994149
Si	5.248643	-3.74376	6.857169
Si	1.402938	-3.53217	7.182942
Si	2.982053	-5.8007	4.427445
Si	3.142795	-1.88174	4.133077
Si	3.361947	-7.95479	8.516359
Si	3.43604	-3.71716	8.360885
Si	6.187991	-5.07454	-8.2598
Si	6.341536	-1.19499	-8.62528
Si	8.125605	-2.95804	-5.87658
Si	4.191204	-2.77468	-5.63354
Si	8.36213	-0.92668	-4.67851
Si	4.4172	-0.72268	-4.42152
Si	6.084046	-3.00072	-7.11171

Si	6.259759	0.870153	-7.46488
Si	6.245772	-4.56628	-2.88255
Si	6.490891	-0.70677	-3.19841
Si	8.562432	-2.49998	-0.42045
Si	4.679215	-2.30425	-0.13797
Si	8.841537	-0.46353	0.804124
Si	4.927609	-0.25195	1.074125
Si	6.5045	-2.52622	-1.65609
Si	6.686729	1.34737	-2.00667
Si	6.779255	-4.10947	2.602383
Si	7.004096	-0.23894	2.317286
Si	9.038833	-2.05117	5.146011
Si	5.194809	-1.87003	5.360915
Si	9.21588	0.00889	6.303917
Si	5.382162	0.208539	6.526534
Si	7.019604	-2.08144	3.850612
Si	7.207158	1.832284	3.498071
Si	7.244523	-3.97806	8.11223
Si	7.384772	0.200551	7.757981
Si	10.68394	-1.37422	-8.56884
Si	8.300791	0.874274	-6.22711
Si	8.359514	2.965365	-5.14143
Si	10.16931	0.749994	-7.68281
Si	10.41673	-0.91644	-3.45352
Si	8.749697	1.343761	-0.77257
Si	8.985456	3.330172	0.469672
Si	10.60712	1.069975	-2.1977
Si	10.90104	-0.46298	2.097806
Si	9.234315	1.836537	4.789164
Si	9.573466	3.687382	6.229128
Si	11.15748	1.452431	3.479145
Si	11.20771	-0.00603	7.599839
Si	-6.84836	-8.17523	-6.81455
Si	-6.23187	-4.4132	-7.16619
Si	-3.95029	-6.23946	-4.53952
Si	-7.87987	-5.84036	-4.22
Si	-3.67516	-4.17842	-3.34317
Si	-7.56138	-3.90578	-2.92856

Si	-6.06428	-6.24281	-5.67888
Si	-5.81958	-2.3774	-6.03896
Si	-5.59338	-7.76686	-1.38656
Si	-5.46323	-3.92283	-1.77883
Si	-3.29015	-5.75819	0.919322
Si	-7.13492	-5.47319	1.332849
Si	-3.04254	-3.71345	2.13284
Si	-6.916	-3.45244	2.534832
Si	-5.37916	-5.72681	-0.22649
Si	-5.2121	-1.87787	-0.57749
Si	-4.88046	-7.40029	4.123006
Si	-4.82903	-3.48563	3.70544
Si	-2.64178	-5.36709	6.391801
Si	-6.36394	-5.18354	6.965919
Si	-2.44263	-3.29542	7.579604
Si	-6.27149	-3.04414	7.977932
Si	-4.74163	-5.32782	5.244714
Si	-4.58695	-1.42391	4.889252
Si	-4.22478	-3.26408	9.136198
Si	-2.12896	-4.62334	-7.57812
Si	-1.86005	-0.79409	-7.92246
Si	0.236705	-2.56466	-5.26928
Si	-3.71494	-2.36605	-4.88362
Si	0.470759	-0.51677	-4.06416
Si	-3.47173	-0.31711	-3.68494
Si	-1.87651	-2.5918	-6.40493
Si	-1.67475	1.246622	-6.76184
Si	-1.56372	-4.15945	-2.18968
Si	-1.36175	-0.29093	-2.52393
Si	0.784293	-2.09647	0.196418
Si	-3.11222	-1.88084	0.587518
Si	1.024525	-0.03669	1.39979
Si	-2.86878	0.179446	1.78129
Si	-1.31211	-2.10976	-0.97666
Si	-1.12242	1.767177	-1.327
Si	-0.95191	-3.71601	3.295126
Si	-0.77983	0.192557	2.956396
Si	1.34252	-1.6641	5.675546

Si	-2.51096	-1.43332	6.059087
Si	1.547721	0.420323	6.834573
Si	-2.28549	0.654125	7.213648
Si	-0.7265	-1.65552	4.490437
Si	-0.54205	2.27403	4.131554
Si	-0.38598	-3.44898	8.715879
Si	-0.23209	0.649745	8.357221
Si	2.227585	-0.97586	-8.30688
Si	2.328825	2.870619	-8.68022
Si	4.371211	1.090982	-5.98587
Si	0.42596	1.290249	-5.62157
Si	4.538761	3.158381	-4.80852
Si	0.612206	3.357215	-4.45006
Si	2.269307	1.074314	-7.14361
Si	2.321168	4.941748	-7.54537
Si	2.569825	-0.50222	-2.89466
Si	2.706872	3.37716	-3.28035
Si	4.859856	1.566566	-0.49022
Si	0.970563	1.788108	-0.15432
Si	5.080053	3.635406	0.676082
Si	1.20438	3.865392	1.016665
Si	2.782168	1.562196	-1.70276
Si	2.912523	5.45511	-2.12505
Si	3.10393	-0.03292	2.600939
Si	3.280611	3.869958	2.217477
Si	5.380451	2.054823	5.004902
Si	1.526546	2.273681	5.316295
Si	5.614828	4.142147	6.150225
Si	1.765188	4.358408	6.468424
Si	3.327348	2.045281	3.775759
Si	3.535909	5.949524	3.37508
Si	3.577342	0.425924	8.016396
Si	3.815708	4.550334	7.615749
Si	6.515869	2.681121	-8.97933
Si	4.415776	4.95807	-6.39588
Si	4.44953	7.099193	-5.39537
Si	6.049332	4.831462	-8.11738
Si	6.59955	3.152243	-3.58409

Si	4.986866	5.432351	-0.91667
Si	5.20261	7.479455	0.219447
Si	6.740614	5.220142	-2.47215
Si	7.141386	3.626064	1.906441
Si	5.592521	5.946147	4.59277
Si	5.988578	7.918571	5.855535
Si	7.438628	5.594312	3.171864
Si	7.631536	4.353789	7.379371
Si	-10.7048	-3.97282	-6.86693
Si	-9.9872	-0.30724	-7.2089
Si	-7.66449	-2.13604	-4.52355
Si	-11.6489	-1.60947	-4.29595
Si	-7.40371	-0.08456	-3.32079
Si	-11.3086	0.321816	-2.98439
Si	-9.79869	-2.1191	-5.69004
Si	-9.45732	1.7106	-6.10274
Si	-9.39591	-3.56916	-1.48623
Si	-9.20647	0.207561	-1.76791
Si	-7.0118	-1.63644	0.979653
Si	-10.9264	-1.29891	1.265479
Si	-6.76557	0.40421	2.195117
Si	-10.6382	0.649561	2.577903
Si	-9.10615	-1.61048	-0.20366
Si	-8.87373	2.226459	-0.54447
Si	-8.64377	-3.2243	4.132139
Si	-8.56056	0.636344	3.775943
Si	-6.35952	-1.19562	6.461908
Si	-10.1236	-1.00409	6.981651
Si	-6.12655	0.873666	7.640036
Si	-9.95011	1.072511	8.082649
Si	-8.45296	-1.1883	5.316105
Si	-8.27215	2.682231	4.969225
Si	-7.88406	1.100508	9.205406
Si	-5.93741	-0.56873	-7.5423
Si	-5.89053	3.276117	-7.9188
Si	-3.50844	1.483044	-5.24399
Si	-7.40761	1.704892	-4.87618
Si	-3.28997	3.526544	-4.04036

Si	-7.17238	3.758891	-3.68333
Si	-5.59727	1.473107	-6.41458
Si	-5.47013	5.288101	-6.76778
Si	-5.29085	-0.07862	-2.14013
Si	-5.09097	3.774469	-2.49514
Si	-2.92493	2.000963	0.230541
Si	-6.80315	2.214839	0.64152
Si	-2.67267	4.070699	1.422113
Si	-6.53898	4.25759	1.846386
Si	-5.0263	1.971452	-0.93574
Si	-4.83438	5.81293	-1.28505
Si	-4.65989	0.411362	3.350142
Si	-4.45162	4.311874	3.001053
Si	-2.3262	2.511937	5.699819
Si	-6.178	2.70968	6.107937
Si	-2.07882	4.609038	6.85489
Si	-5.91269	4.791013	7.254658
Si	-4.40361	2.481072	4.534935
Si	-4.18573	6.391804	4.171876
Si	-4.05345	0.88284	8.754035
Si	-3.84565	5.033954	8.371406
Si	-1.7931	3.027628	-8.29039
Si	-1.91638	6.830806	-8.72554
Si	0.491627	5.156237	-6.03197
Si	-3.39307	5.309773	-5.59771
Si	0.680865	7.239188	-4.88734
Si	-3.19184	7.374272	-4.42795
Si	-1.61236	5.085961	-7.16647
Si	-1.6883	8.867622	-7.59189
Si	-1.19044	3.57459	-2.88899
Si	-1.08737	7.453469	-3.29829
Si	1.125741	5.681074	-0.55847
Si	-2.74179	5.87399	-0.14255
Si	1.382909	7.756814	0.603719
Si	-2.48432	7.941651	1.024771
Si	-0.96741	5.649452	-1.72266
Si	-0.81714	9.512711	-2.1274
Si	-0.58092	4.105162	2.583453

Si	-0.39326	8.00571	2.173212
Si	1.758801	6.196466	4.937537
Si	-2.08399	6.446187	5.312063
Si	2.052988	8.288962	6.070704
Si	-1.77486	8.54902	6.449674
Si	-0.31476	6.194833	3.744995
Si	-0.09205	10.08625	3.321829
Si	-0.01021	4.740545	7.970926
Si	0.300599	8.82422	7.564251
Si	2.32399	6.707634	-9.13814
Si	0.416251	8.999017	-6.50498
Si	0.361833	11.18582	-5.59882
Si	1.92684	8.891637	-8.32467
Si	2.784334	7.261975	-3.7207
Si	1.268494	9.558815	-0.97437
Si	1.399666	11.71954	0.004946
Si	2.890406	9.383215	-2.68176
Si	3.46327	7.732284	1.780237
Si	1.975447	9.999902	4.448299
Si	3.721361	9.783709	2.903474
Si	4.145839	8.708728	7.093336
Si	-11.3622	1.925197	-4.73953
Si	-13.4198	0.705769	-1.96725
Si	-10.7262	2.324391	0.907814
Si	-12.6506	0.964645	3.787447
Si	-9.9814	2.898238	6.592591
Si	-7.35705	5.418874	-5.3612
Si	-8.96934	3.935825	-2.16419
Si	-6.54903	6.055856	0.321577
Si	-8.28752	4.472099	3.426705
Si	-5.81292	6.706654	5.864857
Si	-3.45649	9.053734	-6.06541
Si	-4.92051	7.576995	-2.83906
Si	-2.43232	9.808511	-0.42663
Si	-4.10807	8.249269	2.713457
Si	-1.63897	10.47935	5.069076
Si	-0.88918	11.37253	-3.60259
Si	0.171251	12.03192	1.997037

H	3.498674	-7.18852	9.779472
H	3.32664	-9.39879	8.881035
H	-0.20379	-6.66824	10.16817
H	-0.49833	-8.95436	9.552585
H	7.211784	-3.05972	9.276595
H	7.256031	-5.35872	8.659955
H	3.5856	-2.69566	9.42315
H	3.409614	-5.03285	9.047093
H	-0.19761	-2.3858	9.727884
H	-0.40059	-4.72512	9.462486
H	-4.01283	-2.25888	10.20337
H	-4.251	-4.59981	9.791905
H	-7.71225	2.377114	9.948993
H	-7.81266	-0.01415	10.18754
H	-3.89284	2.143978	9.512868
H	-4.00463	-0.21419	9.747433
H	-0.07172	1.897369	9.133003
H	-0.20156	-0.45105	9.34326
H	3.711792	1.674415	8.799046
H	3.593221	-0.68397	8.995467
H	7.484546	1.429367	8.579792
H	7.368303	-0.94036	8.704457
H	11.9997	1.228316	7.379017
H	10.85669	-0.08561	9.041687
H	12.05685	-1.17307	7.25842
H	7.77718	5.778244	7.770988
H	7.517562	3.580985	8.639726
H	3.923355	5.960305	8.065018
H	3.873701	3.719047	8.840134
H	0.127267	6.122775	8.476353
H	0.064719	3.86161	9.158947
H	-3.74212	6.465803	8.764198
H	-3.71757	4.232051	9.61032
H	0.423182	10.28342	7.835178
H	0.414416	8.134897	8.87045
H	4.250181	10.19212	7.182991
H	4.204148	8.184086	8.48023
H	10.24744	-3.0914	7.830335

H	9.752985	-4.9354	6.400432
H	6.434448	-7.38191	7.98049
H	5.483793	-8.82011	6.336245
H	12.11502	-1.72881	4.661965
H	11.26878	-3.47566	3.286417
H	8.115233	-5.62124	5.001673
H	7.065909	-7.1764	3.548784
H	3.999305	-10.0411	5.125712
H	2.329029	-10.9078	3.643195
H	14.00599	-0.38479	2.220358
H	13.2972	-2.15796	0.76223
H	13.32967	0.12552	-0.03235
H	9.863331	-4.14795	1.92918
H	8.668107	-5.57991	0.471984
H	5.770684	-8.16056	2.28215
H	4.263652	-9.25637	0.815976
H	11.6381	-2.34509	-0.95896
H	10.64953	-3.9529	-2.4066
H	7.496509	-6.62596	-0.75654
H	5.942086	-7.63037	-2.22959
H	3.290807	-10.6605	-0.43992
H	1.416588	-11.2823	-1.78504
H	13.50386	-0.43303	-3.84682
H	12.86677	-2.6437	-4.55881
H	9.308578	-4.98004	-3.67276
H	7.826562	-6.02852	-5.2034
H	5.039869	-9.02749	-3.43237
H	3.239187	-9.64602	-4.84442
H	11.14293	-3.60041	-6.37847
H	9.80524	-4.39114	-8.18681
H	6.757534	-7.56347	-6.37294
H	5.034033	-7.98227	-7.95765
H	2.359149	-11.3225	-6.18479
H	0.380781	-11.484	-7.51798
H	12.15802	-1.45396	-8.75963
H	10.06144	-1.48319	-9.91257
H	7.606514	-5.2632	-8.66539
H	5.391476	-5.01838	-9.51071

H	3.040264	-8.85174	-8.38783
H	0.748869	-8.44229	-8.88283
H	7.731011	-1.30628	-9.14665
H	5.451075	-1.26272	-9.80788
H	3.297149	-4.97392	-8.67229
H	0.962889	-4.7959	-9.04448
H	-1.39769	-8.67813	-8.24146
H	-3.74759	-8.39189	-7.99481
H	7.937011	2.677914	-9.41587
H	5.697762	2.450958	-10.1961
H	3.530748	-1.10524	-8.99385
H	1.200695	-1.01888	-9.37238
H	-1.01557	-4.79603	-8.53678
H	-3.36789	-4.58208	-8.38578
H	-5.81865	-8.957	-7.53362
H	-7.535	-9.06645	-5.8459
H	-7.85528	-7.70046	-7.79974
H	-5.39955	-4.57433	-8.38028
H	-7.64122	-4.36523	-7.6243
H	-0.70318	-0.94515	-8.82881
H	-3.05853	-0.80087	-8.78782
H	3.619939	2.781672	-9.40468
H	1.269946	2.755248	-9.70927
H	3.630717	6.708938	-9.84487
H	1.290076	6.391588	-10.1561
H	-0.72521	2.918806	-9.30904
H	-3.07436	2.957592	-9.02653
H	-5.00872	-0.73569	-8.68137
H	-7.29329	-0.54298	-8.1268
H	-9.78604	-4.63864	-7.81795
H	-11.2537	-4.98142	-5.92731
H	-11.842	-3.4014	-7.6375
H	-9.2826	-0.5184	-8.49403
H	-11.4389	-0.22229	-7.52887
H	-5.11571	3.118346	-9.17036
H	-7.32827	3.284587	-8.29815
H	-0.95962	6.721847	-9.85355
H	-3.28789	6.701744	-9.28539

H	-1.72192	10.002	-8.55809
H	-5.48684	6.425071	-7.72854
H	-9.42851	2.822456	-7.08952
H	-11.645	3.306065	-4.28608
H	-12.5218	1.513433	-5.57885
H	-7.61761	6.771758	-4.81901
H	-8.53753	5.05012	-6.18818
H	-3.51751	10.40523	-5.458
H	-4.75234	8.81476	-6.75466
H	-0.41634	12.5738	-2.86751
H	-2.30958	11.62183	-3.95483
H	-4.81346	8.884002	-2.15359
H	-6.23391	7.575107	-3.52021
H	-9.05011	5.290167	-1.57631
H	-10.2286	3.746432	-2.91053
H	-13.6163	2.144576	-1.66266
H	-14.4131	0.32016	-3.00561
H	-13.6837	-0.09443	-0.7499
H	-12.9019	2.411745	4.000281
H	-13.7517	0.417454	2.952656
H	-12.6684	0.2772	5.099458
H	-10.9619	3.678089	1.460972
H	-11.9238	1.994571	0.095043
H	-12.1269	-1.05837	0.428097
H	-11.2078	-2.50715	2.074515
H	0.926255	12.99073	2.851827
H	-1.13389	12.66618	1.684698
H	-3.6352	9.382364	3.535086
H	-5.43009	8.659009	2.188669
H	-8.13777	5.751781	4.154846
H	-9.5926	4.542727	2.732937
H	-9.75541	4.150058	7.3641
H	-11.3039	3.017475	5.927346
H	-11.0635	1.214207	9.06329
H	-11.4743	-1.2033	6.400251
H	-9.90163	-2.08595	7.978625
H	-9.9687	-3.32265	3.4805
H	-8.57111	-4.35008	5.089857

H	-8.42898	-5.49593	0.621389
H	-7.16773	-6.62335	2.259871
H	-6.90983	-7.84946	-2.05717
H	-5.54985	-8.89103	-0.42492
H	-5.4723	-10.2027	-4.66482
H	-3.95729	-11.197	-3.09324
H	-7.71445	-5.59181	6.515293
H	-5.9497	-6.15162	8.018006
H	-6.23798	-7.69418	3.61373
H	-4.59533	-8.44643	5.125964
H	-4.66712	-10.1161	1.010393
H	-2.87211	-10.7029	2.464894
H	-3.60388	-7.11175	8.917021
H	-4.01071	-9.83501	6.526317
H	-2.13007	-10.3335	7.903341
H	-1.27535	-10.696	4.323038
H	0.414419	-10.9725	1.738463
H	-0.19101	-11.425	-3.82709
H	-2.5923	-11.5529	-6.46337
H	-10.5754	-3.35742	-2.34964
H	-9.70451	-4.75704	-0.65997
H	-1.01653	11.53085	5.921532
H	-2.93851	11.02265	4.609676
H	-2.88205	8.730451	7.428874
H	1.304575	9.672797	-9.43052
H	3.217022	9.549616	-8.00069
H	-0.29928	12.04128	-6.62409
H	1.726171	11.73121	-5.39079
H	0.893458	12.68733	-1.00252
H	2.822975	12.06475	0.244461
H	2.529879	10.38261	-3.7187
H	4.258029	9.727458	-2.22802
H	4.075181	8.063798	-6.46053
H	5.784682	7.516933	-4.90771
H	5.55846	5.663458	-9.24647
H	7.312908	5.454562	-7.65059
H	9.970007	1.692109	-8.81434
H	11.33828	1.249239	-6.91297

H	8.175427	4.015432	-6.17282
H	9.66704	3.234008	-4.49991
H	6.630617	6.306565	-3.47068
H	8.054207	5.393464	-1.8135
H	5.157778	8.594868	-0.75269
H	6.519543	7.565203	0.888786
H	3.694026	10.89278	1.92054
H	5.043201	9.835071	3.569425
H	2.120276	11.29085	5.180327
H	-5.31729	7.812226	6.729852
H	-7.12081	7.138757	5.320341
H	-7.0294	4.947426	8.229432
H	-6.32758	7.314614	1.06054
H	-7.86885	6.200416	-0.32704
H	-1.97992	10.95956	0.393357
H	-3.77143	10.17226	-0.94489
H	-12.7422	-1.25365	-5.24318
H	-12.1366	-2.7782	-3.52606
H	6.471902	8.986671	4.947187
H	7.10065	7.632252	6.796412
H	10.17219	4.842939	5.517798
H	10.56896	3.246547	7.242542
H	11.61605	2.65767	2.747657
H	12.24762	1.092192	4.42818
H	9.184644	4.507091	-0.40582
H	10.20697	3.214291	1.296995
H	7.733457	6.771469	2.322958
H	8.632392	5.386835	4.025995
H	10.81505	2.257525	-3.05817
H	11.8137	0.942049	-1.3449
H	-9.04242	-5.57603	-5.10509
H	-8.23224	-7.03384	-3.41669
H	-7.38567	-2.91533	8.959134
H	-1.84638	-11.0998	-1.03969
H	1.03243	-10.628	7.102631
H	12.47558	-0.75198	-5.99615

Appendix B

Density of States

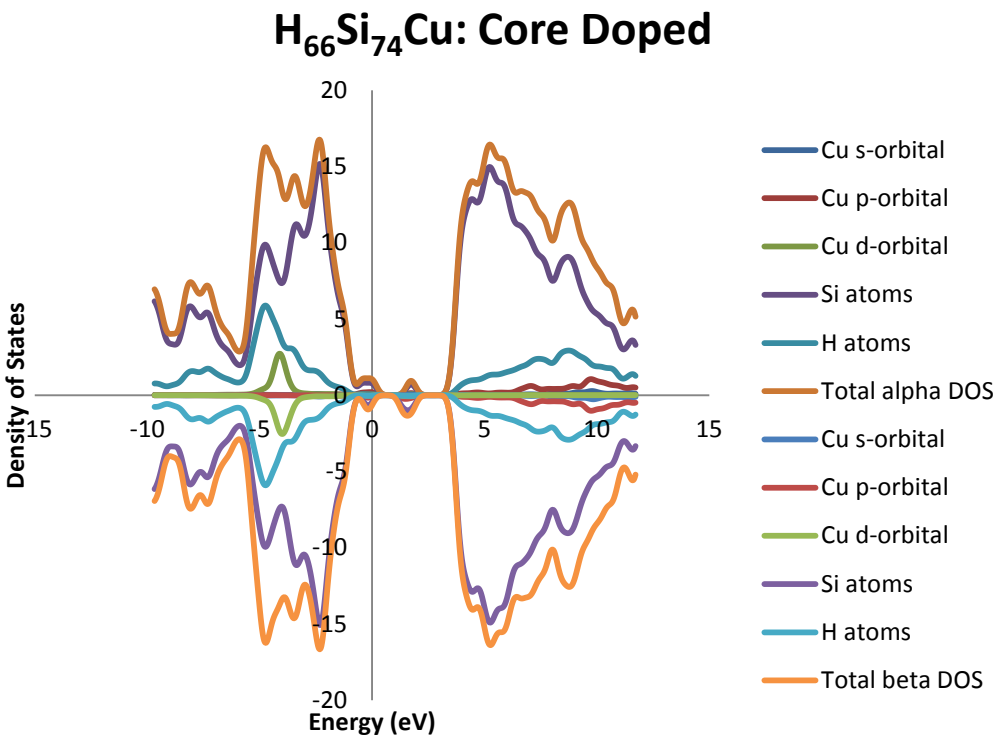
H66Si74Cu: Core Doped
Density of States
Energy (eV)
20
15
10
5
0
-5
-10
-15
-20
-15
-10
-5
0
5
10
15
Cu s-orbital
Cu p-orbital
Cu d-orbital
Si atoms
H atoms
Total alpha DOS
Cu s-orbital
Cu p-orbital
Cu d-orbital
Si atoms
H atoms
Total beta DOS

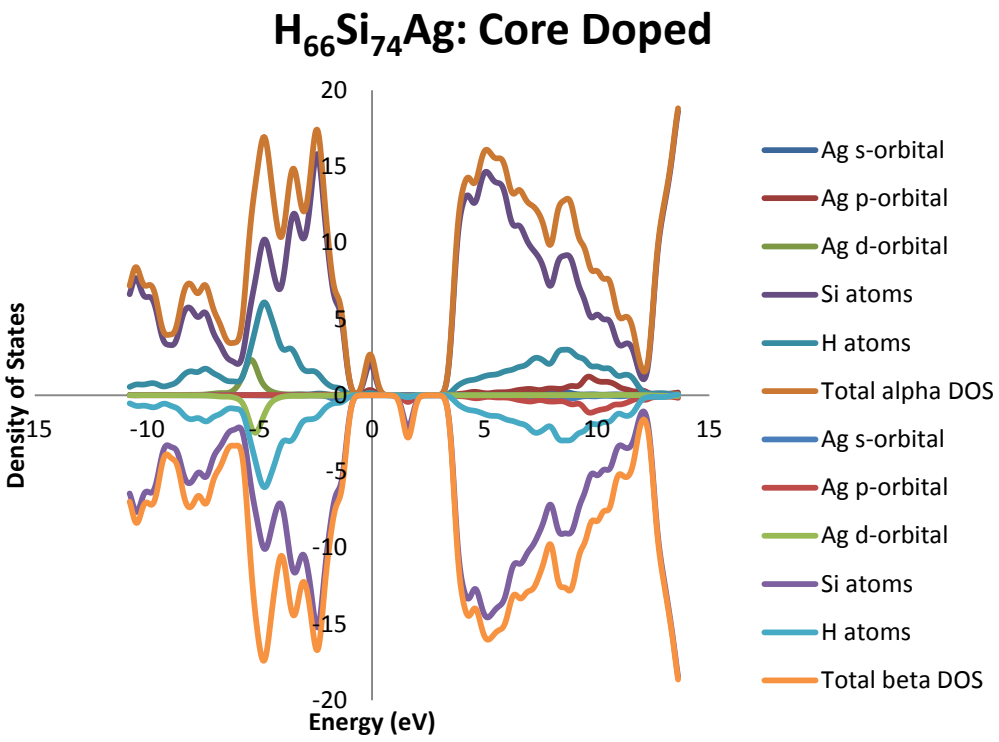
H66Si74Ag: Core Doped
Density of States
Energy (eV)
20
15
10
5
0
-5
-10
-15
-20
-15
-10
-5
0
5
10
15
Ag s-orbital
Ag p-orbital
Ag d-orbital
Si atoms
H atoms
Total alpha DOS
Ag s-orbital
Ag p-orbital
Ag d-orbital
Si atoms
H atoms
Total beta DOS

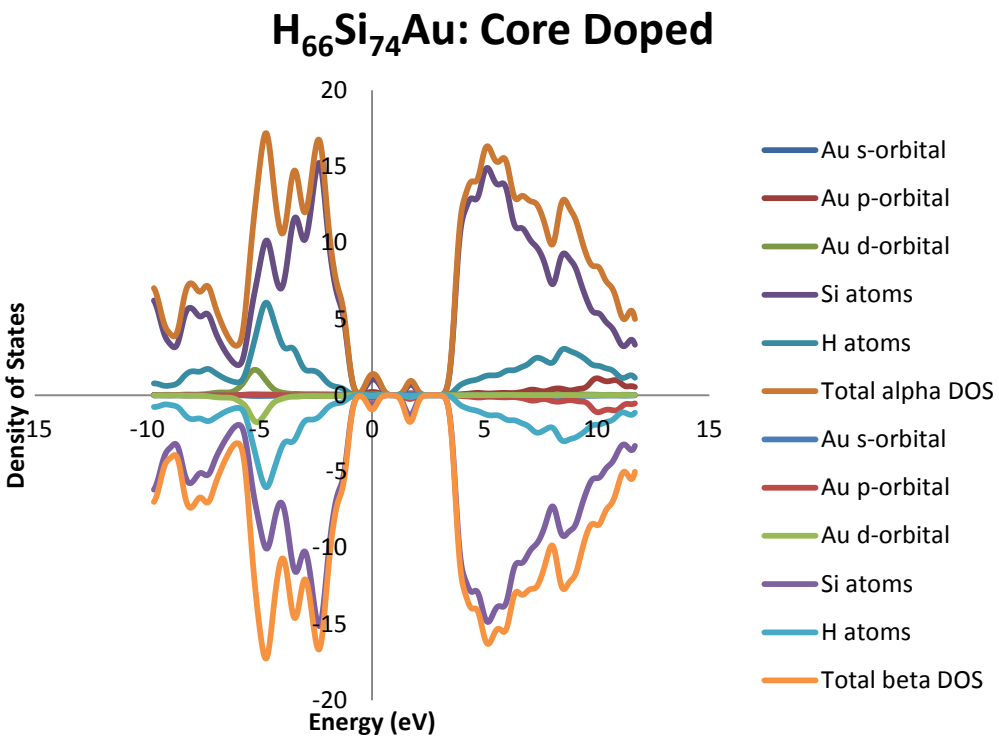
H66Si74Au: Core Doped
Density of States
Energy (eV)
20
15
10
5
0
-5
-10
-15
-20
-15
-10
-5
0
5
10
15
Au s-orbital
Au p-orbital
Au d-orbital
Si atoms
H atoms
Total alpha DOS
Au s-orbital
Au p-orbital
Au d-orbital
Si atoms
H atoms
Total beta DOS

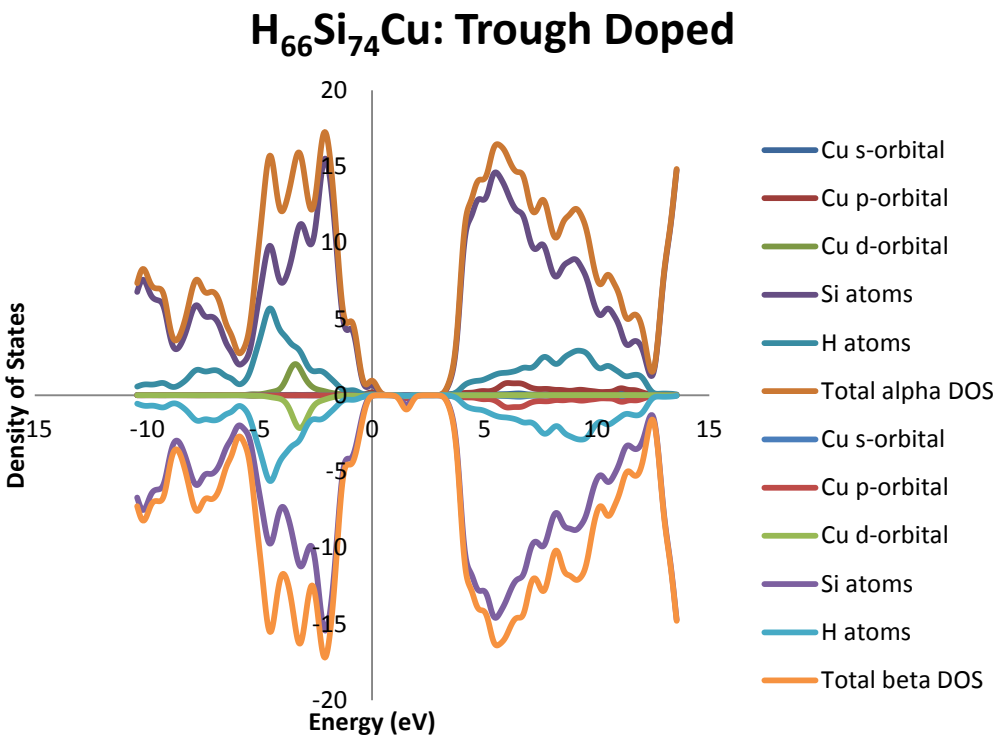
H66Si74Cu: Trough Doped
Density of States
Energy (eV)
20
15
10
5
0
-5
-10
-15
-20
-15
-10
-5
0
5
10
15
Cu s-orbital
Cu p-orbital
Cu d-orbital
Si atoms
H atoms
Total alpha DOS
Cu s-orbital
Cu p-orbital
Cu d-orbital
Si atoms
H atoms
Total beta DOS

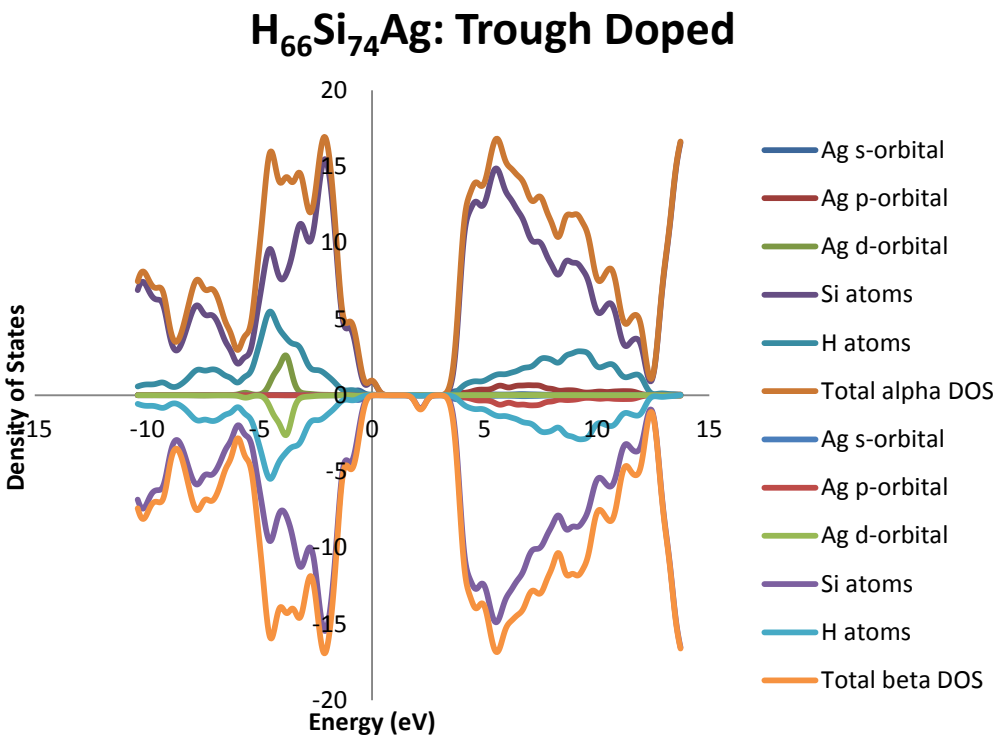
H66Si74Ag: Trough Doped
Density of States
Energy (eV)
20
15
10
5
0
-5
-10
-15
-20
-15
-10
-5
0
5
10
15
Ag s-orbital
Ag p-orbital
Ag d-orbital
Si atoms
H atoms
Total alpha DOS
Ag s-orbital
Ag p-orbital
Ag d-orbital
Si atoms
H atoms
Total beta DOS

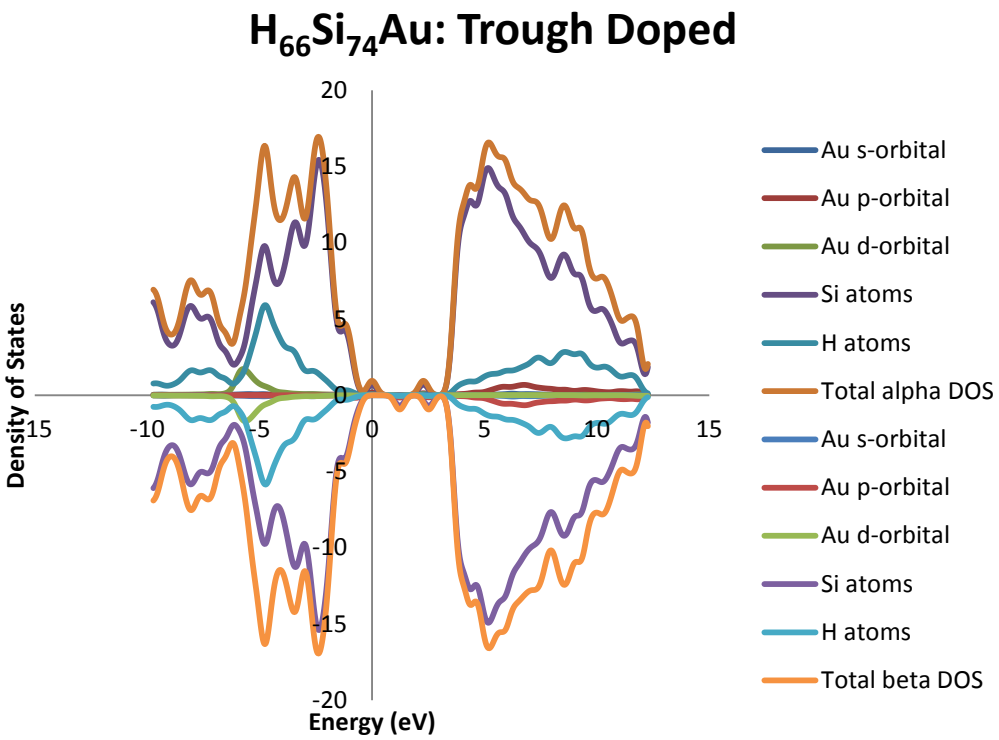
H66Si74Au: Trough Doped
Density of States
Energy (eV)
20
15
10
5
0
-5
-10
-15
-20
-15
-10
-5
0
5
10
15
Au s-orbital
Au p-orbital
Au d-orbital
Si atoms
H atoms
Total alpha DOS
Au s-orbital
Au p-orbital
Au d-orbital
Si atoms
H atoms
Total beta DOS

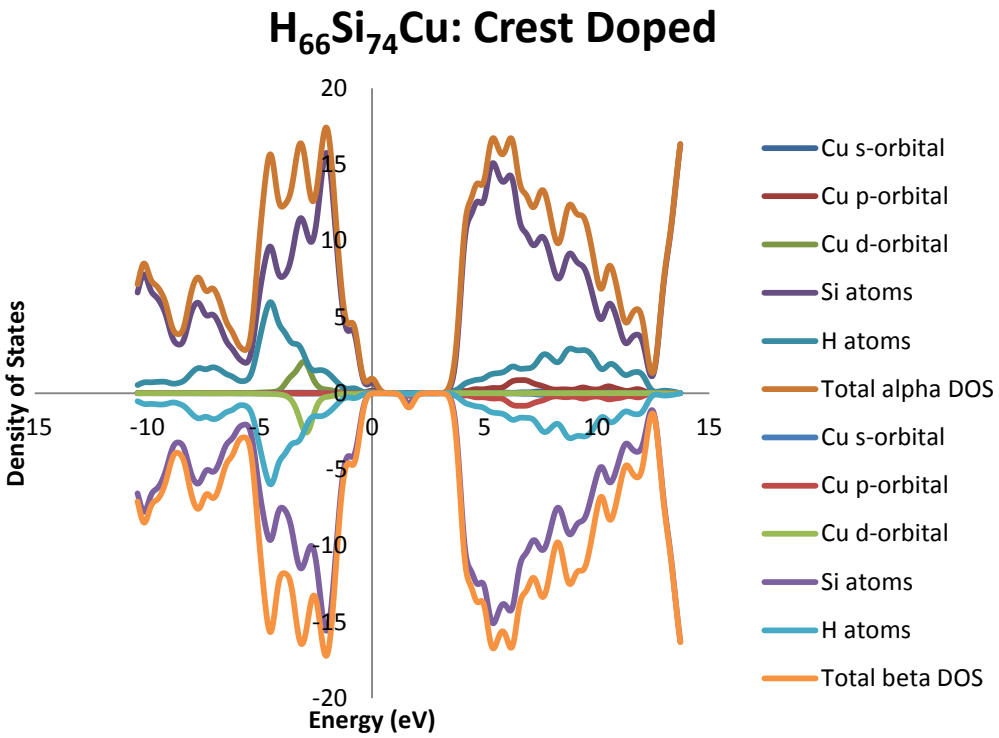
H66Si74Cu: Crest Doped
Density of States
Energy (eV)
20
15
10
5
0
-5
-10
-15
-20
-15
-10
-5
0
5
10
15
Cu s-orbital
Cu p-orbital
Cu d-orbital
Si atoms
H atoms
Total alpha DOS
Cu s-orbital
Cu p-orbital
Cu d-orbital
Si atoms
H atoms
Total beta DOS

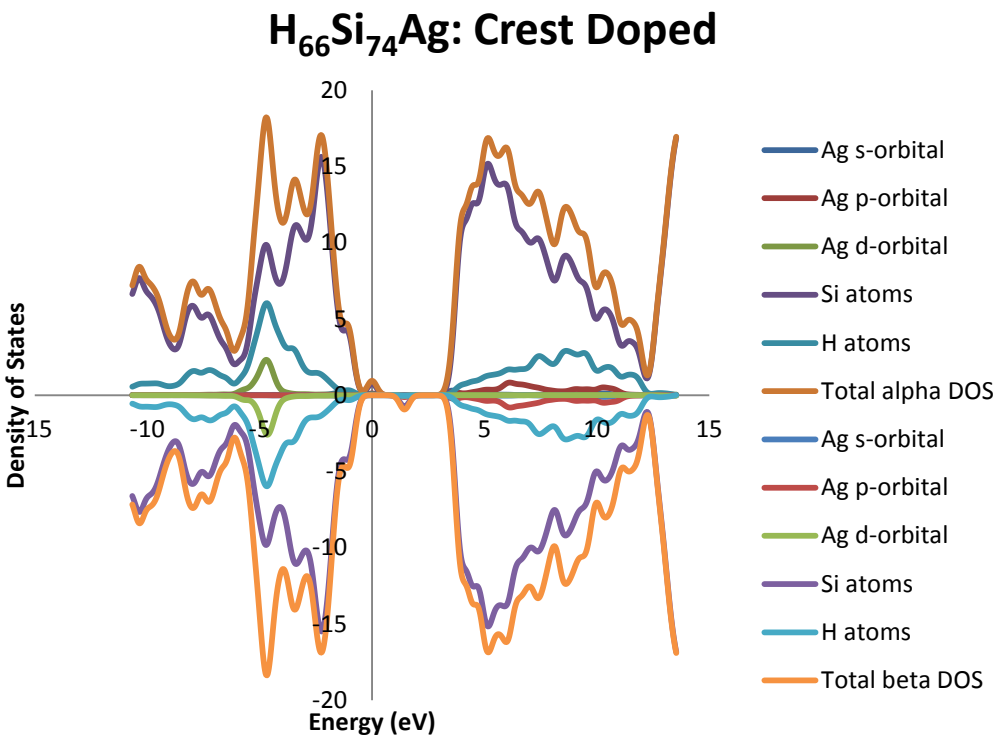
H66Si74Ag: Crest Doped
Density of States
Energy (eV)
20
15
10
5
0
-5
-10
-15
-20
-15
-10
-5
0
5
10
15
Ag s-orbital
Ag p-orbital
Ag d-orbital
Si atoms
H atoms
Total alpha DOS
Ag s-orbital
Ag p-orbital
Ag d-orbital
Si atoms
H atoms
Total beta DOS

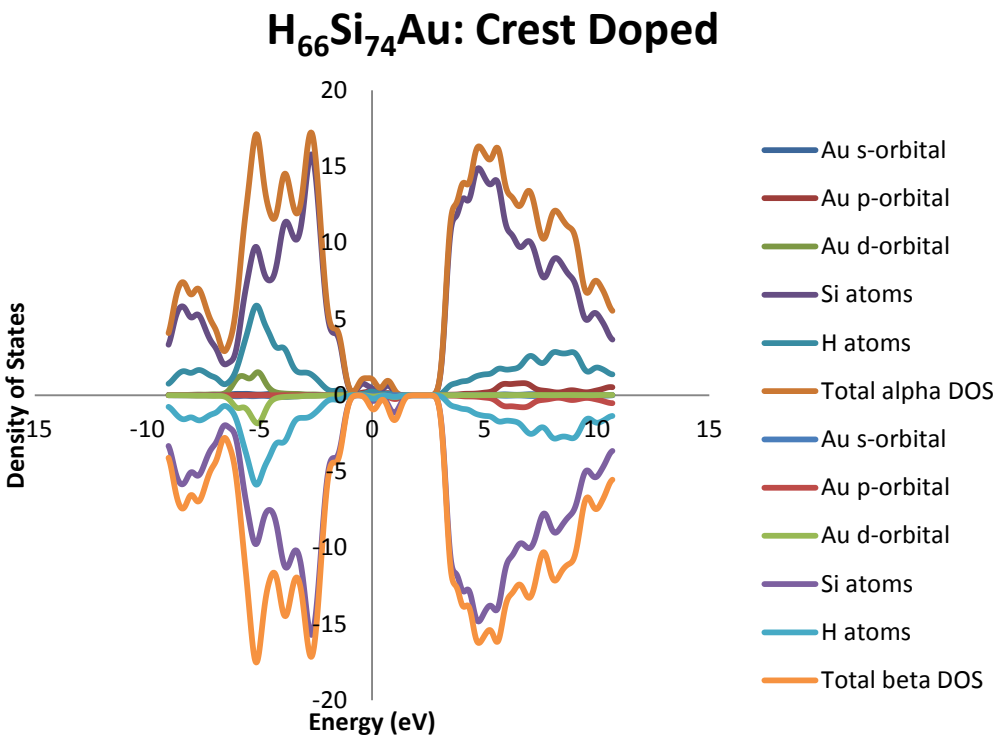
H66Si74Au: Crest Doped
Density of States
Energy (eV)
20
15
10
5
0
-5
-10
-15
-20
-15
-10
-5
0
5
10
15
Au s-orbital
Au p-orbital
Au d-orbital
Si atoms
H atoms
Total alpha DOS
Au s-orbital
Au p-orbital
Au d-orbital
Si atoms
H atoms
Total beta DOS

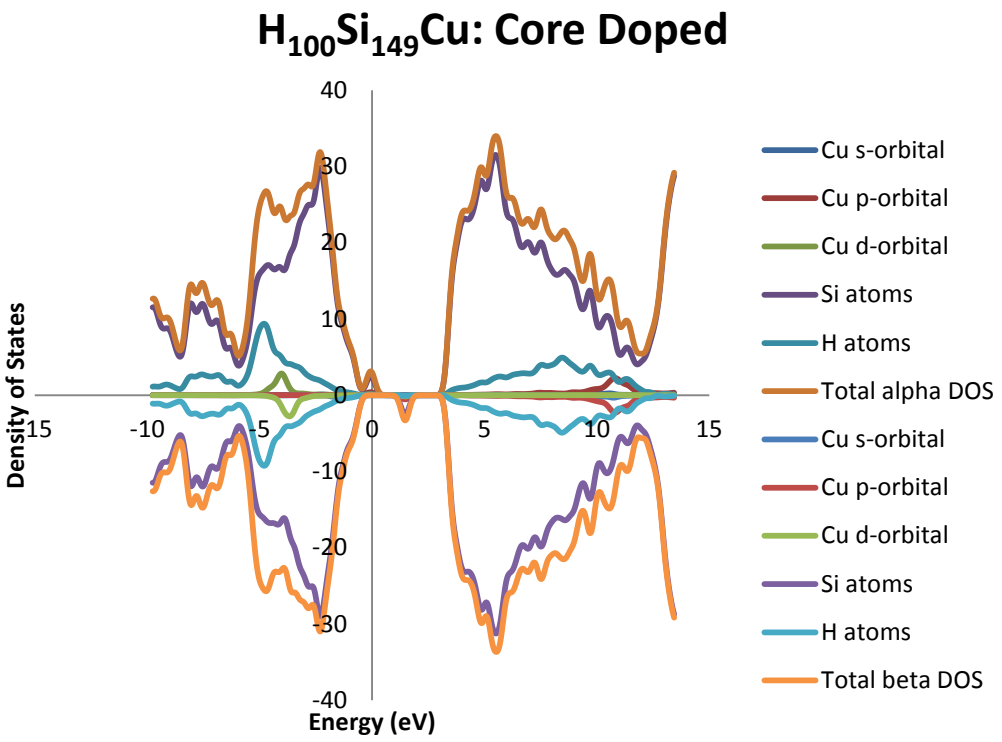
H100Si149Cu: Core Doped
Density of States
Energy (eV)
40
30
20
10
0
-10
-20
-30
-40
-15
-10
-5
0
5
10
15
Cu s-orbital
Cu p-orbital
Cu d-orbital
Si atoms
H atoms
Total alpha DOS
Cu s-orbital
Cu p-orbital
Cu d-orbital
Si atoms
H atoms
Total beta DOS

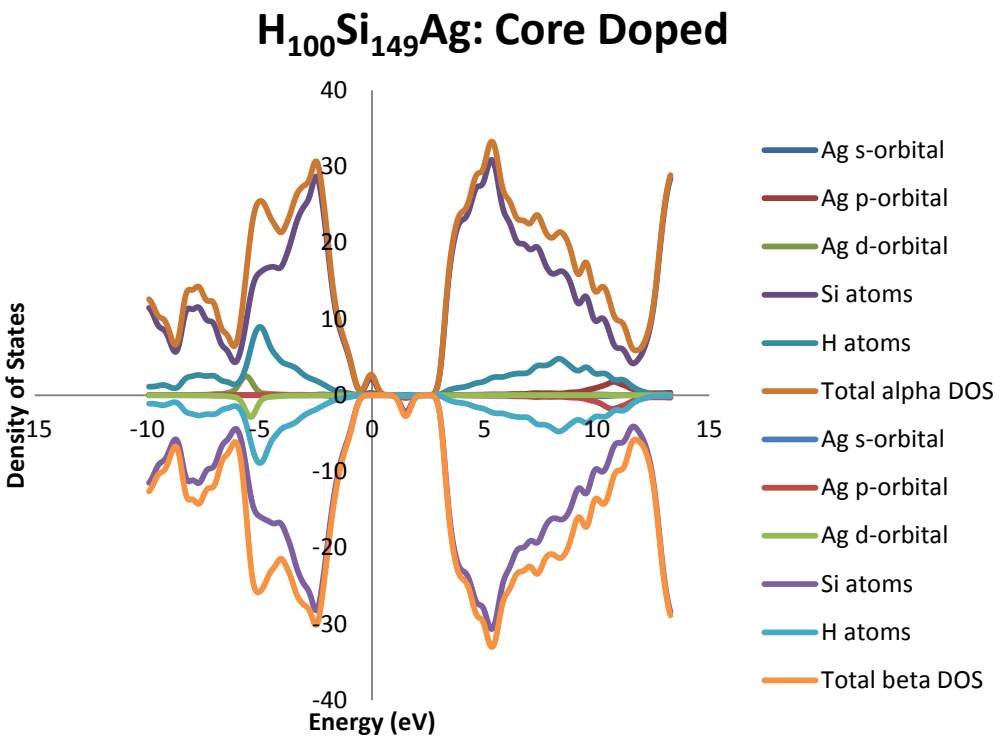
$H_{100}Si_{149}Ag$: Core Doped
Density of States
Energy (eV)
40
30
20
10
0
-10
-20
-30
-40
-15
-10
-5
0
5
10
15
Ag s-orbital
Ag p-orbital
Ag d-orbital
Si atoms
H atoms
Total alpha DOS
Ag s-orbital
Ag p-orbital
Ag d-orbital
Si atoms
H atoms
Total beta DOS

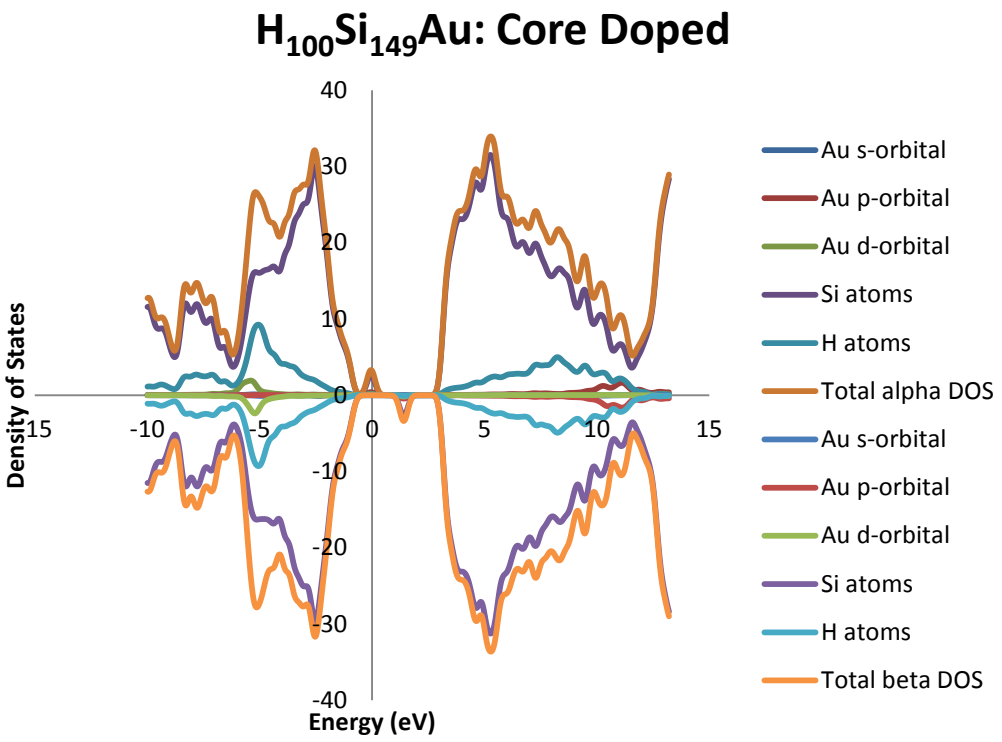
H100Si149Au: Core Doped
Density of States
Energy (eV)
40
30
20
10
0
-10
-20
-30
-40
-15
-10
-5
0
5
10
15
Au s-orbital
Au p-orbital
Au d-orbital
Si atoms
H atoms
Total alpha DOS
Au s-orbital
Au p-orbital
Au d-orbital
Si atoms
H atoms
Total beta DOS

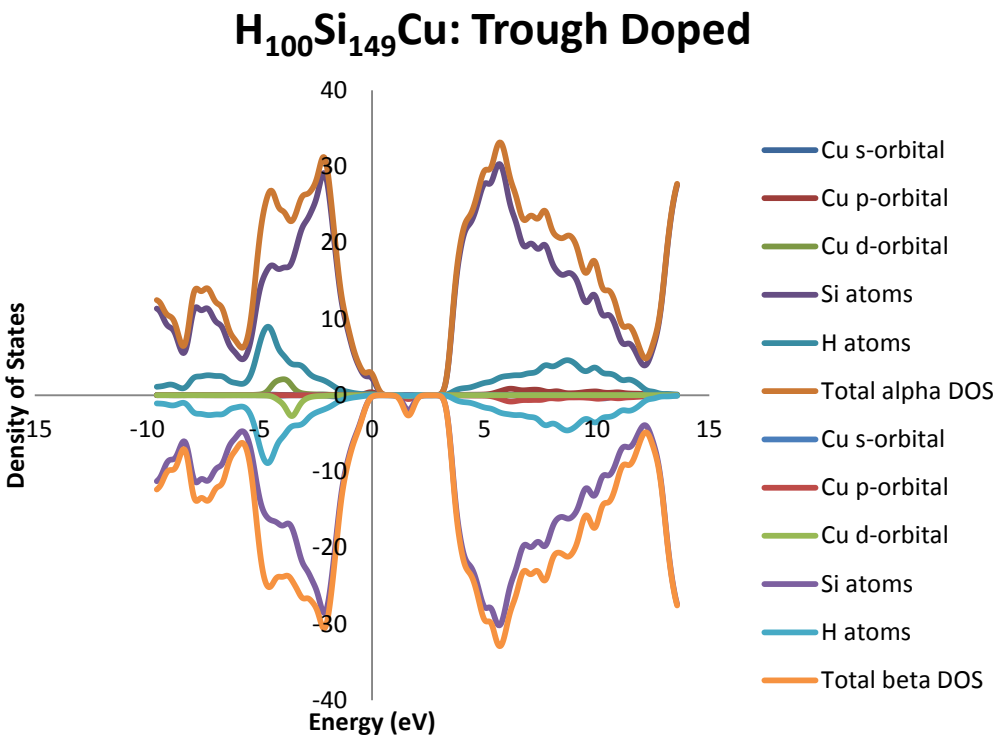
$H_{100}Si_{149}Cu$: Trough Doped
Density of States
Energy (eV)
40
30
20
10
0
-10
-20
-30
-40
-15
-10
-5
0
5
10
15
Cu s-orbital
Cu p-orbital
Cu d-orbital
Si atoms
H atoms
Total alpha DOS
Cu s-orbital
Cu p-orbital
Cu d-orbital
Si atoms
H atoms
Total beta DOS

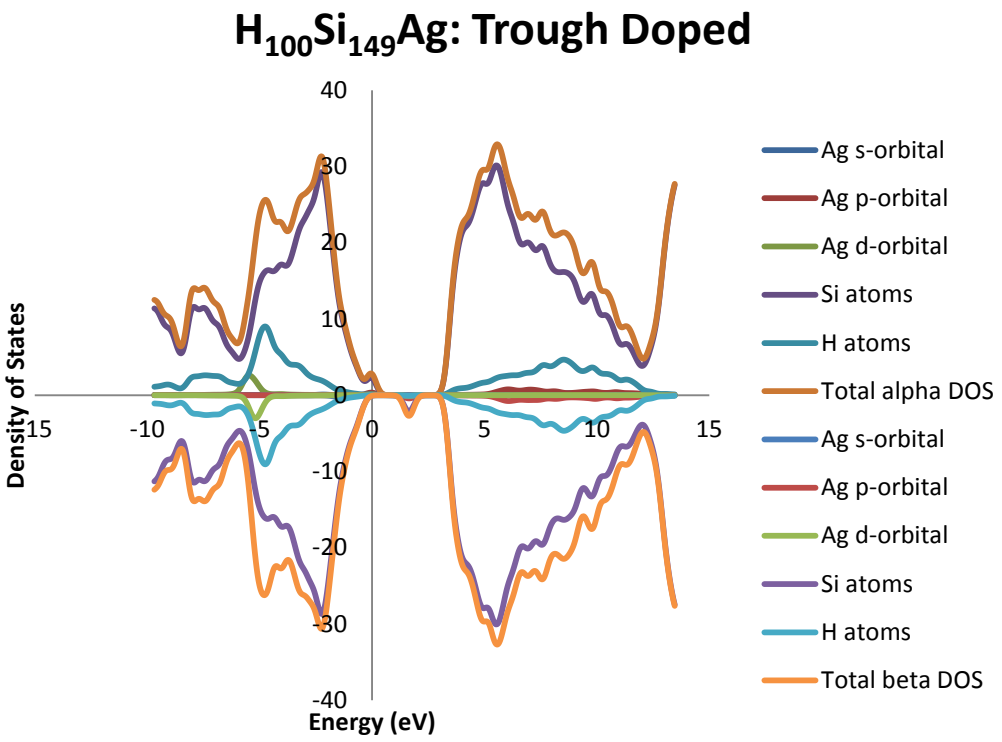
H100Si149Ag: Trough Doped
Density of States
Energy (eV)
40
30
20
10
0
-10
-20
-30
-40
-15
-10
-5
0
5
10
15
Ag s-orbital
Ag p-orbital
Ag d-orbital
Si atoms
H atoms
Total alpha DOS
Ag s-orbital
Ag p-orbital
Ag d-orbital
Si atoms
H atoms
Total beta DOS

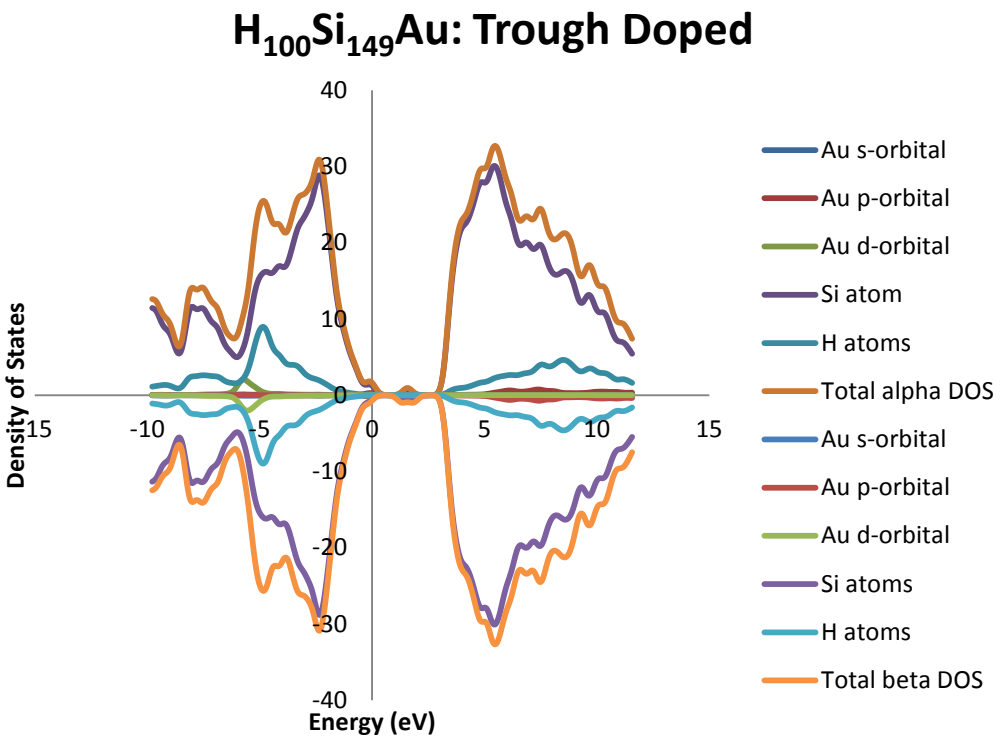
H100Si149Au: Trough Doped
Density of States
Energy (eV)
40
30
20
10
0
-10
-20
-30
-40
-15
-10
-5
0
5
10
15
Au s-orbital
Au p-orbital
Au d-orbital
Si atom
H atoms
Total alpha DOS
Au s-orbital
Au p-orbital
Au d-orbital
Si atoms
H atoms
Total beta DOS

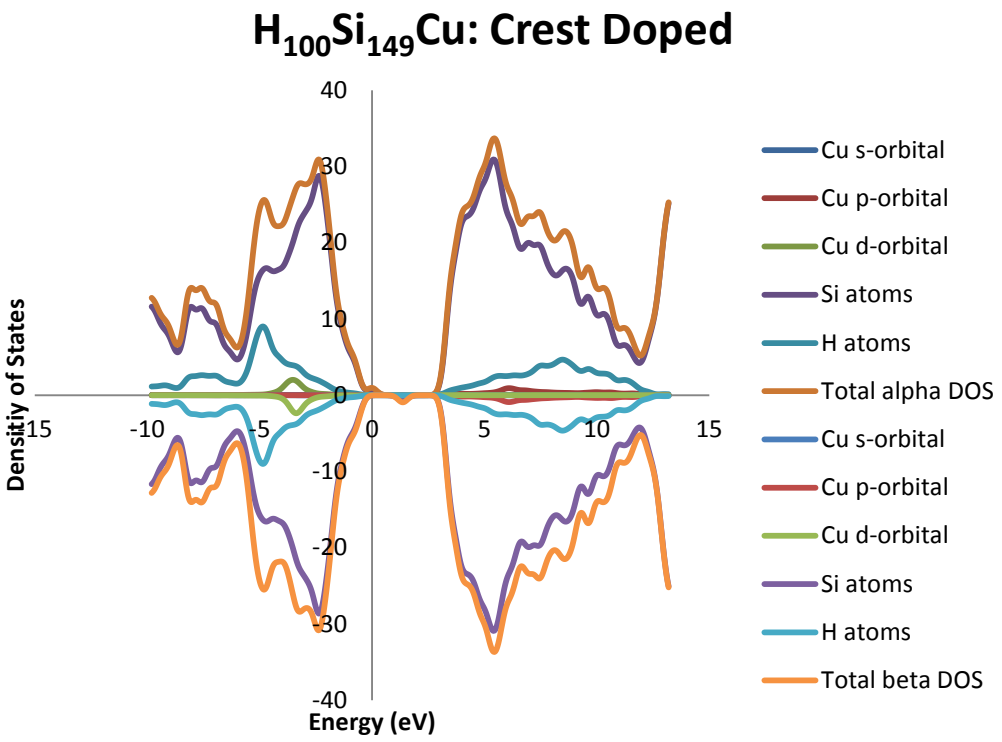
H100Si149Cu: Crest Doped
Density of States
Energy (eV)
40
30
20
10
0
-10
-20
-30
-40
-15
-10
-5
0
5
10
15
Cu s-orbital
Cu p-orbital
Cu d-orbital
Si atoms
H atoms
Total alpha DOS
Cu s-orbital
Cu p-orbital
Cu d-orbital
Si atoms
H atoms
Total beta DOS

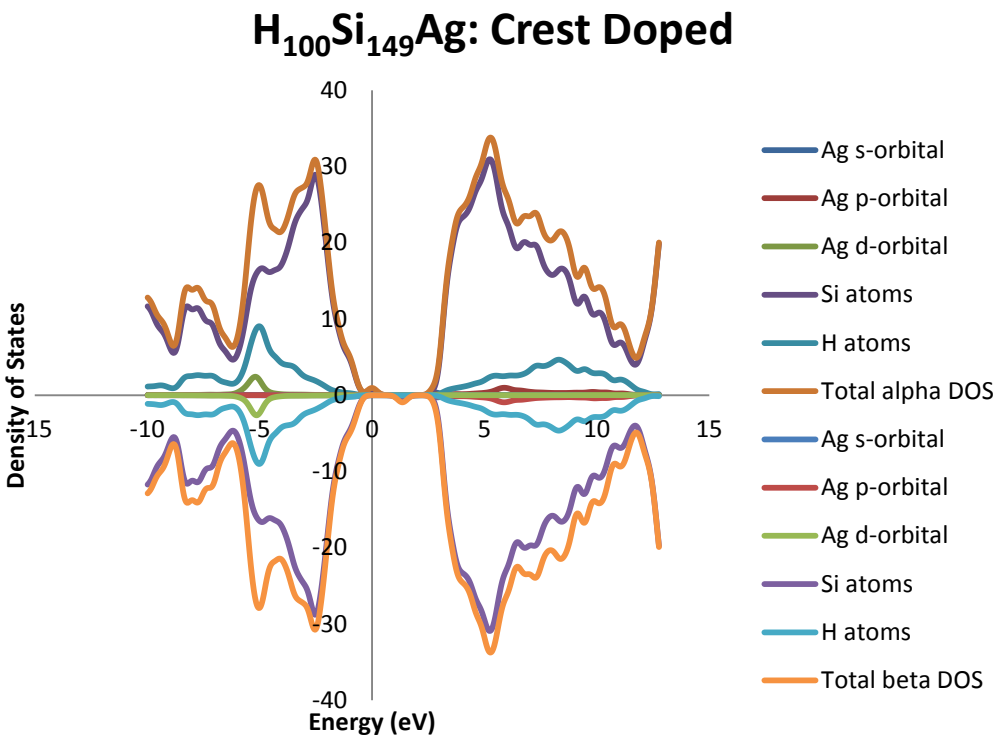
$H_{100}Si_{149}Ag$: Crest Doped
Density of States
Energy (eV)
40
30
20
10
0
-10
-20
-30
-40
-15
-10
-5
0
5
10
15
Ag s-orbital
Ag p-orbital
Ag d-orbital
Si atoms
H atoms
Total alpha DOS
Ag s-orbital
Ag p-orbital
Ag d-orbital
Si atoms
H atoms
Total beta DOS

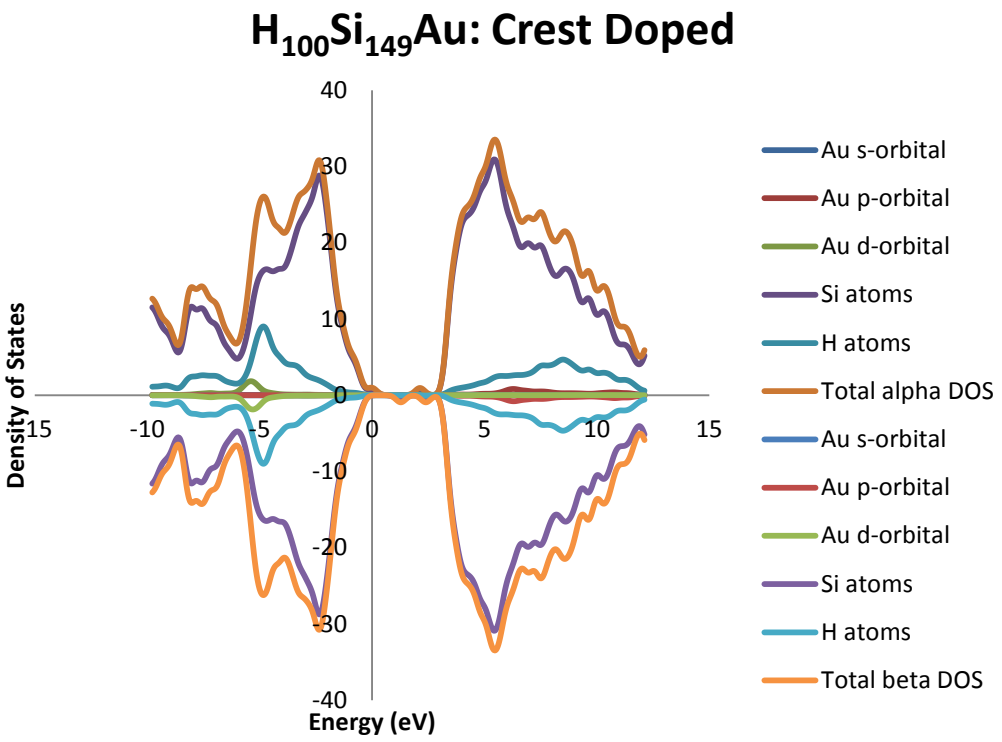
H100Si149Au: Crest Doped
Density of States
Energy (eV)
40
30
20
10
0
-10
-20
-30
-40
-15
-10
-5
0
5
10
15
Au s-orbital
Au p-orbital
Au d-orbital
Si atoms
H atoms
Total alpha DOS
Au s-orbital
Au p-orbital
Au d-orbital
Si atoms
H atoms
Total beta DOS

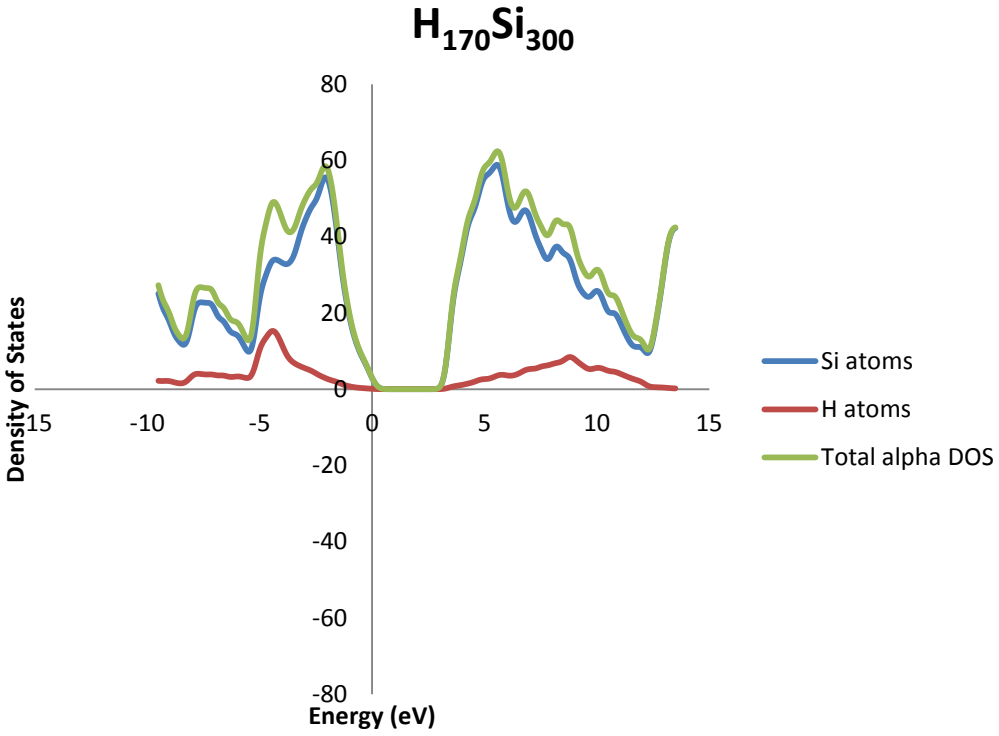
H170Si300
80
60
40
20
0
-20
-40
-60
-80
-15
-10
-5
0
5
10
15
Density of States
Energy (eV)
Si atoms
H atoms
Total alpha DOS

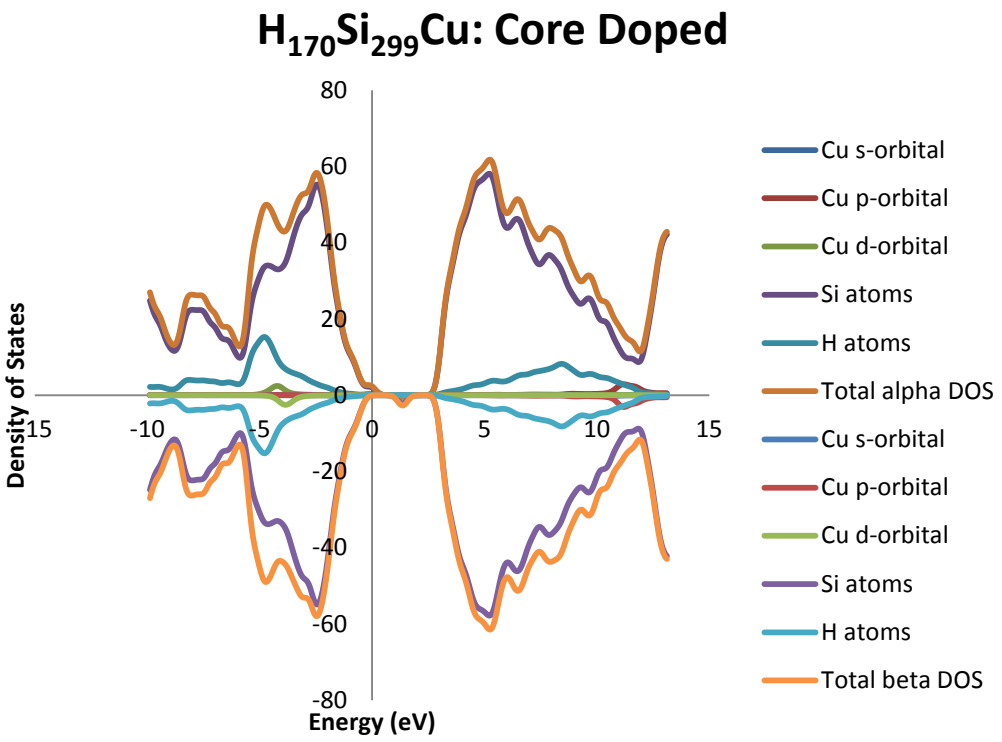
H170Si299Cu: Core Doped
Density of States
Energy (eV)
80
60
40
20
0
-20
-40
-60
-80
-15
-10
-5
0
5
10
15
Cu s-orbital
Cu p-orbital
Cu d-orbital
Si atoms
H atoms
Total alpha DOS
Cu s-orbital
Cu p-orbital
Cu d-orbital
Si atoms
H atoms
Total beta DOS

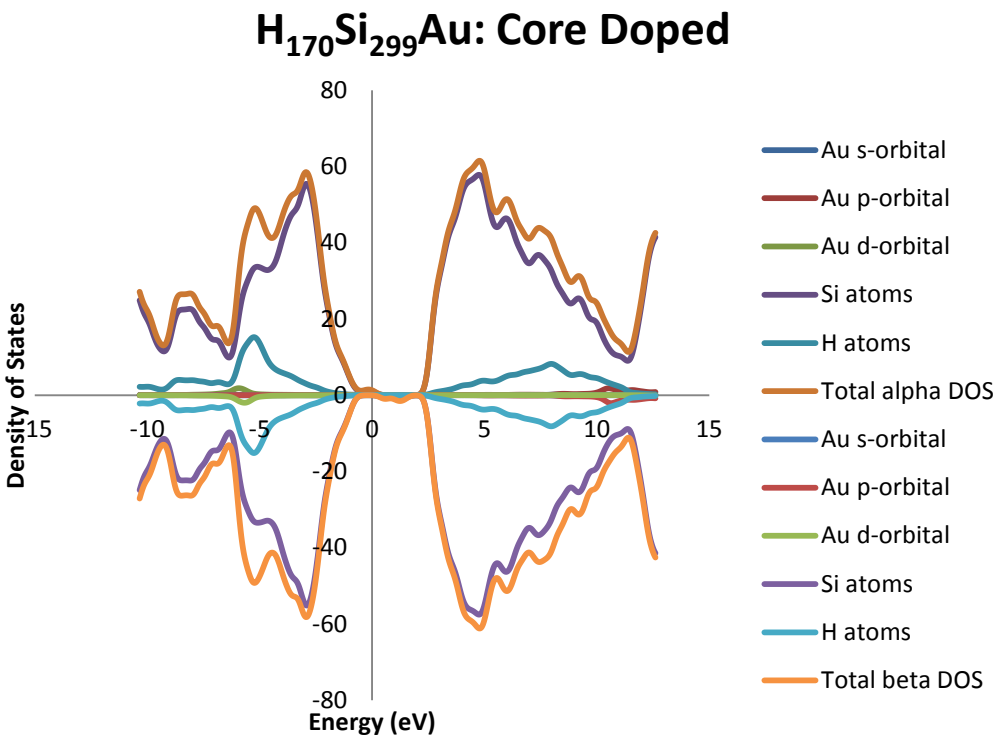
$H_{170}Si_{299}Au$: Core Doped
Density of States
Energy (eV)
80
60
40
20
0
-20
-40
-60
-80
-15
-10
-5
0
5
10
15
Au s-orbital
Au p-orbital
Au d-orbital
Si atoms
H atoms
Total alpha DOS
Au s-orbital
Au p-orbital
Au d-orbital
Si atoms
H atoms
Total beta DOS

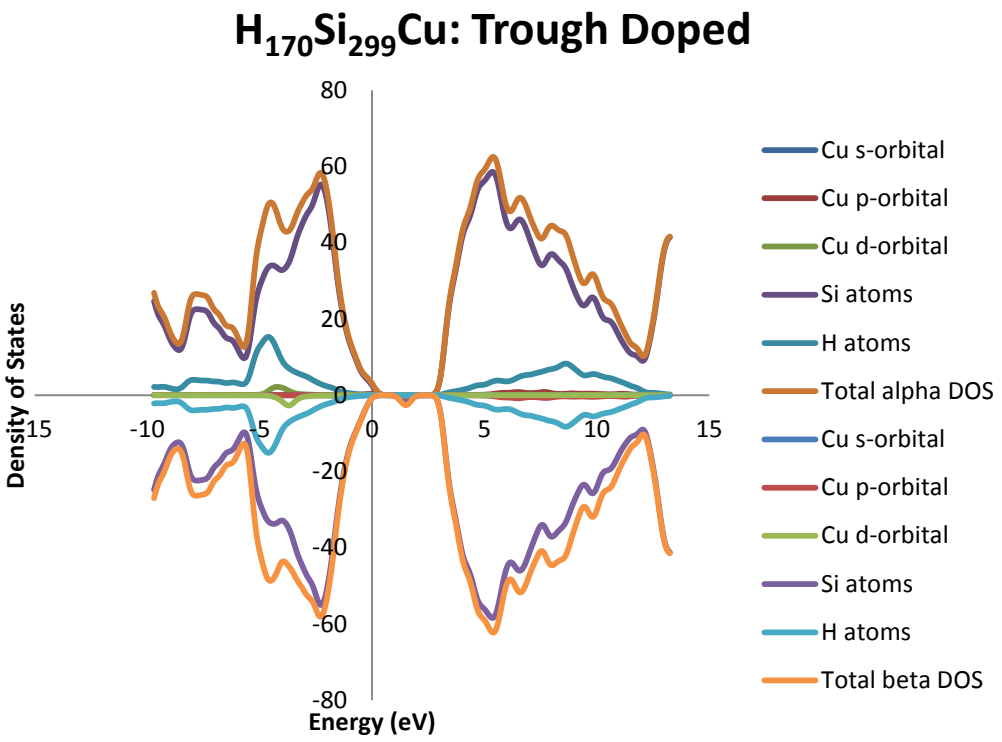
H170Si299Cu: Trough Doped
Density of States
Energy (eV)
80
60
40
20
0
-20
-40
-60
-80
-15
-10
-5
0
5
10
15
Cu s-orbital
Cu p-orbital
Cu d-orbital
Si atoms
H atoms
Total alpha DOS
Cu s-orbital
Cu p-orbital
Cu d-orbital
Si atoms
H atoms
Total beta DOS

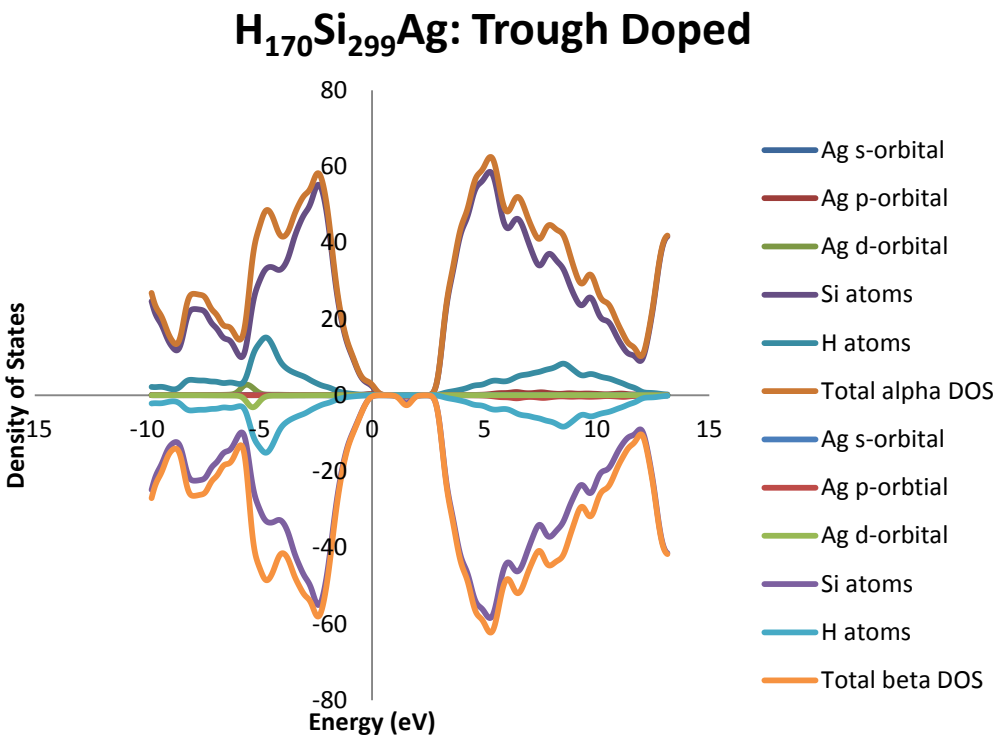
H170Si299Ag: Trough Doped
Density of States
Energy (eV)
80
60
40
20
0
-20
-40
-60
-80
-15
-10
-5
0
5
10
15
Ag s-orbital
Ag p-orbital
Ag d-orbital
Si atoms
H atoms
Total alpha DOS
Ag s-orbital
Ag p-orbtial
Ag d-orbital
Si atoms
H atoms
Total beta DOS

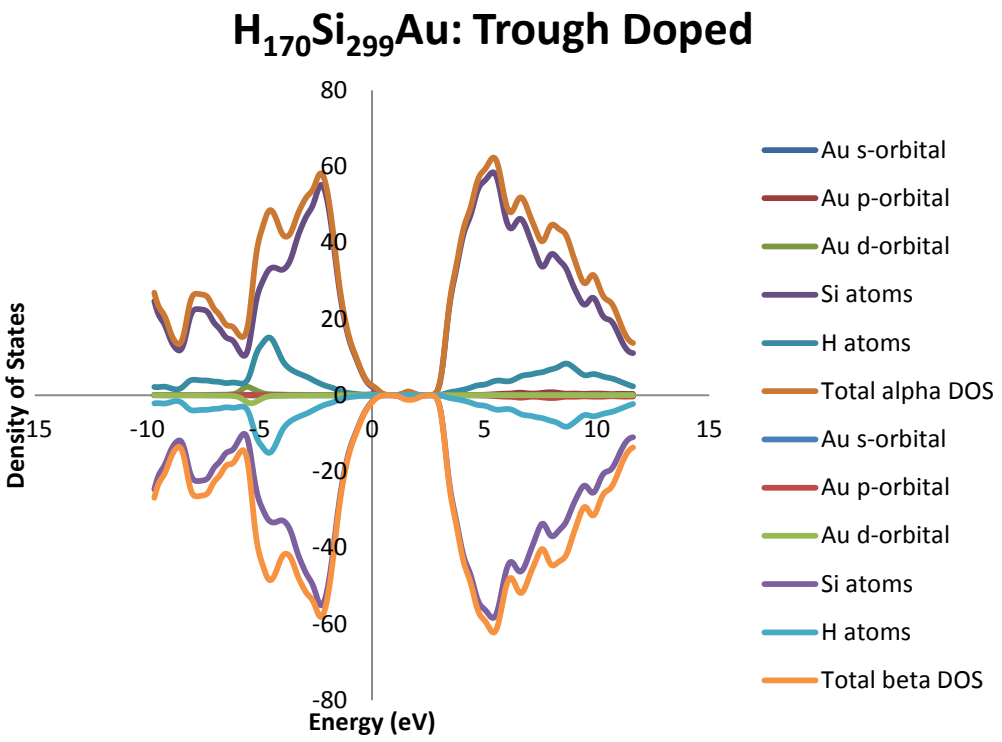
H170Si299Au: Trough Doped
Density of States
Energy (eV)
80
60
40
20
0
-20
-40
-60
-80
-15
-10
-5
0
5
10
15
Au s-orbital
Au p-orbital
Au d-orbital
Si atoms
H atoms
Total alpha DOS
Au s-orbital
Au p-orbital
Au d-orbital
Si atoms
H atoms
Total beta DOS

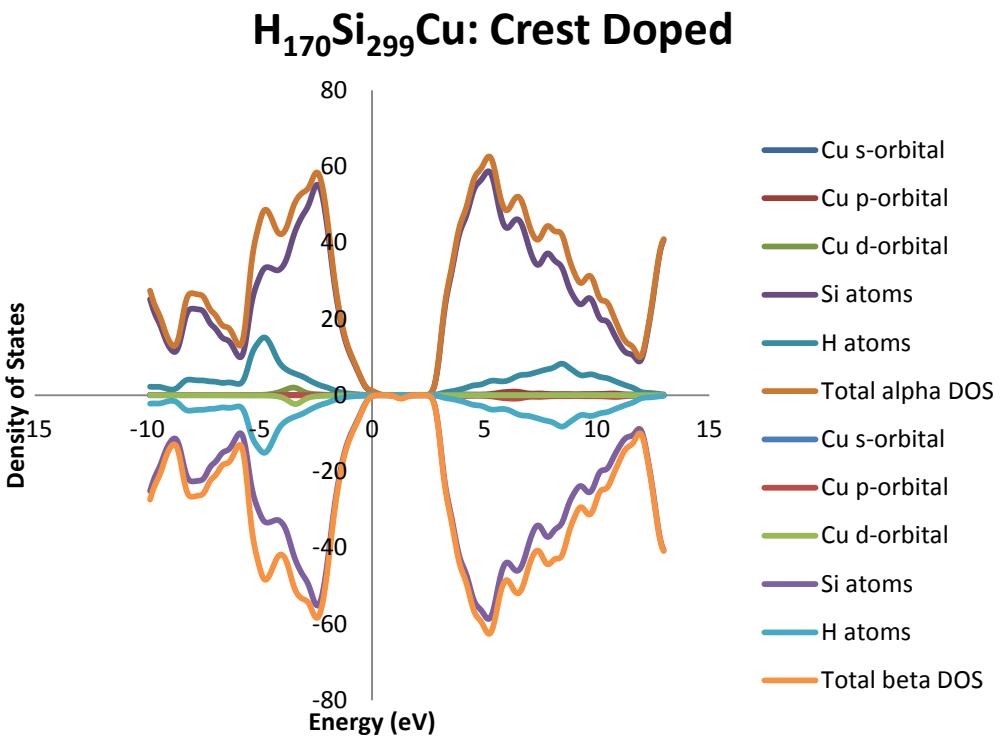
$H_{170}Si_{299}Cu$: Crest Doped
Density of States
Energy (eV)
80
60
40
20
0
-20
-40
-60
-80
-15
-10
-5
0
5
10
15
Cu s-orbital
Cu p-orbital
Cu d-orbital
Si atoms
H atoms
Total alpha DOS
Cu s-orbital
Cu p-orbital
Cu d-orbital
Si atoms
H atoms
Total beta DOS

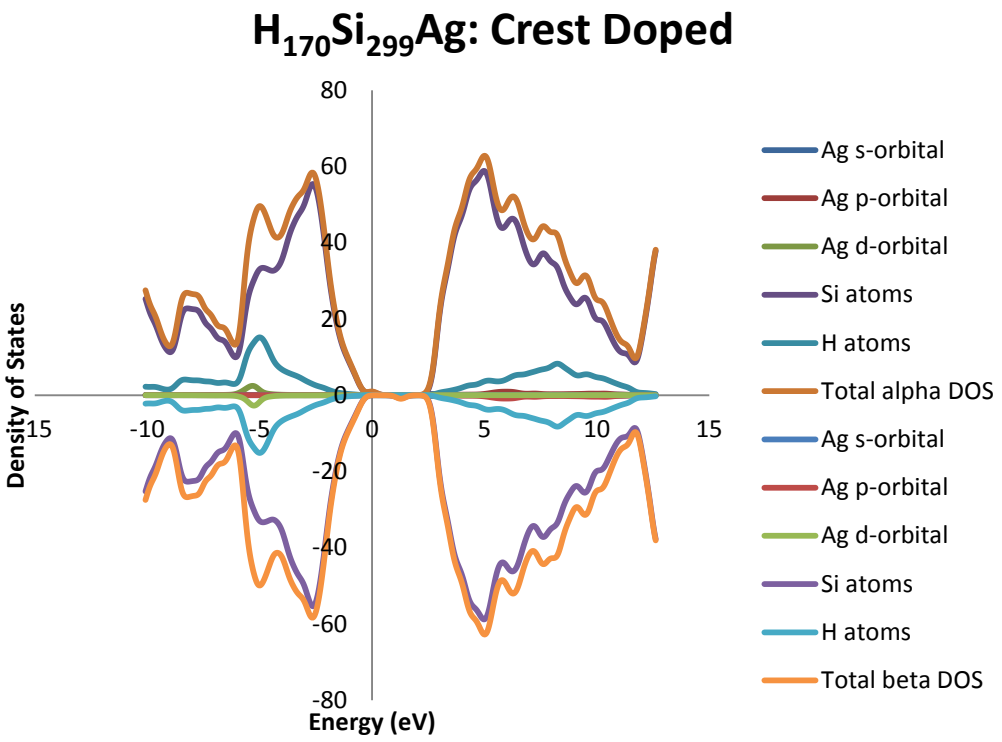
$H_{170}Si_{299}Ag$: Crest Doped
Density of States
Energy (eV)
80
60
40
20
0
-20
-40
-60
-80
-15
-10
-5
0
5
10
15
Ag s-orbital
Ag p-orbital
Ag d-orbital
Si atoms
H atoms
Total alpha DOS
Ag s-orbital
Ag p-orbital
Ag d-orbital
Si atoms
H atoms
Total beta DOS

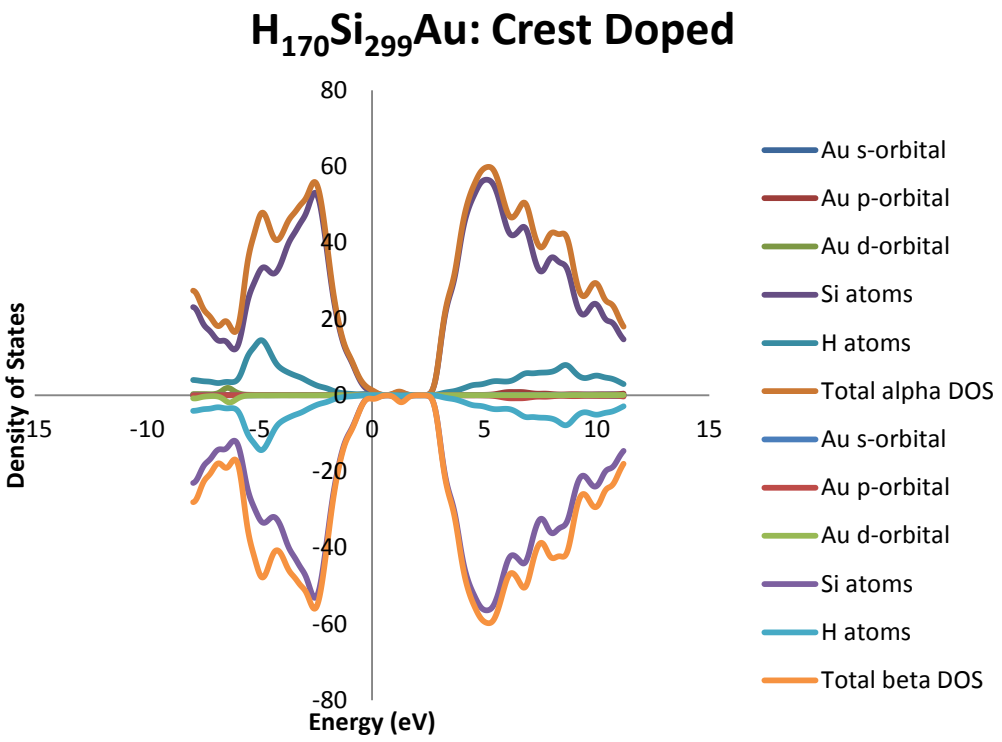
$H_{170}Si_{299}Au$: Crest Doped
Density of States
Energy (eV)
80
60
40
20
0
-20
-40
-60
-80
-15
-10
-5
0
5
10
15
Au s-orbital
Au p-orbital
Au d-orbital
Si atoms
H atoms
Total alpha DOS
Au s-orbital
Au p-orbital
Au d-orbital
Si atoms
H atoms
Total beta DOS

References

[1] S. Chu and A. Majumdar, Nature **488**, 294 (2012).

[2] E. Serrano, G. Rus, and J. García-Martínez, Renewable and Sustainable Energy Reviews **13**, 2373 (2009).

[3] P. Oelhafen and a Schuler, Solar Energy **79**, 110 (2005).

[4] R. Rurali, Reviews of Modern Physics **82**, 427 (2010).

[5] E. Garnett and P. Yang, Nano Letters **10**, 1082 (2010).

[6] O. E. Semonin, J. M. Luther, S. Choi, H.-Y. Chen, J. Gao, A. J. Nozik, and M. C. Beard, Science (New York, N.Y.) **334**, 1530 (2011).

[7] M. D. Archer, **14**, 61 (2002).

[8] J. Wang, S. J. Xiong, X. L. Wu, T. H. Li, and P. K. Chu, Nano Letters **10**, 1466 (2010).

[9] R. Pereira, a. Stegner, T. Andlauer, K. Klein, H. Wiggers, M. Brandt, and M. Stutzmann, Physical Review B **79**, 1 (2009).

[10] K.-H. Hong, J. Kim, J. H. Lee, J. Shin, and U.-I. Chung, Nano Letters 1671 (2010).

[11] B. Delley and E. Steigmeier, Physical Review B **47**, 1397 (1993).

[12] R. Pereira, D. Rowe, R. Anthony, and U. Kortshagen, Physical Review B **83**, 1 (2011).

[13] a. Carvalho, J. Coutinho, M. Barroso, E. Silva, S. Öberg, M. Rayson, and P. Briddon, Physical Review B **84**, 1 (2011).

[14] V. Schmidt, J. V. Wittemann, S. Senz, and U. Gösele, Advanced Materials **21**, 2681 (2009).

[15] K. Q. Peng, J. J. Hu, Y. J. Yan, Y. Wu, H. Fang, Y. Xu, S. T. Lee, and J. Zhu, Advanced Functional Materials **16**, 387 (2006).

[16] a. Fontcuberta i Morral, J. Arbiol, J. D. Prades, a. Cirera, and J. R. Morante, Advanced Materials **19**, 1347 (2007).

[17] A. Zhao, X. Yu, X. Wang, and W. Wu, Nanotechnology Materials and … 380 (2011).

[18] D. Parlevliet and J. C. L. Cornish, MRS Proceedings **989**, 0989 (2011).

[19] K. Rykaczewski, O. Hildreth, and C. Wong, Nano … 2369 (2011).

[20] J. L. Lensch-Falk, E. R. Hemesath, D. E. Perea, and L. J. Lauhon, Journal of Materials Chemistry **19**, 849 (2009).

[21] J. Hu, T. W. Odom, and C. M. Lieber, Accounts of Chemical Research **32**, 435 (1999).

[22] M. Alonso, I. Marcus, M. Garriga, a. Goñi, J. Jedrzejewski, and I. Balberg, Physical Review B **82**, 1 (2010).

[23] L. Ramos, J. Furthmüller, and F. Bechstedt, Physical Review B **72**, 1 (2005).

[24] G. Faraci, S. Gibilisco, and A. R. Pennisi, Physical Review B **80**, 1 (2009).

[25] J. Han, T.-L. Chan, and J. Chelikowsky, Physical Review B **82**, 1 (2010).

[26] M. Bruno, M. Palummo, S. Ossicini, and R. Delsole, Surface Science **601**, 2707 (2007).

[27] T. Vo, A. J. Williamson, and G. Galli, Physical Review B **74**, 1 (2006).

[28] A. K. Singh, V. Kumar, R. Note, and Y. Kawazoe, Nano Letters **5**, 2302 (2005).

[29] T. Markussen, A.-P. Jauho, and M. Brandbyge, Nano Letters **8**, 3771 (2008).

[30] P. W. Leu, B. Shan, and K. Cho, Physical Review B **73**, 1 (2006).

[31] F. Iori, S. Ossicini, and S. Frabboni, Etsf.polytechnique.fr (2007).

[32] C. Q. Sun, Progress in Solid State Chemistry **35**, 1 (2007).

[33] L. Shen, M. Zeng, S.-W. Yang, C. Zhang, X. Wang, and Y. Feng, Journal of the American Chemical Society **132**, 11481 (2010).

[34] N. Sai, K. Leung, and J. Chelikowsky, Physical Review B **83**, 3 (2011).

[35] D. Bandyopadhyay and M. Kumar, Chemical Physics **353**, 170 (2008).

[36] J. Wu and F. Hagelberg, The Journal of Physical Chemistry. A **110**, 5901 (2006).

[37] J. R. Chelikowsky, M. M. G. Alemany, T.-L. Chan, and G. M. Dalpian, Reports on Progress in Physics **74**, 046501 (2011).

[38] T. Ohgi and D. Fujita, Physical Review B **66**, 1 (2002).

[39] J. Wang and J.-G. Han, The Journal of Chemical Physics **123**, 64306 (2005).

[40] S. Zhang, S.-H. Wei, and A. Zunger, Physical Review B **63**, 075205 (2001).

[41] C. Zhang, G. Chen, K. Wang, H. Yang, T. Su, C. Chan, M. Loy, and X. Xiao, Physical Review Letters **94**, 2 (2005).

[42] O. Takeuchi, M. Kageshima, H. Sakama, and A. Kawazu, Physical Review B **83**, 1 (2011).

[43] N. B. Nguyen, C. Dufour, and S. Petit, Journal of Physics: Condensed Matter **20**, 455209 (2008).

[44] J. B. Jaeger, T. D. Jaeger, and M. a Duncan, The Journal of Physical Chemistry. A **110**, 9310 (2006).

[45] H. Peng and S. Lany, Physical Review B **85**, 1 (2012).

[46] J. Ma, S.-H. Wei, N. R. Neale, and A. J. Nozik, Applied Physics Letters **98**, 173103 (2011).

[47] M. N. Huda, M. M. Al-Jassim, and J. a. Turner, Journal of Renewable and Sustainable Energy **3**, 053101 (2011).

[48] X. Xu and P. Servati, Nano Letters **9**, 1999 (2009).

[49] D. G. Cahill, K. Goodson, and A. Majumdar, Journal of Heat Transfer **124**, 223 (2002).

[50] H. Lu, Y.-J. Zhao, X.-B. Yang, and H. Xu, Physical Review B **86**, 1 (2012).

[51] S. Ismail-Beigi and T. Arias, Physical Review B **57**, 11923 (1998).

[52] Z. Zhou, R. a Friesner, and L. Brus, Journal of the American Chemical Society **125**, 15599 (2003).

[53] F. Baletto and R. Ferrando, Reviews of Modern Physics **77**, 371 (2005).

[54] C.-T. Peng, J.-C. Lin, C.-T. Lin, and K.-N. Chiang, Sensors and Actuators A: Physical **119**, 28 (2005).

[55] T. Xie and M. Bogdan, Eng.auburn.edu 1 (2010).

[56] R. H. Scheicher, S. Li, C. M. Araujo, A. Blomqvist, R. Ahuja, and P. Jena, Nanotechnology **22**, 335401 (2011).

[57] D. Bandyopadhyay and M. Kumar, Chemical Physics **353**, 170 (2008).

[58] A. Zdetsis, Physical Review B **79**, 1 (2009).

[59] Y. Dubi and M. Di Ventra, Review of Modern Physics **83**, 131 (2011).

[60] R. J. Mehta, Y. Zhang, H. Zhu, D. S. Parker, M. Belley, D. J. Singh, R. Ramprasad, T. Borca-Tasciuc, and G. Ramanath, Nano Letters **12**, 4523 (2012).

[61] T. Markussen, R. Rurali, M. Brandbyge, and A.-P. Jauho, Physical Review B **74**, 1 (2006).

[62] D. Parker and D. Singh, Physical Review B **85**, 1 (2012).

[63] H.-X. Deng, S.-S. Li, J. Li, and S.-H. Wei, Physical Review B **85**, 1 (2012).

[64] J. Ma, S.-H. Wei, N. R. Neale, and A. J. Nozik, Applied Physics Letters **98**, 173103 (2011).

[65] B. Gelloz, H. Sano, R. Boukherroub, D. D. M. Wayner, D. J. Lockwood, and N. Koshida, Applied Physics Letters **83**, 2342 (2003).

[66] Z. Zhou, L. Brus, and R. Friesner, Nano Letters **3**, 163 (2003).

[67] C. K. M. Fung, M. Q. H. Zhang, Z. Dong, and W. J. Li, 5th IEEE Conference on Nanotechnology, 2005. 353 (2005).

[68] R. He, X. L. Feng, M. L. Roukes, and P. Yang, Nano Letters **8**, 1756 (2008).

[69] A. May, D. Singh, and G. Snyder, Physical Review B **79**, 1 (2009).

[70] G. B. Akguc and O. Gülseren, Physical Review B **85**, 1 (2012).

[71] L. Zhang and D. Singh, Physical Review B **81**, 1 (2010).

[72] A. D. Becke, The Journal of Chemical Physics **98**, 1372 (1993).

[73] W. Kohn, a. D. Becke, and R. G. Parr, The Journal of Physical Chemistry **100**, 12974 (1996).

[74] D. Langreth and M. Mehl, Physical Review B (1983).

[75] A. D. Becke, The Journal of Chemical Physics **98**, 5648 (1993).

[76] B. S. Jursic, Journal of Molecular Structure: THEOCHEM **497**, 65 (2000).

[77] J. P. Perdew, M. Ernzerhof, and K. Burke, The Journal of Chemical Physics **105**, 9982 (1996).

[78] R.B. Frisch et.al., Gaussian 03 **v D02**, (2004).

[79] P. Stephens, F. Devlin, C. Chabalowski, and M. Frisch, The Journal of Physical Chemistry **98**, 11623 (1994).

[80] J.-D. Chai and M. Head-Gordon, The Journal of Chemical Physics **131**, 174105 (2009).

[81] J. Paier, M. Marsman, K. Hummer, G. Kresse, I. C. Gerber, and J. G. Angyán, The Journal of Chemical Physics **124**, 154709 (2006).

[82] R. Leitsmann, C. Panse, F. Küwen, and F. Bechstedt, Physical Review B **80**, 1 (2009).

[83] S. Chiodo, N. Russo, and E. Sicilia, The Journal of Chemical Physics **125**, 104107 (2006).

[84] C. E. Check, T. O. Faust, J. M. Bailey, B. J. Wright, T. M. Gilbert, and L. S. Sunderlin, The Journal of Physical Chemistry A **105**, 8111 (2001).

[85] C. Xiao, F. Hagelberg, and W. Lester, Physical Review B **66**, 1 (2002).

Biographical Information

Cedric Leon Mayfield earned his Bachelor of Science degree in Physics from the University of Texas at Arlington. His undergraduate project was Density Functional modeling of nanostructures. Analytical processing was done using Fortran and C programming. During his undergraduate career he worked as a physics tutor, grader, and exam proctor for the Department of Physics at UTA. He graduated with the Latin honor Cum Laude. In the course of this Master's thesis, Cedric was also involved with the simulations and study of binary and ternary metal oxide semiconductor nanocrystals such as Fe_2O_3 and pyrochlore $Bi_2Ti_2O_7$. He has authored a paper on pristine silicon nanocrystals and also presented results at national conferences. He intends to work on the design of materials for renewable energy applications.